Tunability and Performance Enhancement for Planar Microwave Filters

Hongliang Guo

A dissertation submitted for the degree of Doctor of Philosophy

Heriot-Watt University

School of Engineering and Physical Sciences

May 2020

Abstract

Radio-frequency (RF) spectrum is exploited as a valuable resource for wireless applications such as mobile and satellite communications. As a result, communication systems including satellite communication and emerging 5G are trending to have frequency-agility to adapt to highly complex RF environments. However, due to the nature of materials and components, electrically-tunable planar filters, which play essential roles in frequency agile RF systems, have their disadvantages of low-order, high-loss, and poor selectivity. This has limited the overall performances of the frequency agile RF systems. In the light of this scenario, the objective of this thesis is to develop efficient performance-enhancement techniques, including the lossy technique, and the active technique, into the high-selective tunable planar filters to boost the performances of tunable RF systems.

First of all, an electrically reconfigurable microstrip dual-mode filter is demonstrated with nonuniform-quality-factor lossy technique. The 4-pole bandpass filter exhibits a continuously bandwidth tuning and centre frequency tuning capability. By making use of the doubly tuned resonant property of the dual-mode microstrip open-loop resonator, passband flatness can be improved by simply loading resistors on the even-odd mode symmetrical plane of resonators. Moreover, two intrinsic transmission zeros are in upper and lower stopbands enhancing the filter selectivity. The coupling matrix synthesis is introduced to describe the nonuniform-quality-factor distribution in a filter network. The experiment of this type of four-pole tunable lossy filter has presented a good agreement with the simulation.

Then, the thesis reports a novel 5-pole lossy bandpass filter with the bandwidth tunability. In order to improve the filter selectivity, we choose a hybrid filter structure consist of hairpin resonators and dual behaviour resonators to produce two adjustable transmission zeros for high selective responses. A novel lossy technique named centre-loaded resistive cross-coupling is developed to efficiently reduce the insertion-loss variation of the tuned passband. The fabricated filter demonstrates an insertion loss variation of less than 1 dB for all bandwidth states.

To compensate the loss within the varactor-tuned narrowband filter, a tunable 2-pole active filter is presented with a constant absolute bandwidth. The negative resistance

generated from active circuits successfully cancels the loss within the varactor-loaded resonators resulting in high quality-factor resonator filter responses. With the transistor small-signal model, the value of the negative resistance of the active circuit can be predicted by network analysis. Experiments were carried out to validate the design.

Dedication

To my parents

Acknowledgements

I would like to express my deep appreciation to my supervisor, Professor Jia-Sheng Hong for his guidance, encouragement, and support during the years of my PhD study. I learned not only professional knowledge but also the attitude towards science and research.

I would also like to thank Rong Fu, Zhou Zhou, Jia Ni, Wenxing Tang, Qianru Zhou, Jiayu Rao, and every lovely person.

Most importantly, my deepest gratitude goes to my family for their support and encouragement.

Research Thesis Submission

Please note this form should be bound into the submitted thesis.

Name:	Hongliang Guo		
School:	EPS/EECE		
Version: *(i.e. First, Resubmission, Final)*	Final	Degree Sought:	PhD in Microwave Engineering

Declaration

In accordance with the appropriate regulations I hereby submit my thesis and I declare that:

1. The thesis embodies the results of my own work and has been composed by myself
2. Where appropriate, I have made acknowledgement of the work of others
3. The thesis is the correct version for submission and is the same version as any electronic versions submitted*.
4. My thesis for the award referred to, deposited in the Heriot-Watt University Library, should be made available for loan or photocopying and be available via the Institutional Repository, subject to such conditions as the Librarian may require
5. I understand that as a student of the University I am required to abide by the Regulations of the University and to conform to its discipline.
6. I confirm that the thesis has been verified against plagiarism via an approved plagiarism detection application e.g. Turnitin.

ONLY for submissions including published works

Please note you are only required to complete the Inclusion of Published Works Form (page 2) if your thesis contains published works)

7. Where the thesis contains published outputs under Regulation 6 (9.1.2) or Regulation 43 (9) these are accompanied by a critical review which accurately describes my contribution to the research and, for multi-author outputs, a signed declaration indicating the contribution of each author (complete)
8. Inclusion of published outputs under Regulation 6 (9.1.2) or Regulation 43 (9) shall not constitute plagiarism.

* *Please note that it is the responsibility of the candidate to ensure that the correct version of the thesis is submitted.*

Signature of Candidate:	Hongliang Guo	Date:	04/04/2021

Submission

Submitted By *(name in capitals):*	HONGLIANG GUO
Signature of Individual Submitting:	Hongliang Guo
Date Submitted:	04/04/2021

For Completion in the Student Service Centre (SSC)

Limited Access	Requested	Yes		No		Approved	Yes		No	
*E-thesis Submitted (**mandatory for final theses**)*										
Received in the SSC by *(name in capitals):*						Date:				

TABLE OF CONTENTS

LIST OF PUBLICATIONS

1. H. Guo, J. Ni, and J. Hong, 'Varactor-Tuned Dual-Mode Bandpass Filter With Nonuniform Q Distribution', *IEEE Microw. Wireless Compon. Lett.*, vol. 28, no. 11, pp. 1002–1004, Nov. 2018.

2. H. Guo, J. Ni, J. Hong, and P. M. Iglesias, 'Lossy Dual-Mode Bandpass Filter with Non-Uniform Q Method', in *2018 48th European Microwave Conference (EuMC)*, Sep. 2018, pp. 356–359.

3. J. Rao, H. Guo, J. Ni, J. Hong, and P. M. Iglesias, 'C-Band Microstrip Lossy Filter using Resistive-loaded Closed-Loop Resonators', in *2019 49th European Microwave Conference (EuMC)*, Sep. 2019.

CHAPTER 1
INTRODUCTION

1.1 Motivation

RF (radio-frequency) /microwave is widely used in modern technologies, such as wireless communications, sensing, radar, satellite, navigation, and medical instruments. As the channel selecting component, RF filters play important roles in various RF/microwave systems. In today's crowded RF environment, the frequency spectrum resources are more valuable and limited. Meanwhile, the development of RF/microwave systems is trending towards small size, multi-function, and frequency agility, which challenges RF filters with even more stringent requirements. As shown in Figure 1.1, in the last decade, filters with diverse characteristics, such as reconfigurable filters [1], [2], lossy filter [3], filter-antenna [4], balun-filter, and active filter [5], have been widely reported to meet new requirements.

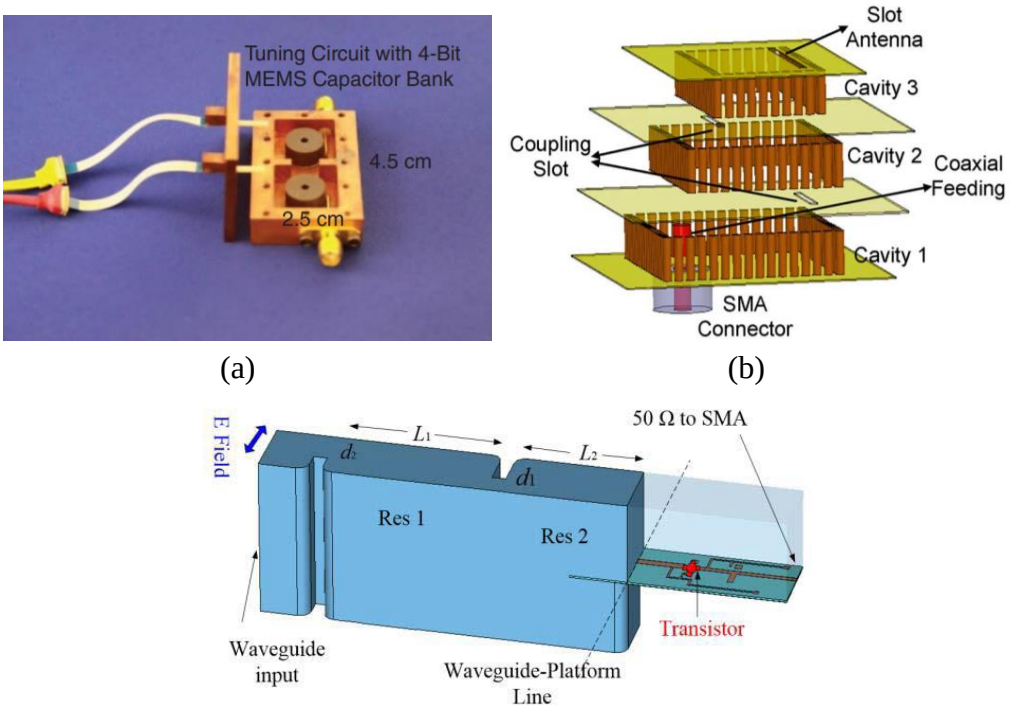

(a) (b)

(c)

Figure 1.1 (a) MEMS based tunable dielectric resonator filter [2]; (b) Filter-antenna [4]; (c) Filter-amplifier [6].

In satellite transponders, high quality-factor (Q-factor) resonator filters based on cavities or dielectric resonators are required for the output which have crucial requirements for insertion loss and power handling. At the receiver end, however, the insertion loss and power handling performances are less critical. For the receiver filters, the challenge is lying in designing a compact bandpass filter with frequency flexibility, flat in-band responses and high selectivity.

The frequency agility of filters is attractive and has been widely discussed with mechanical tuning components, varicaps, and RF switches [1], [2], [7]. The general benefits of the reconfigurable filter can be summarised as:

- High efficiency and flexibility in spectrum usage.
- The number of RF filters can be reduced.
- Size reduction and low complexity for the system.
- Capability of working in complex environments.
- Software-defined.

In recent years, there are ever more stringent demands for reconfigurable filters with high selectivity, high degree, compact size, fast reconfiguration speed, and low insertion loss.

High selectivity of the passband can be achieved by introducing band-side transmission zeros in stopbands. In a conventional way, cross-coupling between non-adjacent resonators or I/O port of the filter by folding the filter is adapted to create the band-side transmission zeros, resulting in a quasi-elliptic function response. But the folded configuration would lead to difficulty of deploying tuning components into the filter resonator. What is also concerned is the reservation for transmission zeros when the filter is tuned.

Varactor tuned planar bandpass filters are most attractive thanks to its advantages of high tuning speed, small size, continuous tuning ability, low power consumption, and low cost. However, high losses of the substrate-structure and varactor diodes have seriously degraded the performances of varactor-tuned planar filters. Therefore, practical filter-performance-enhancement methods are highly desired.

1.2 Objectives

Following our motivation, the primary objective of the dissertation is to introduce tunable filters with improved performance. We aim to carry out the following tasks:

- To develop high-order bandpass filters with frequency/bandwidth reconfigurable abilities using varactor diodes.
- To build in-line filter configurations with high selective responses.
- To investigate solutions to overcome the performance degradation caused by the low quality-factor of filters.

1.3 Organisation

This thesis is formed by 6 chapters. Following the introduction, Chapter 2 presents a review of state-of-the-art tunable filter techniques and performance enhancement techniques for high loss filter.

In Chapter 3, a 4-pole dual-mode resonator microstrip filter is demonstrated with nonuniform-quality-factor (nonuniform-Q) distribution to improve the passband flatness. The tunability of the filter is accomplished by loading varactors on resonators. Thanks to the feature of dual-mode resonators, two transmission zeros are observed at two sides of the passband. The methodology of coupling matrix synthesis is introduced to characterise the tunable lossy filter. The experimental results of this type of tunable lossy filter have shown a good passband flatness and high selectivity during the bandwidth and frequency tuning.

Chapter 4 presents a type of bandwidth tunable bandpass filter with 5-pole high selective responses. A cascaded dual-behaviour resonator contributes controllable transmission zeros at two sides of the passband. Based on the concept of the resistive cross-coupling technique, a novel lossy technique called centre-loaded resistive cross-coupling configuration is developed to enhance the passband flatness of the tunable filter. At 2% fractional bandwidth (FBW) bandwidth state, the tunable filter has an in-band insertion loss variation of only 1 dB. The experimental results of the filter are presented.

In chapter 5, the research focuses on the development of a tunable active filter with constant absolute bandwidth at C band frequency. The presented active circuit can provide adjustable negative resistance in a wide frequency range to compensate the loss of the tuned resonator. Circuit modelling for the active circuit is presented to predict the negative resistance. A 2-pole frequency tunable filter is demonstrated experimentally, and good insertion loss compensation can be observed over the frequency tuning range.

Finally, a summary of presented works and suggestions for future works are concluded in Chapter 6.

1.4 Reference

[1] J. s Hong, 'Reconfigurable Planar Filters', *IEEE Microwave Magazine*, vol. 10, no. 6, pp. 73–83, Oct. 2009.

[2] R. R. Mansour, F. Huang, S. Fouladi, W. D. Yan, and M. Nasr, 'High-Q Tunable Filters: Challenges and Potential', *IEEE Microwave Magazine*, vol. 15, no. 5, pp. 70–82, Jul. 2014.

[3] A. C. Guyette, I. C. Hunter, and R. D. Pollard, 'The Design of Microwave Bandpass Filters Using Resonators With Nonuniform Q', *IEEE Transactions on Microwave Theory and Techniques*, vol. 54, no. 11, pp. 3914–3922, Nov. 2006.

[4] H. Cheng, Y. Yusuf, and X. Gong, 'Vertically Integrated Three-Pole Filter/Antennas for Array Applications', *IEEE Antennas and Wireless Propagation Letters*, vol. 10, pp. 278–281, 2011.

[5] Young-Hoon Chun, Jae-Ryong Lee, Sang-Won Yun, and Jin-Koo Rhee, 'Design of an RF Low-noise Bandpass Filter using Active Capacitance Circuit', *IEEE Transactions on Microwave Theory and Techniques*, vol. 53, no. 2, pp. 687–695, Feb. 2005.

[6] Y. Gao, J. Powell, X. Shang, and M. J. Lancaster, 'Coupling Matrix-Based Design of Waveguide Filter Amplifiers', *IEEE Transactions on Microwave Theory and Techniques*, vol. 66, no. 12, pp. 5300–5309, Dec. 2018.

[7] F. Huang and R. R. Mansour, "Tunable Compact Dielectric Resonator Filters," *2009 European Microwave Conference (EuMC)*, Rome, Italy, 2009, pp. 559-562.

CHAPTER 2
FUNDAMENTAL THEORY & LITERATURE REVIEW

In general, fixed-frequency-response filters are a major bottleneck in modern wireless communication systems that gives rise to the demand for implementation of filters with tunability [1]. Electrical tuned planar filters are a popular technique due to its compact size, and easy integration with lumped elements. A well-known problem for the planar filter is the high loss caused by the limited quality factor of the resonator due to substrate loss. Various techniques have been proposed to overcome this problem to minimise the signal distortion due to the high loss in filters [3] – [5]. This chapter reports a review of state-of-the-art filter techniques in the aspect of tunable filter and filter performance enhancement from public resources. The fundamental theory of the planar filters is reviewed at the beginning.

2.1 Basic Theories of Filters

A conventional microwave filter is a two-port network used to control the frequency response at a certain point in an RF or microwave system. A filter frequency channels containing wanted signal and rejects undesired frequencies within the stopband. Obviously, filters play an essential role in the RF/microwave applications. The theory development of microwave filters can be traced back to the 1930's as the pioneers used the image parameters method to guide the low-frequency filter design [6], [7]. In the latest century, more accurate methods such as insertion loss method and coupling matrix method have been introduced based on prescribed frequency responses such as Butterworth response, Chebyshev response and Elliptic response [8], [9].

In order to develop the understanding of proposed works in this thesis, some basic concepts and theories of filter and tuning techniques are reviewed in this Section. The topic will cover the filter transfer function, filter network synthesis, filter parameters extraction.

2.1.1 Transfer Functions

The transfer function of a filter describes mathematically the transmission of the network response, also known as S_{21}. For a lossless passive filter network, the transfer function can be defined as [8]

$$\left|S_{21}(j\Omega)\right|^2 = \frac{1}{1+\varepsilon^2 F_n^2(\Omega)} \tag{2.1}$$

where ε is the ripple constant, Ω is the frequency variable, $F_n(\Omega)$ which is an n^{th}-order polynomial defines the characteristic function of the filter. Consequently, insertion loss of the filter can be calculated by

$$IL(\Omega) = 10\log\frac{1}{\left|S_{21}(j\Omega)\right|^2} \ \ (dB) \tag{2.2}$$

Filters exhibiting distinct frequency responses can be divided as several classical types including Butterworth (maximally flat) response, Chebyshev response, and Elliptic function response. An n^{th}-order lowpass Butterworth filter which has the insertion loss $IL = 3$ dB at the cutoff frequency $\Omega_c = 1$ has a transfer function of (2.3). This type of filter response provides a maximally flat at the frequency of $\Omega = 0$ as shown in Figure 2.1 (a).

$$\left|S_{21}(j\Omega)\right|^2 = \frac{1}{1+\Omega^{2n}} \tag{2.3}$$

The Chebyshev response filter is the most common type of filter in RF/microwave applications. It presents equal ripples L_{Ar} (dB) in passband as shown Figure 2.1 (b). The transfer function of a Chebyshev response can be expressed by (2.1), (2.4) and (2.5).

$$\varepsilon = \sqrt{10^{L_{Ar}/10} - 1} \tag{2.4}$$

$$F_n(\Omega) = \begin{cases} \cos(n\cos^{-1}(\Omega)) & |\Omega| \le 1 \\ \cosh(n\cosh^{-1}(\Omega)) & |\Omega| \ge 1 \end{cases} \tag{2.5}$$

Elliptic filter response, as shown in Figure 2.1 (c), is equal ripple in both the passband

and stopband in which case a better cut-off rate can be obtained [9]. Instead of the elliptic response, quasi-elliptic response filter with a single pair of attenuation poles at finite frequency is widely used for high-selectivity filtering. The characteristic function $F_n(\Omega)$ in (2.1) for the quasi-elliptic response filters could be expressed as (2.6) [10]. Ω_a is the attenuation pole frequency as seen in Figure 2.1 (d).

$$F_n(\Omega) = \cosh\left\{(n-1)\cosh^{-1}(\Omega) + \cosh^{-1}\left(\frac{\Omega\Omega_a - 1}{\Omega_a - \Omega}\right) + \cosh^{-1}\left(\frac{\Omega\Omega_a + 1}{\Omega_a + \Omega}\right)\right\} \quad (2.6)$$

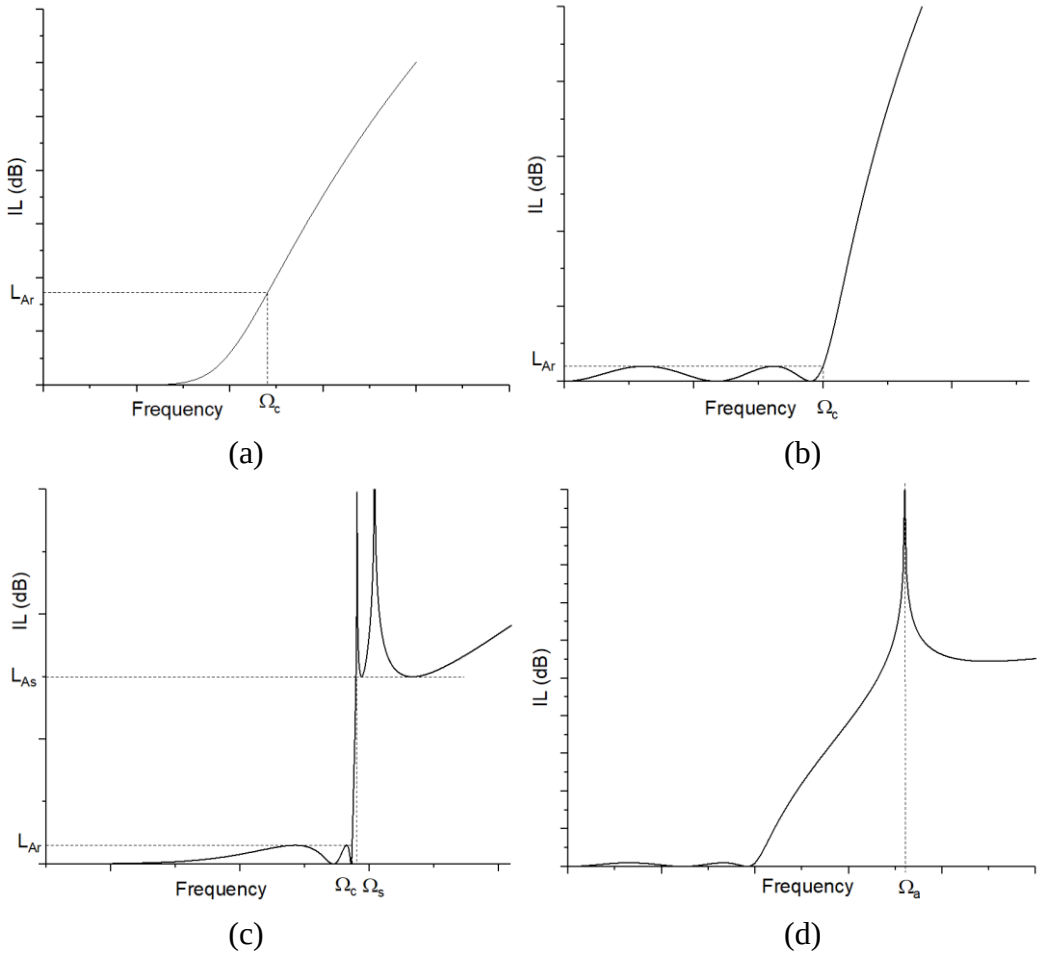

Figure 2.1 Typical filter responses. (a) Butterworth response; (b) Chebyshev response; (c) Elliptic function response; (d) Quasi-elliptic response.

2.1.2 Filter Network Synthesis

2.1.2.1 Lowpass Prototype Filters

Low pass prototype filters are usually used to synthesis the filter transfer functions [7],

[8]. In general, a low pass prototype filter is defined as a filter with normalised element values which make the source resistance or conductance equal to one $g_0 = 1$ and the cut off frequency to $\Omega_c = 1\ (rad/s)$. Figure 2.2 shows a possible form of an nth-order lowpass prototype. It should be indicated that g_i for $i = 1$ to n can be either series inductances or shunt capacitances but with the alternate sequence. g_0 and g_{n+1} are source/load resistance or conductance depending on the g_i and g_n. Element values in lowpass prototype for different transfer function can be obtained from many references [8], [9].

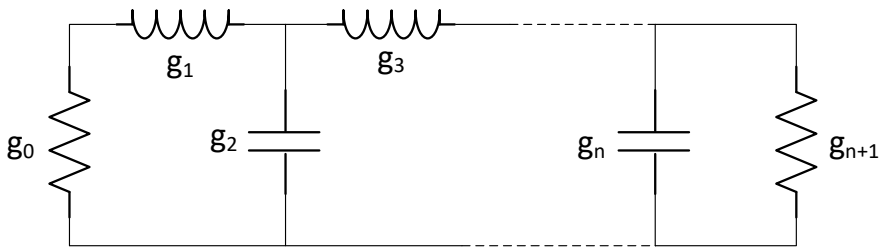

Figure 2.2 Lowpass prototype filter with a ladder network structure.

2.1.2.2 Filter with Immittance Inverters

Immittance inverters are either impedance (K) or admittance (J) inverters which ideally have a unique property at all frequencies. For any termination impedance Z_2, an impedance inverter K will switch the input impedance Z_1 between conductive and inductive by

$$Z_1 = \frac{K^2}{Z_2} \tag{2.7}$$

Apparently, an inverter has a phase shift of $\pm 90°$. The ABCD matrix of an impedance inverter can be expressed as

$$\begin{bmatrix} A & B \\ C & D \end{bmatrix} = \begin{bmatrix} 0 & \mp jK \\ \pm \dfrac{1}{jK} & 0 \end{bmatrix} \tag{2.8}$$

Similarly, an ideal admittance inverter has the admittance transform function of (2.9) and ABCD matrix of (2.10)

$$Y_1 = \frac{J^2}{Y_2} \tag{2.9}$$

$$\begin{bmatrix} A & B \\ C & D \end{bmatrix} = \begin{bmatrix} 0 & \pm\dfrac{1}{jJ} \\ \mp jJ & 0 \end{bmatrix} \tag{2.10}$$

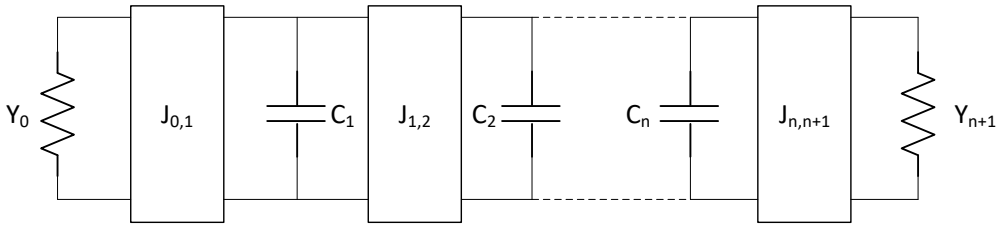

$$J_{0,1} = \sqrt{\frac{Y_0 C_{a1}}{g_0 g_1}}\ ,\ J_{i,1+1} = \sqrt{\frac{C_{ai} C_{a(i+1)}}{g_i g_{i+1}}}\Bigg|_{i=1 to n-1}\ ,\ J_{0,1} = \sqrt{\frac{C_{an} Y_{n+1}}{g_n g_{n+1}}}$$

(a)

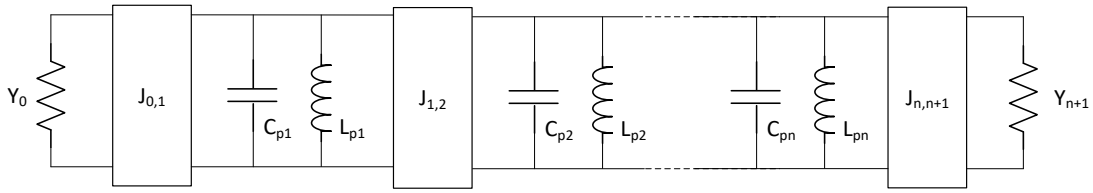

$$J_{0,1} = \sqrt{\frac{Y_0 FBW\omega_0 C_{p1}}{\Omega_c g_0 g_1}}\ ,\ J_{i,i+1} = \frac{FBW\omega_0}{\omega_c}\sqrt{\frac{C_{pi} C_{p(i+1)}}{g_i g_{i+1}}}\ ,\ J_{n,n+1} = \sqrt{\frac{Y_{n+1} FBW\omega_0 C_{pn}}{\Omega_c g_n g_{n+1}}}\ ,$$

$$L_{pi} = \frac{1}{\omega_0^2 C_{pi}}\Bigg|_{i=1 to n}$$

(b)

Figure 2.3 (a) Lowpass prototype filters modified with admittance inverters; (b) Bandpass prototype filter with J inverters.

By employing lowpass to bandpass transformation and admittance inverter, the general lowpass prototype in Figure 2.2 can be transformed into a bandpass filter prototype composed of LC resonators and J inverters, shown in Figure 2.3, where Y_0 and Y_{n+1} are the characteristic admittances of source/load, Ω_c is the normalised cut-off frequency, C_{pi} maybe chosen arbitrarily which would result in the identical filter response defined by the original prototype.

2.1.2.3 Equivalent Circuit Synthesis

As discussed above, a bandpass filter with certain transmission function can be synthesised by an equivalent circuit composed by LC elements and immittance inverters (impedance inverter K or admittance inverter J). In many practical cases, equivalent circuit synthesises are performed with commercial CAD tools. As an example, a 4-pole bandpass filter with a quasi-elliptical response is demonstrated with an equivalent circuit. The initial elements' values for the lowpass prototype filter can be found in [10] as

$$g_1 = 0.95974\ ,\ g_2 = 1.42192\ ,\ J_1 = -0.21083\ ,\ J_2 = 1.11769$$

$$\begin{aligned} Q_e &= \frac{g_1}{FBW} \\ M_{i,i+1}, M_{n-i,n-i+1} &= \frac{FBW}{\sqrt{g_i g_i}} \quad for \quad i = 1 \quad to \quad m-1 \\ M_{m,m+1} &= \frac{FBW \cdot J_{\mathrm{m}}}{g_{\mathrm{m}}},\ M_{m-1,m+2} = \frac{FBW \cdot J_{\mathrm{m\text{-}1}}}{g_{\mathrm{m\text{-}1}}} \quad \ldots \end{aligned} \tag{2.11}$$

The chosen lowpass prototype provides transmission zeros at $\Omega = \pm 1.8$ for the selectivity purpose. Therefore, the design parameters of the bandpass filter with a fractional bandwidth (FBW) of 0.05 can be determined by equations (2.11) as follows:

$$\mathrm{Q_e} = 19.19,\ \mathrm{M_{12}} = 0.0428,\ \mathrm{M_{23}} = 0.0393,\ \mathrm{M_{14}} = -0.01098$$

The commercial software AWR Microwave Office is used here for the filter synthesis. The schematic circuit, shown in Figure 2.4 (a), is composed of lumped RLC resonators and $\pm 90°$ transmission-line inverters at centre frequency f_0, where the positive and negative phase differences of the quarter-wavelength inverter are defined by the signs of the coupling coefficient representing the coupling types. Impedances of the quarter-wavelength inverter produce the coupling magnitudes.

The corresponding values of RLC resonator parameters for the bandpass filter can be calculated by

$$C_0 = \frac{Q_e}{\omega_0 Z_0} \times 10^{12} \left(pF \right)$$
$$L_0 = \frac{Z_0}{\omega_0 Q_e} \times 10^{9} \left(nH \right) \tag{2.12}$$
$$R_Q = Z_0 \frac{Q_u}{Q_e} \left(\Omega \right)$$

In the meanwhile, inverters' impedances can be found by

$$Z_{01} = Z_0$$
$$Z_{i,i+1} = \frac{Z_0}{\left| M_{i,i+1} \right| Q_e} \tag{2.13}$$

where Z_0 is the terminal impedance at ports, ω_0 (rad/s) is the angular frequency at the filter centre frequency, Q_u is the unloaded quality factor of filter resonators which is ideally infinite. In this case, the filter centre frequency is allocated at 2GHz, accordingly, the pair of transmission zeros are allocated at frequencies of 1.82GHz and 2.18GHz. The calculated design parameters obtained by (2.12), (2.13) are

$$\mathrm{Z_{01}} = 50,\ \mathrm{Z_{12}} = 60.86,\ \mathrm{Z_{23}} = 66.28,\ \mathrm{Z_{14}} = 237.2$$

$$\mathrm{C_0} = 30.55(\mathrm{pF}),\ \mathrm{L_0} = 0.2073(\mathrm{nH}),\ \mathrm{R_Q} = \infty$$

The synthesised results of filter equivalent circuit with the parameters of the above elements are shown in Figure 2.4 (b). The frequency responses meet the design specifications with 5% fractional bandwidth and a pair of transmission zeros.

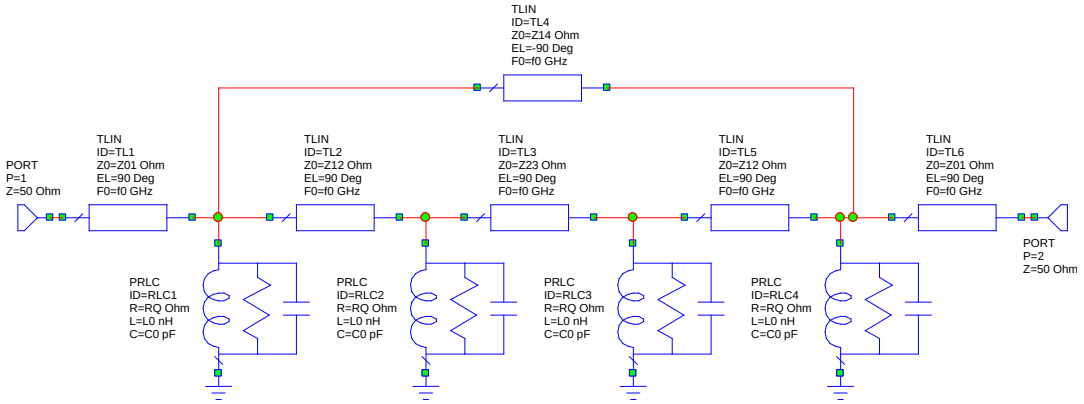

(a)

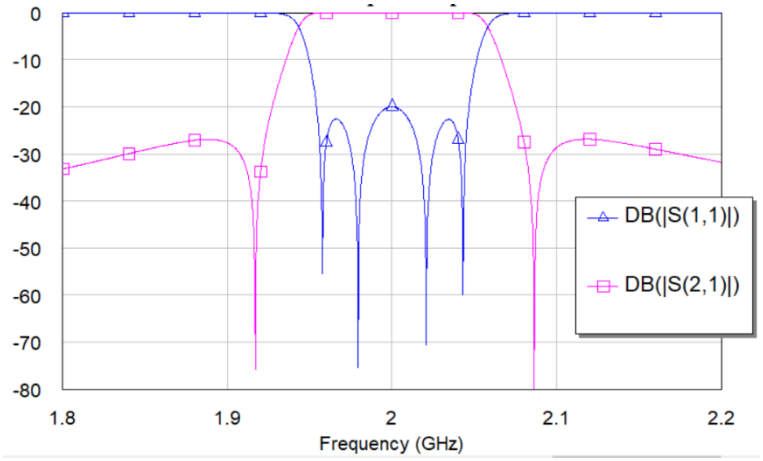

(b)

Figure 2.4 (a) Schematic circuit in AWR Microwave Office for the synthesis of a 4-pole quasi-elliptic response filter; (b) Frequency response for the filter at 2GHz.

2.1.2.4 Coupling Matrix Synthesis

The coupling matrix, as another popular synthesis method for the filter design, mathematically characterises the coupled-resonator filter topologies. For an nth-order filter, the filter network can be represented by an n+2 coupling matrix as (2.14) including the couplings from the source/load terminations to the resonator nodes.

$$\begin{bmatrix} m_{SS} & m_{S1} & \cdots & m_{Sn} & m_{SL} \\ m_{1S} & m_{11} & \ddots & \ddots & m_{1L} \\ \vdots & \ddots & \ddots & \ddots & \vdots \\ m_{nS} & \ddots & \ddots & m_{nn} & m_{nL} \\ m_{LS} & m_{L1} & \cdots & m_{Ln} & m_{LL} \end{bmatrix} \tag{2.14}$$

The filter synthesised by the equivalent circuit in the previous section is now expressed by the coupling matrix as:

$$\begin{bmatrix} 0 & 1.0209 & 0 & 0 & 0 & 0 \\ 1.0209 & 0 & 0.856 & 0 & -0.2196 & 0 \\ 0 & 0.856 & 0 & 0.786 & & 0 \\ 0 & 0 & 0.786 & 0 & 0.856 & 0 \\ 0 & -0.2196 & 0 & 0.856 & 0 & 1.0209 \\ 0 & 0 & 0 & 0 & 1.0209 & 0 \end{bmatrix} \tag{2.15}$$

Matrix elements in (2.15) are normalised elements which can be calculated by (2.16)

[9], where m_{ij} is the normalised coupling coefficient between filter nodes, m_{Si} is the normalised coupling coefficient from terminations to nodes, M_{ij} is the coupling coefficients.

$$m_{ij} = \frac{M_{ij}}{FBW}$$
$$m_{Si} = \frac{1}{\sqrt{Q_{e,i} \cdot FBW}} \tag{2.16}$$

Now, the filer frequency responses in terms of S-parameters can be calculated by

$$S_{21} = -2j[A]^{-1}_{n+2,1}$$
$$S_{11} = 1 + 2j[A]^{-1}_{1,1} \tag{2.17}$$

$$[A] = [m] + \Omega[U] - j[q] \tag{2.18}$$

$$\Omega = \frac{1}{FBW}\left(\frac{\omega}{\omega_0} - \frac{\omega_0}{\omega}\right) \tag{2.19}$$

where $[A]$ is the immittance matrix, [U] is an $(n+2) \times (n+2)$ identity-like matrix with only $[U]_{11} = [U]_{n+2,n+2} = 0$, $[q]$ is the $(n+2) \times (n+2)$ zero matrix, but $[q]_{11} = [q]_{n+2,n+2} = 1$, ω_0 is the centre frequency of the filter.

The coupling matrix calculation for a filter with a centre frequency of 2GHz and FBW = 0.05 is completed by Matlab as shown in Figure 2.5. The synthesised frequency responses match the results presented by equivalent circuit simulation in Figure 2.4.

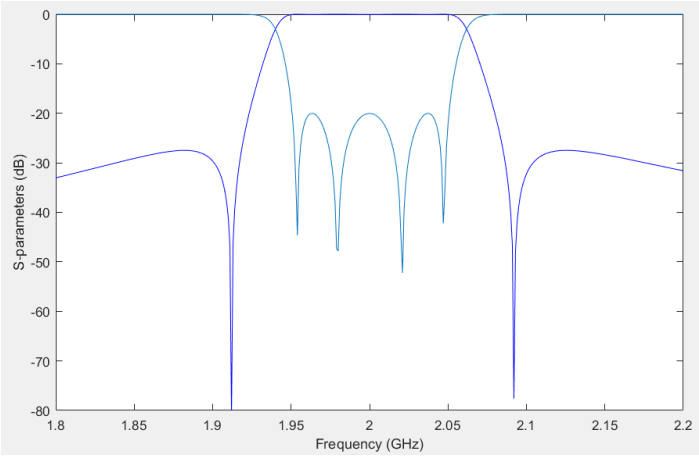

Figure 2.5 Synthesised filter response.

2.1.3 Filter Parameters Extraction

2.1.3.1 Coupling Coefficients Extraction

Commercial EM simulators allow designers to decompose the filter design into separate parts. Therefore, design parameters extraction becomes achievable by simulating different parts individually. Figure 2.6 (a) shows an arrangement for the coupling coefficient extraction for coupled resonators. The coupled resonators are very weakly fed by a port at each side. Frequency response is performed by the Sonnet simulator as shown in Figure 2.6 (b). Two resonating peaks caused by the coupling can be observed with very low levels of S21.

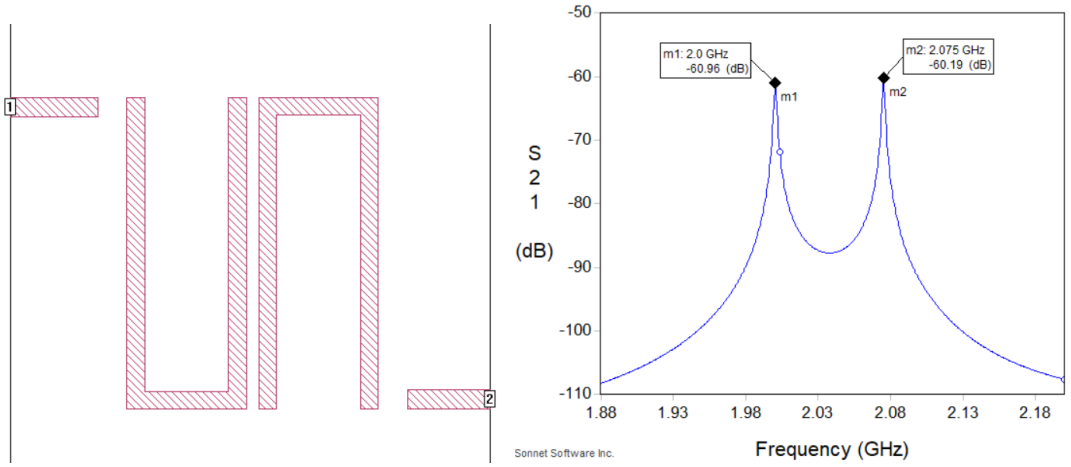

(a) (b)

Figure 2.6 Coupling coefficient extraction, (a) EM arrangement; (b) Coupled resonators response.

The general equation for the coupling coefficient extraction is (2.20), where f_{r1}, f_{r2} are two resonators' self-resonating frequencies, f_1, f_2 are frequencies of extracted peaks. For a pair of synchronously tuned coupled resonators, two resonators have the same self-resonating frequency $f_{r1} = f_{r2}$. The extraction equation can be simplified to (2.21). The sign of the coupling coefficient is depending on whether it is capacitive or inductive. Thus, the coupling coefficient in Figure 2.6 (b) can be calculated as 0.0368.

$$M_{12} = \pm\frac{1}{2}\left(\frac{f_{r2}}{f_{r1}} + \frac{f_{r1}}{f_{r2}}\right)\sqrt{\left(\frac{f_2^2 - f_1^2}{f_2^2 + f_1^2}\right)^2 - \left(\frac{f_{r2}^2 - f_{r1}^2}{f_{r2}^2 + f_{r1}^2}\right)^2} \tag{2.20}$$

$$M_{12} = \pm \frac{f_2^{\,2} - f_1^{\,2}}{f_2^{\,2} + f_1^{\,2}} \tag{2.21}$$

2.1.3.2 External Q Extraction

A configuration for the external-Q extraction is exhibited in Figure 2.7 (a). The resonator is excited by a single port resulting in the group delay and phase of S11 shown in Figure 2.7 (b). The resonating frequency can be located at the peak of the group-delay response as 4.797 ns at 2.042 GHz. The external Q of the feeding configuration in Figure 2.5 (a) can be obtained as $Q_e = 15.38$ by (2.22) which is discussed in the [8], where $\tau_{S11}(\omega_0)$ is the group delay at the resonating frequency of $\omega_0\,(rad/s)$. Alternatively, Q_e can also be determined by equation (2.23) that the resonating frequency ω_0 is divided by the bandwidth of $\pm 90°$ phase shifts with respect to the phase at ω_0. The calculated value of Q_e by (2.23) is 15.95 which matches the result from (2.22).

$$Q_e = \frac{\omega_0 \cdot \tau_{S11}(\omega_0)}{4} \tag{2.22}$$

$$Q_e = \frac{\omega_0}{\Delta\omega_{\pm 90^\circ}} \tag{2.23}$$

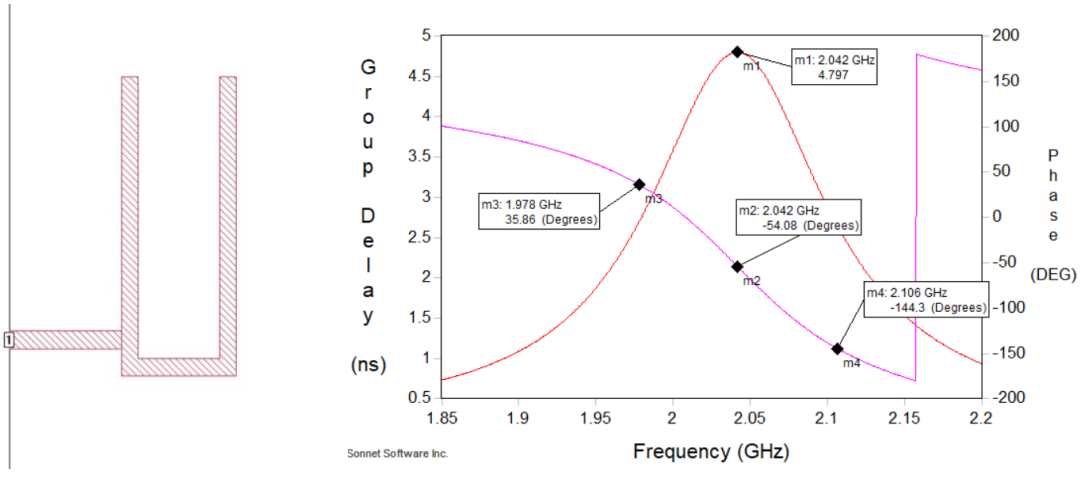

(a) (b)

Figure 2.7 External Q_e extraction, (a) Excitation port; (b) Frequency responses in terms of group delay and phase differences.

2.1.3.3 Unloaded Q Extraction

The unloaded quality factor Q_u of a resonator is another important parameter in this thesis that indicates the loss within a resonator. The extraction for unloaded Q of a resonator can be done by a similar configuration as the coupling coefficient extraction, that two ports excite the measured resonator very weakly, shown in Figure 2.8 (a). The Q_u can be estimated through the S21 response using equation (2.24). $\Delta\omega_{3dB}$ is the bandwidth of the 3-dB attenuation from the resonating peak. In the case of Figure 2.8 (b), the unloaded quality factor is given as $Q_u = 156$.

$$Q_u = \frac{\omega_0}{\Delta\omega_{3dB}} \tag{2.24}$$

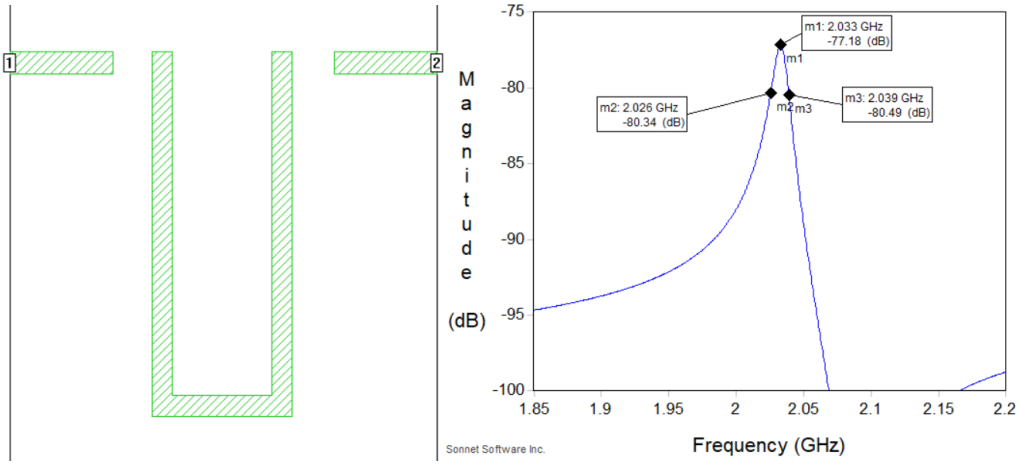

(a) (b)

Figure 2.8 Unloaded Q extraction for the resonator, (a) Extraction layout; (b) S21 response.

2.2 Literature & Techniques Review

The emphasis of this review has been put on reconfigurable techniques, lossy filter techniques, and performance-enhancement techniques in filter applications. The chapter contains several parts including:

- Overview of reconfigurable techniques
- Tunable filters
    - Frequency reconfiguration
    - Bandwidth reconfiguration

- Active filters
- Lossy filter techniques
    - Non-uniform Q distribution
    - Resistive cross-couplings (RCCs)

2.2.1 Overview of Reconfigurable Techniques

Tunable bandpass filters are desirable in modern communication systems and have been widely discussed for years. In open works of literature, microwave tunable filter can be realised by various techniques categorised as discrete tuning and continuous tuning. PIN diodes and MEMS (Microelectromechanical System) switches are the main techniques used for discrete tuning. Meanwhile, for tuning continuously, mechanical tuning techniques, varactor diodes, MEMS capacitors, and Barium Strontium Titanate (BST) varactors can be applied.

Mechanical tuning techniques are the early approach in filter reconfiguration. Such a method physically moves a part in a cavity resonator to affect the resonating frequency or inner coupling of the filter. [11], [12] present cavity filters with frequency tuning ability controlled by step-motor/positioner. Moreover, piezoelectric transducers or actuators are used instead to achieve the filter reconfiguration in [13], [14]. As piezoelectric materials can convert electrical energy into mechanical displacement base on the piezoelectric effect, movement of flexible cavity sidewalls is accomplished by simply varying the applied DC voltage. Hence, filter tuning can be achieved. Generally, mechanically tuned filters offer excellent performances of high-Q, high linearity and high-power handling. However, their bulky size and limited tuning speed are the main concerns in many applications.

The integrations of RF MEMS and planar filters have been demonstrated in [15], [16]. RF MEMS devices, such as MEMS switches and MEMS varactors, adopt micro-mechanical movement to achieve tuning or switching functions. They have advantages in small size, low loss, and high linearity. The application frequency of MEMS is up to 100 GHz which is also attractive for the modern RF/microwave application. On the other side, RF MEMS also has several concerns limiting its application such as high

driving voltage, hermetic packaging, and reliability.

Barium Strontium Titanate varactor/capacitor is the most developed ferroelectric material in RF tunable applications at room temperature [17], [18]. Because of the high dielectric constant of the BST thin film, the varactor based on BST material has a compact size. They can be designed in the forms of a metal-insulator-metal or an interdigital capacitor. The BST thin film offers a dielectric constant variation (typically $\varepsilon_r = 700 - 1200$) with an applied DC electric field. The BST varactor can change with nanosecond speeds so that they can be widely used in tunable RF/microwave designs. However, the high loss of BST varactor has been the main issue limiting their uses. Recent years, BST-varactor products with better quality factors have been released on the market [19], but those BST-varactors are restricted by their operation frequency (below 3GHz).

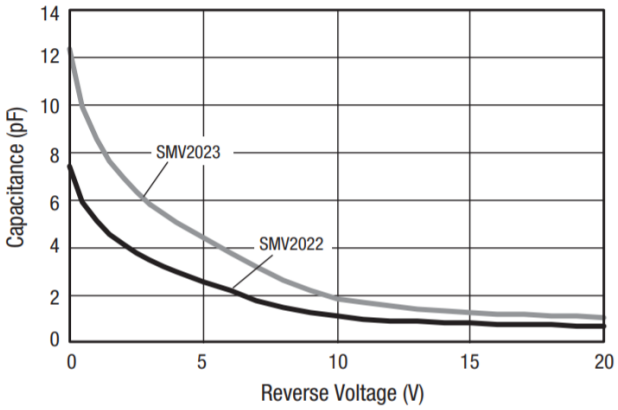

Figure 2.9 Typical voltage-capacitance curves of varactor diodes [20].

Semiconductor diodes including PIN diodes and varactor diodes have been widely implemented in RF and microwave circuit benefited from its promising performance and low cost. Generally, they perform a faster reaction speed than RF MEMS and piezoelectric transducers. A PIN diode contains an additional layer of an intrinsic or lightly doped semiconductor sandwiched between highly doped p and n layers [21]. Under forward bias, the insulator layer is suppressed until the current can be conducted, while the backward bias will boost the insulator layer and block the current flow. Therefore, PIN diode performances as an on/off switch in a circuit. A varactor diode can be created by a specific middle layer doping profile. Figure 2.9 shows a typical C-V curve of commercial varactor diodes [20]. The reverse bias changes the width of the

intrinsic layer resulting in a voltage-controlled variable capacitance. For RF/microwave frequency, the hyper-abrupt junction gallium arsenide (GaAs) diodes are more favourable because of their lower parasitic and higher Q. For example, the GaAs tuning varactor MA46580 series have applicable frequencies as high as 40GHz [22].

Table 2-1 summarizes the performances of those reviewed techniques in different aspects. A suitable technique can be selected by considering the tunable performance, size, cost, circuit complexity, power consumption and tuning speed.

Table 2-1 Comparison of Typical Tunable Technologies [23]

Techniques	**Q factor at 10GHz**	**Bias**	**Power consumption**	**Speed**	**Cost**	**Size**
Varactor Diode	10-30	< 25 V	Negligible	< 1 us	Low	Small
Pin Diode	Rs=1-4 ohm	< 10 V	10-20 mA	< 1 us	Low	Small
BST	20-100	< 25V	Negligible	< 1 us	Low	Small
Mechanical	High	N/A	High	> 10 us	High	Large
MEMs	>200	< 50 V	Negligible	> 10 us	Medium	Small
Piezoelectric-Actuator	>500	> 100 V	Negligible	>100 us	Medium	Medium

2.2.2 Equivalent Circuit of Varactor Diodes

Semiconductor diodes have become a mature technique for reconfigurable filters [23]. Varactor diode tuning techniques providing variable capacitances have the advantage in continuous tuning. To predict the diode performance precisely in simulations, in this section, the equivalent circuit modelling for a varactor is presented.

At high RF/microwave frequency, due to the small wavelength, the physical size of a varactor diode cannot be neglected anymore. A varactor diode would no longer act like an ideal capacitor, and the parasitic effects become significant. To describe the varactor

diode behaviours, the equivalent circuit model (SPICE model) is a common-used modelling tool for those diodes at higher frequency design. Figure 2.10 (a) shows an equivalent circuit of a commercially packaged varactor diode provided by SKYWORKS [20]. The circuit includes parasitic capacitance C_P and parasitic inductance L_S arising from the package. Moreover, a diode model and a resistor in series describe the behaviour of the diode die. The diode model predicts the diode die's behaviour against different biasing voltages while the resistance constructs the loss in the die. The parameter C_{JO} in the diode model is the variable junction capacitance of the diode die that C_{JO} has an initial value for each varactor diode. Such an equivalent circuit with diode model can be simulated in commercial software such as ADS, AWR Microwave Office. Figure 2.10 (b), (c) show the predicted capacitance against the frequency for the varactor-diode SKYWORKS SMV2019-040LF. It is notable that, at higher frequencies, parasitic effects heavily undermine the performance of the varactor. Hence, the available maximum frequency of a varactor needs to be evaluated when choosing a varactor diode.

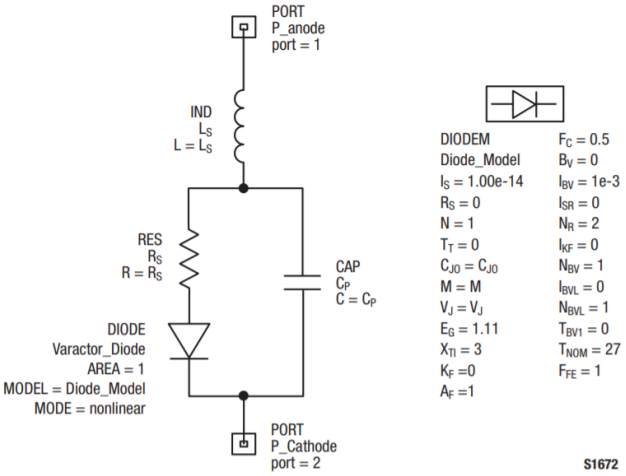

(a)

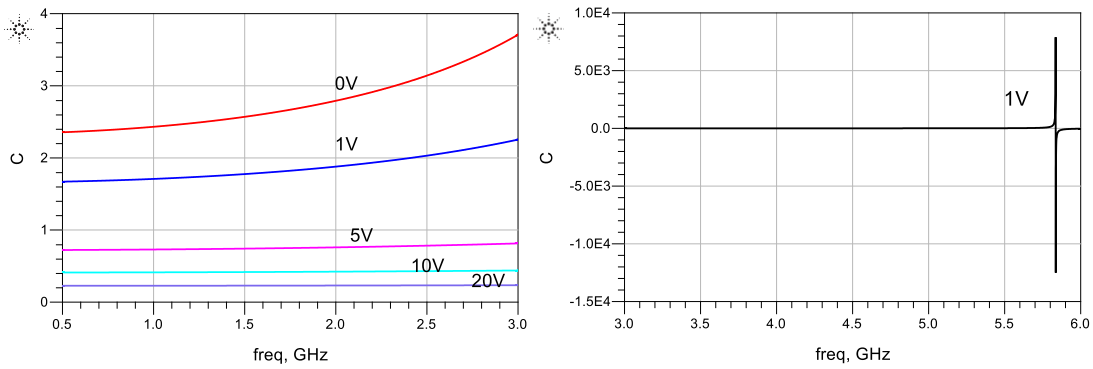

(b) (c)

Figure 2.10 (a) The equivalent circuit (SPICE model) for a varactor [20]; (b) Varactor capacitance against biasing voltage; (c) High-frequency response of the varactor.

Furthermore, the quality factor is another important characteristic for varactor diode as it measures the power dissipation in the diode die. At a relatively low frequency, the parasitic inductance/capacitance has a very limited effect on the circuit performance, and the loss caused by the varactor becomes the most concern. A simplified model of a varactor is shown in Figure 2.11 which is a more commonly used model in the simulation. The higher Q factor (lower R_s in the circuit) of the varactor diode can give better performance of filter loss. Most commercial varactor products claim that they have very high Q in the datasheet, for example, 3000 at 50 MHz [24]. However, their performances in the aspect of Q at our interesting frequencies L-C band are actually much lower, normally 10 – 80, because the Q is highly dependent on the operating frequency. For this reason, it is necessary to evaluate the Q of chosen varactors at operation frequencies in order to obtain accurate results in simulations.

Several methods can be considered to achieve accurate Q-factor or R_s of a varactor. As shown in Figure 2.10, the SPICE models cover the R_s information. In most cases, a user can directly obtain the SPICE models from manufacturers' websites. Those provided parameters are usually reliable and can be used to predict the actual behaviour of the varactor.

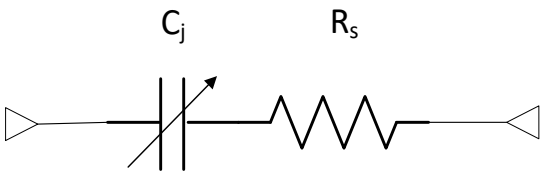

Figure 2.11 Simple model for a limited-Q RF varactor.

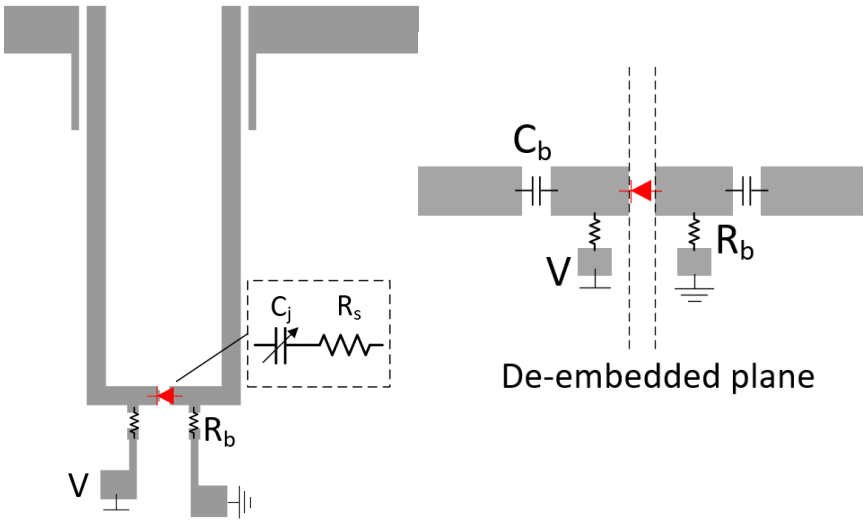

(a) (b)

Figure 2.12 Testing circuit for the R_s extraction. (a) Measurement with a loaded resonator; (b) De-embedded measurement.

However, for some causes, not all varactor models are available from the manufacturers. Experimental extraction for the Q factor (or resistance) and capacitance would be required. Figure 2.12 shows two types of the measurement configuration. The first method is testing the frequency responses of a varactor loaded resonator shown in Figure 2.12 (a). In EM simulations, the parameters R_s and C_j can be adjusted to make the resonator simulation responses approaching the measured responses. Therefore, the values of R_s and C_j are determined when the simulation responses match the measurements. The second manner in Figure 2.12 (b) is called De-embedded measurement. The varactor is soldered on a 50-ohm transmission line with its DC biasing circuit. The effects of the test fixture and DC biasing circuit can be removed by calibration methods such as TRL (Thru, Reflect, Line) method or port extension method. The S-parameters of the varactor diode is directly obtained. Further details of the quality factor extraction have been demonstrated in the Appendix.

2.3 Reconfigurable Filters

2.3.1 Frequency Reconfiguration

A frequency tuned compact planar filter would bring much flexibility to a device. In

general, the resonating frequency of a resonator is varying with electrical length while the coupling between two resonators provides a predictable fractional bandwidth. Therefore, a filter with frequency tuning is obtained by controlling the electrical length without coupling tuning. Many investigations have been focusing on the centre frequency tuning capability [15], [25]–[29] for the next generation of wireless systems [30].

2.3.1.1 PIN Diode Switchable Filter Bank

The PIN-diode is preferred in those applications where fast switching and moderate insertion loss are required. A 4-channel switchable filter bank based on PIN diodes was designed with a spurious suppression low pass filter (LPF) [25], shown in Figure 2.13 (a). Four bandpass filters in parallel designed on a suspended stripline substrate (SSS) have a bandwidth of 142.5 MHz. The centre frequencies of the filers are from 4.058 GHz to 4.4855 GHz with consecutive steps of 138 MHz, as shown in Figure 2.13 (b). The filter bank terminates with a lowpass filter which provides a spurious suppression up to 19 GHz. The measured resonator Q-factor is 580 while the passband insertion loss is from 3.3 to 3.8 dB. Two PIN-diode based SP4Ts (Single Pole 4 Throw) switches were employed for frequency reconfiguration. This switchable filter bank has a total current consumption of 60mA. In the meantime, the overall size of the filter reaches 95 *mm* × 101.6 *mm*.

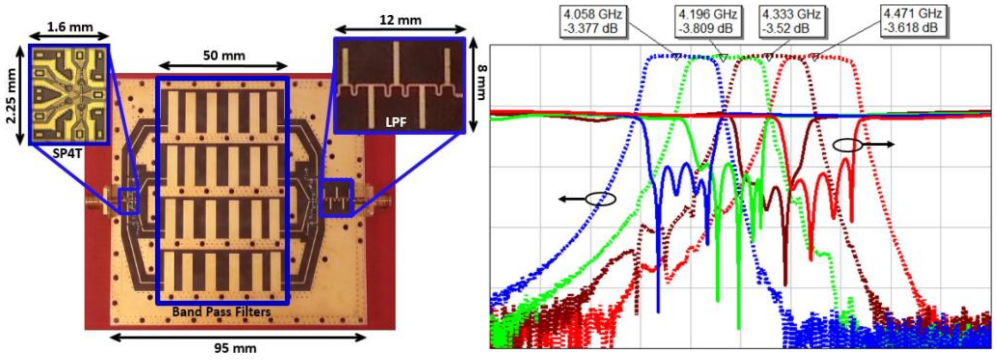

(a) (b)

Figure 2.13 (a) Structure of the 4-channel switchable filter bank with LPF; (b) Responses of the switchable filter. [25]

2.3.1.2 Varactor-tuned Combline Filter

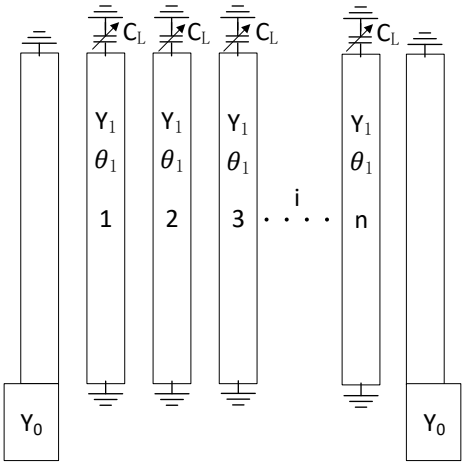

Figure 2.14 Schematic of a tunable combline filter [8].

Although the switchable filter bank shows a reliable performance in the frequency reconfiguration, the drawback of such technique is obvious as it has a large size. Varactor tuned filter shows its advantage in continuous tuning and small size. A typical varactor-tuned combline filter design analysis was demonstrated in the Chapter 13 of [8]. Short-circuit lines are loaded by the same capacitance of C_L, as shown in Figure 2.14. The input admittance of the capacitance loaded resonator is given by

$$Y_{in} = j\omega C_L + \frac{Y_1}{j\tan(\theta_1)} \tag{2.25}$$

where θ_1 is the electric length of the physical line at frequency ω, Y_1 is the admittance of the line. Thus, the resonating frequency can be found at the frequency $\omega = \omega_0$ that the input admittance of the resonator has $Y_{in} = 0$. The variation of the capacitance C_L will change the resonating frequency of the resonator, so the frequency tuning is achieved. Appropriate electrical length, loading capacitance, and line admittance can be chosen to achieve wanted resonator unloaded Q, tuning range and stopband bandwidth.

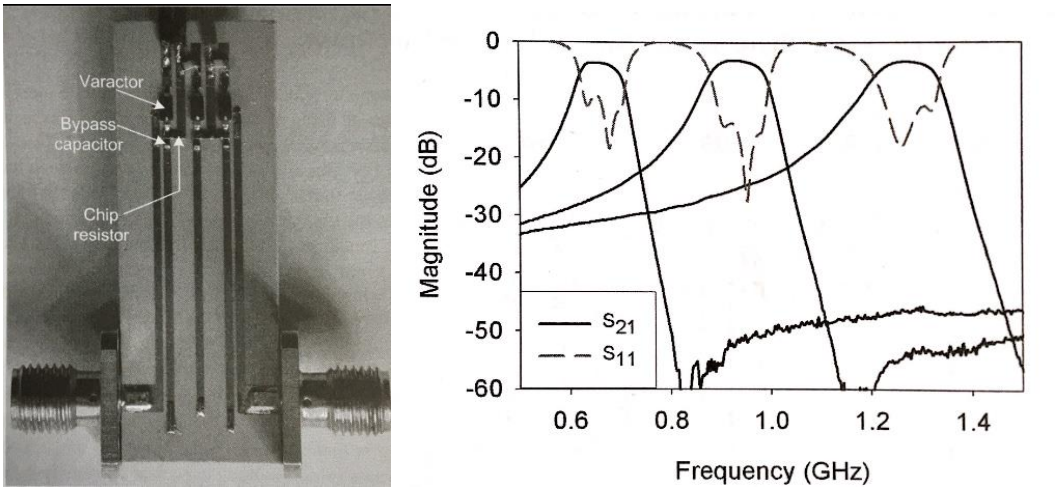

(a) (b)

Figure 2.15 (a) The varactor tuned combline filter; (b) Measurement results. [8]

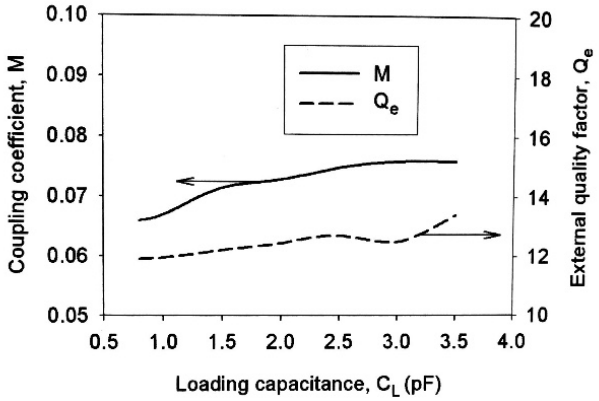

Figure 2.16 Extracted coupling coefficient and external Q as a function of loading capacitance for the combline filter [8].

An experimental filter is given in Figure 2.15 [8], where the filter is fabricated on a Rogers RO3003 substrate with a relative dielectric constant of 3 and a thickness of 1.02 *mm*. Practically, coupling coefficients between capacitance loaded resonators can be extracted by the weakly-feeding extraction method described in Section 2.1. As can be seen in Figure 2.16, the variation of extracted coupling coefficient and external Q is rather small. Therefore, a constant fractional passband bandwidth can be maintained during the frequency tuning. Surface mount varactor diodes (MA46H202-1088) which have a capacitance tuning range of 0.7 – 7 pF are used in capacitance loading for tuning. DC bias, consisted of bypass capacitors of 33 pF and chip resistors of 10 $k\Omega$, is varying from 3V to 20V. As a result, the centre frequency of the filter is tuned from 0.65 to 1.27

GHz with a middle band insertion loss of ~3.5 dB. A fractional bandwidth of 0.07 is roughly maintained during the tuning.

2.3.1.3 Tunable Combline Filter Using Step-Impedance Resonator

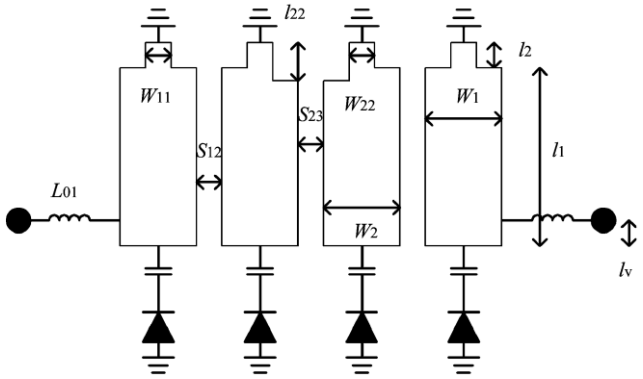

Figure 2.17. Varactor tuned combline filter using step-impedance microstrip lines [26].

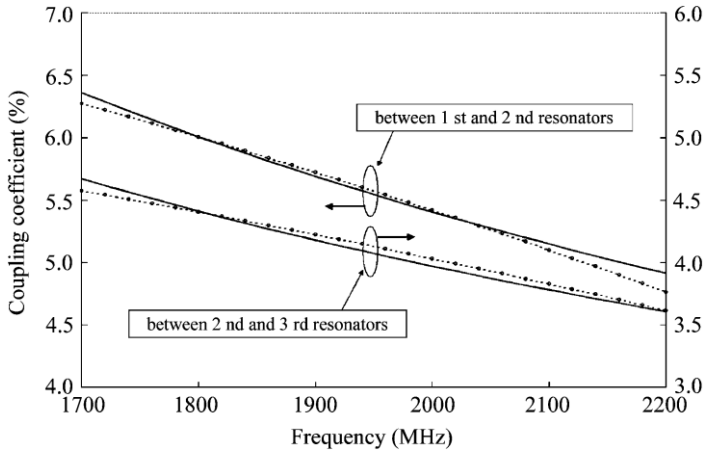

(a)

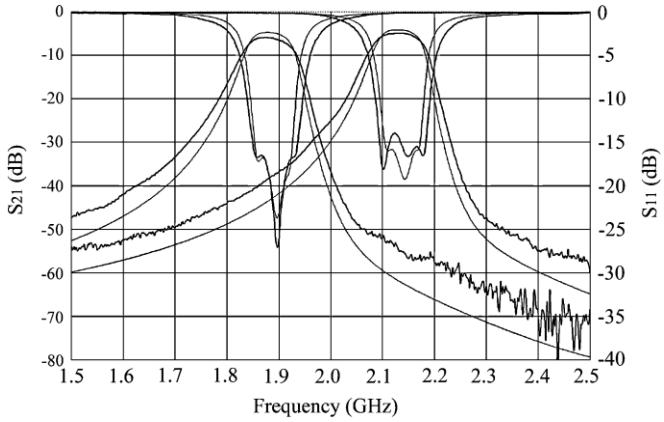

(b)

Figure 2.18 (a) Frequency variations of coupling coefficients, dot-line: achieved; Solid-line: required for constant ABW. (b) Simulated and measured results of the filter [26].

Preserving a constant absolute bandwidth (ABW) when the centre frequency is tuned is a well-known challenge in frequency tunable filter design. In general, to maintain a constant ABW, coupling coefficients need to vary inversely with the tuned centre frequency while the external Q factor is required to vary directly along with the frequency changing. Several techniques have been proposed in achieving constant ABW. In [26], step-impedance microstrip lines were employed to replace the uniform width lines, as shown in Figure 2.17. As the magnetic field is much concentrated near the short-circuited end on a resonator, the magnetic coupling reaches its maximum, while the electric coupling has the highest density at the opposite end. By allowing a larger gap near the short-circuited end, the magnetic coupling between resonators is reduced while the portion of the electric coupling is increased. In this manner, when the electromagnetic field on the microstrip line changes with the loading capacitance, the appropriate coupling coefficient variation required for the constant ABW can be produced as shown in Figure 2.18 (a). In addition, to obtain corresponding external Q factors during the tuning, a pair of lumped inductors are employed for the I/O feeding. The measurement results of the filter are given in Figure 2.18 (b). It can be observed that the 3 dB bandwidth of the tunable filter has an ABW of 100 MHz with a small variation of 3.2% within 250 MHz tuning range at 2GHz.

2.3.1.4 Frequency Tuned Filter with Transmission Zeros (TZ)

A. TZ Reconfiguration

Due to the increasing complexity of the modern communication systems, the selectivity of the RF tunable filter is concerned. In recent researches, tunable bandpass filters with transmission zeros become attractive thanks to its high selectivity [28], [29], [31].

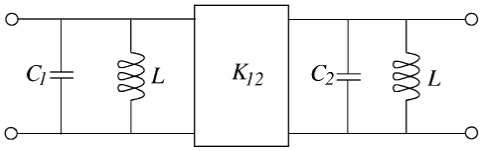

(a)

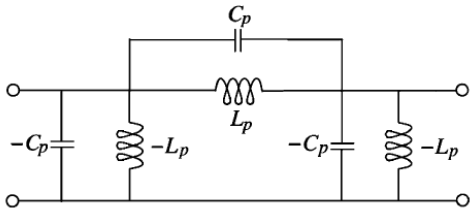

(b)

Figure 2.19 (a) A pair of coupled resonators, (b) an approximate model for the inverter with a TZ at finite frequency. [31]

In [31], a bandpass filter with a reconfigurable transmission-zero has been demonstrated. Considering a pair of coupled resonators who have the mixing coupling, the impedance inverter can be approximated as an LC equivalent circuit, such as the $-C_p$, $-L_p$, C_p and L_p shown in Figure 2.19. The negative shunt element could be further absorbed into the resonator LC equivalent circuit. This inverter has a coupling coefficient K_{12} and could generate an attenuation pole at its self-resonating frequency f_p.

$$f_p = \pm \frac{1}{2\pi\sqrt{L_p C_p}}$$
$$K_{12} = \frac{2\pi f_0 L_p}{1 - 4\pi^2 f_0^2 L_p C_p} \tag{2.26}$$

where f_0 is the centre frequency. Therefore, the coupling coefficient could be expressed in the term of the frequency of the transmission zero. It is seen from (2.27) that the lower side TZ leads to a negative coupling coefficient; a positive K_{12} leads to a TZ above the passband. Therefore, if a variable capacitance is used for the electric coupling capacitance C_p between two resonators, as shown in Figure 2.20 (a), the position of the transmission zero can be placed in either upper stopband or lower stopband while the inner-passband responses remain the same.

$$K_{12} = \frac{2\pi f_0 L_p}{1 - \left(f_0 / f_p\right)^2} \tag{2.27}$$

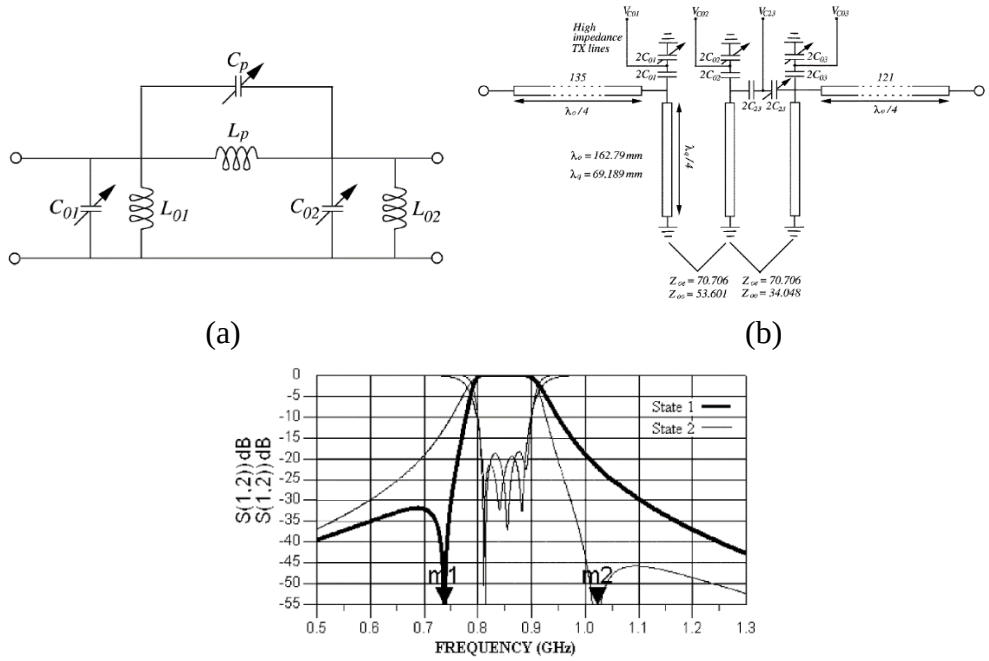

Figure 2.20 (a) Two coupled LC resonators with tunable capacitance; (b) Full layout of a proposed TZ reconfigurable bandpass filter based on the circuit in (a); (c) Simulated lossless filter responses. [31]

The full layout of a TZ reconfigurable combline filter is demonstrated in Figure 2.20 (b) in which coupling between second and third resonators is adjusted by varactors for TZ reconfiguration. As a result, the frequency of the transmission zero can be switched between 735.6 MHz and 1016.25 MHz to improve either upper side or lower side selectivity of the passband as shown in Figure 2.20 (c).

B. Frequency Tuned High Selective Filter

Frequency tuned filters with high selectivity have been widely discussed, in which filter responses have adjacent transmission zeros on each side of the passband. For example, such a high selectivity property is achieved by source-to-load cross (SL) coupling in [28]. Figure 2.21 shows a tunable filter composed of two folded short-circuited microstrip line resonators with back-to-back loaded varactors, where the back-to-back configuration of the loaded varactors can significantly improve the linearity performance of the tunable filter, illustrated in Figure 2.21 (c), (d). An electric SL coupling by a fixed capacitor C_{z1} gives a pair of transmission zeros. The short-circuited

ends of two resonators are coupled which produce a magnetic coupling path. Therefore, two band-side transmission zeros are introduced by two coupling paths with opposite properties. The input matching capacitors C_m are used to adjust the slope parameter of the coupled resonator. Thus, proper external coupling can be obtained.

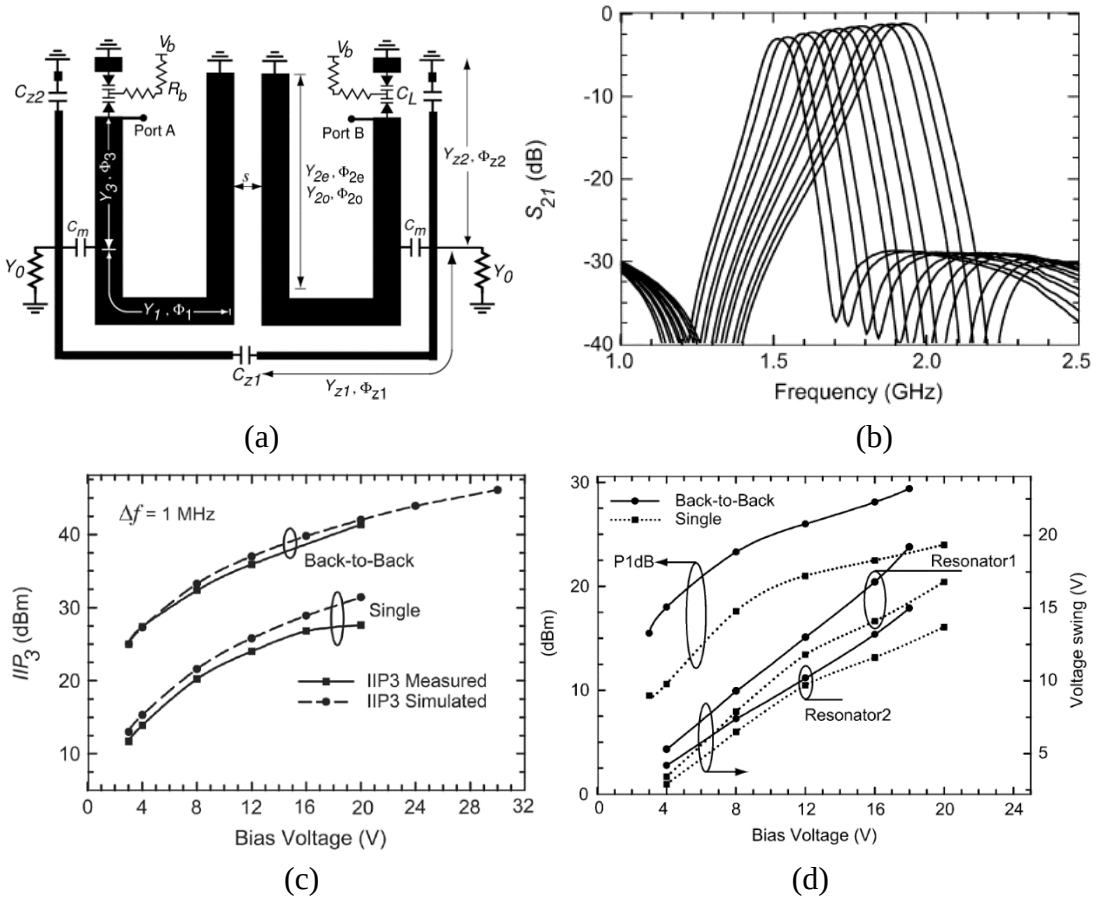

(a) (b)

(c) (d)

Figure 2.21 (a) Layout of the high selective tunable filter; (b) Frequency responses; (c) Improvement in IIP3; (d) Improvement in 1-dB compression point. [28]

The dual-mode microstrip resonator filter is attractive due to their compact size. Since each dual-mode resonator can perform as a doubly tuned resonator circuit, the number of resonators required for a given order of the filter is reduced by half compared with a conventional filter. A varactor-tuned dual-mode bandpass filter is introduced in [29]. A perturbation is loaded at the centre of a half-wavelength resonator exciting an additional mode on the resonator as shown in Figure 2.22 (a). Such a resonator has a distinct characteristic that two modes on the resonator are not coupled to each other. Figure 2.22 (b) shows the odd mode equivalent circuit where a virtual grounding is located at the middle of the half-wavelength resonator. On the other hand, a magnetic wall on the

line of the symmetry leads to the even mode equivalent circuit as shown in Figure 2.22 (c), so the second resonating frequency occurs. Additionally, an intrinsic transmission zero is found on the side of the even mode frequency enhancing the selectivity of the filter. The even mode frequency can be placed at either the upper or lower side in the passband by control the length of the loading. Consequently, the transmission zero will move to upper or lower stopband improving one side selectivity. Varactors are loaded at the open-ends of both the open-loop resonator and the loading element. In the manner of controlling the impedance ratio (line width) between the open-loop resonator and the perturbation line, frequencies of even and odd modes can be tuned synchronously by the same type of varactor. A constant ABW can be achieved during the frequency tuning while the number of control voltage remains single. Figure 2.23 shows the experiment of the tunable dual-mode filter where the transmission zero is placed in the upper stopband. The filter is tuned from 0.6 to 1.03 GHz with an absolute bandwidth of 85±5 MHz.

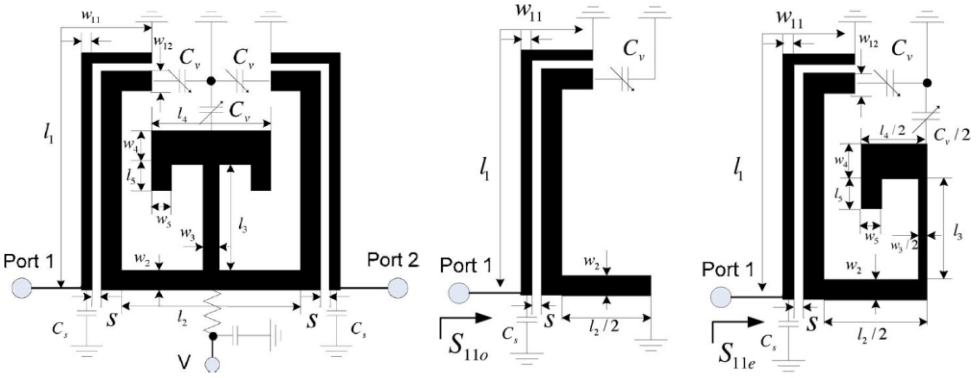

(a) (b) (c)

Figure 2.22 (a) Layout of a frequency tuned dual-mode filter; (b) Odd mode equivalent layout; (c) Even mode equivalent layout. [29]

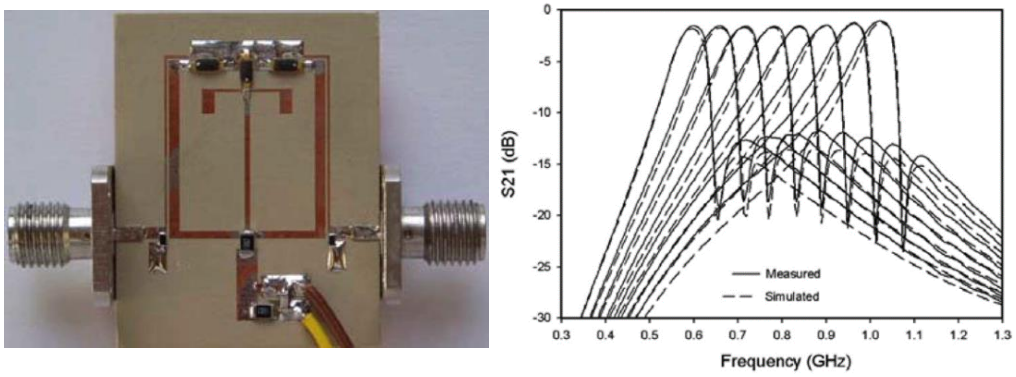

(a) (b)

Figure 2.23 (a) Fabrication; (b) Frequency result of the tunable dual mode filter. [29]

2.3.2 Bandwidth Reconfigurable

As we have seen, the reconfiguration of the centre frequency is mainly accomplished by varying the electrical length of filter resonators. In comparison, the bandwidth reconfiguration is challenging because of the lack of efficient methods to vary the inter resonator coupling electronically which is essential for bandwidth control. To tackle the challenge of bandwidth control, several techniques have been proposed [32]–[36].

2.3.2.1 Bandwidth Tuning by Interconnected Varactors

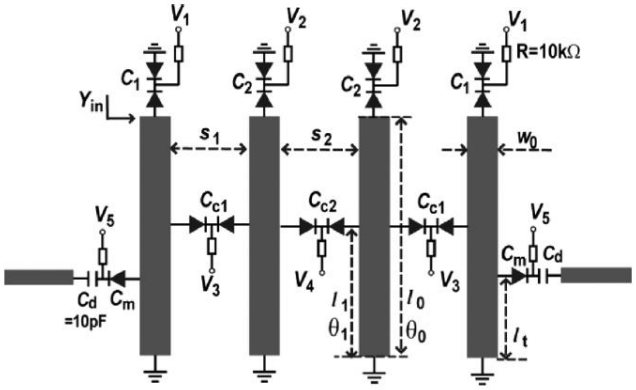

Figure 2.24 Layout of three-pole tunable filter with centre frequency and bandwidth control [33].

The coupling control between adjacent resonators has been demonstrated in [32], [33] by adding varactors across two resonators. Figure 2.24 shows a three-pole tunable combline bandpass filter with centre frequency and bandwidth control presented in [33]. Varactor loaded $\lambda/4$ resonators are connected by a back-to-back varactor pair and a short transmission line. The coupling between resonators can be analysed by the even/odd-modes equivalent circuits as shown in Figure 2.25. For the even mode equivalent circuit, the capacitance C_c across resonators has no effect on the circuit, while the capacitance $2C_c$ is shorted to the ground in the odd mode circuit. The varactor capacitance between resonators only changes the odd-mode frequency whereas the even-mode frequency is independent of C_c. Therefore, the asymmetric bandwidth tuning can be achieved by changing the interconnected varactors. To maintain the same centre frequency, centre frequency adjustment by the end-loaded varactors is required. The external coupling from the I/O ports is controlled in a similar way by tapping

varactor on the resonator. Subsequently, the results of filter bandwidth tuning are presented in Figure 2.26. The FBW of the filter can be tuned from 3% to 8% at 1.8 GHz.

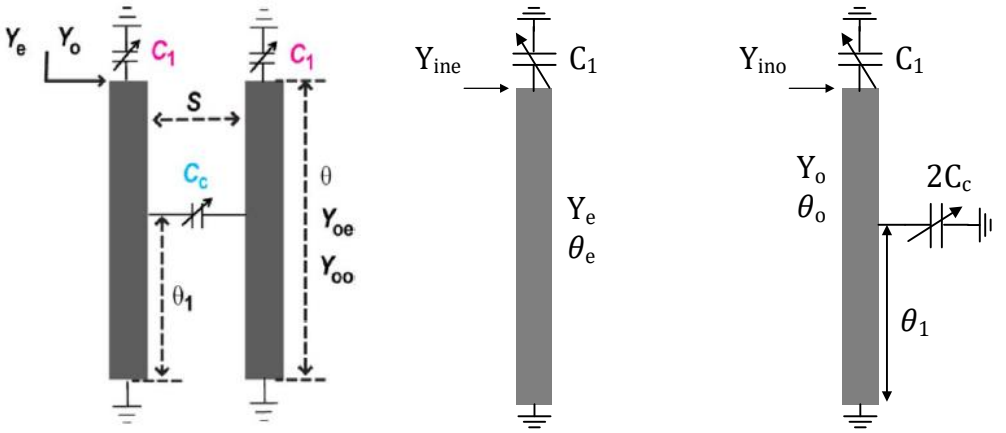

Figure 2.25 (a) Equivalent circuit model of adjacent resonators in Figure 2.26; (b), (c) Even and odd-mode equivalent circuits [33].

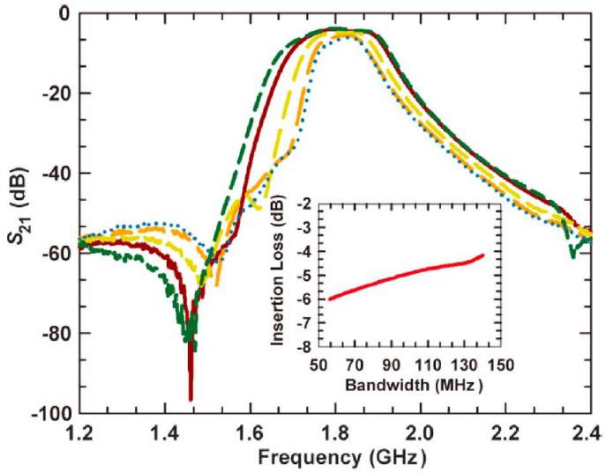

Figure 2.26 Bandwidth tuning of the 4-pole bandpass filter.

2.3.2.2 Tunable Filter using Variable Coupling Reducer

The coupling between resonators can also be controlled by adding non-resonating nodes called variable coupling reducers [34]. As can be seen in Figure 2.27, a varactor loaded segment whose resonating frequency is away from the filter passband is inserted between two coupled resonators. When the impedance of the coupling reducer is changed by the varactor, the coupling between the resonators is adjusted. In this way, the bandwidth of the filter is controlled. The filter layout and performance of bandwidth

tuning is shown in Figure 2.28. Asymmetrical bandwidth tuning can be achieved by varying the impedance of coupling reducers. Centre frequency adjustment is required to maintain a fixed centre frequency.

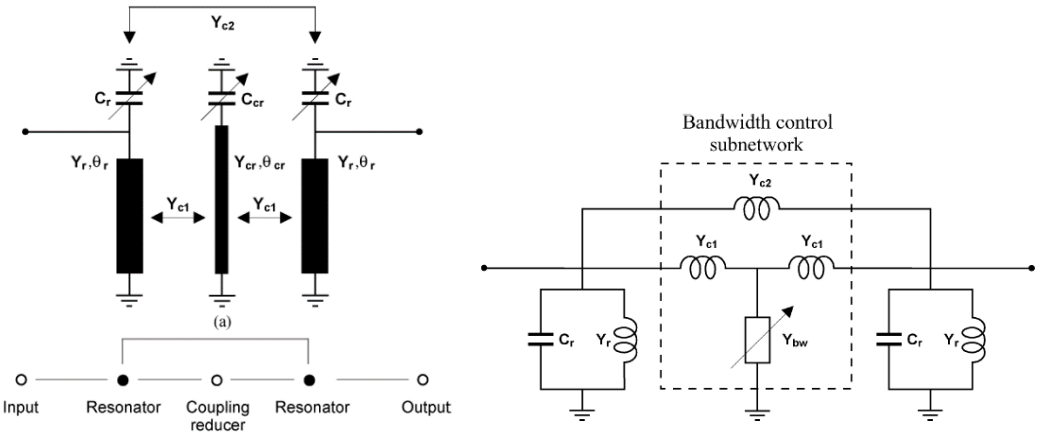

(a) (b)

Figure 2.27 (a) Coupled resonator pair with variable coupling reducer; (b) Corresponding equivalent circuit.

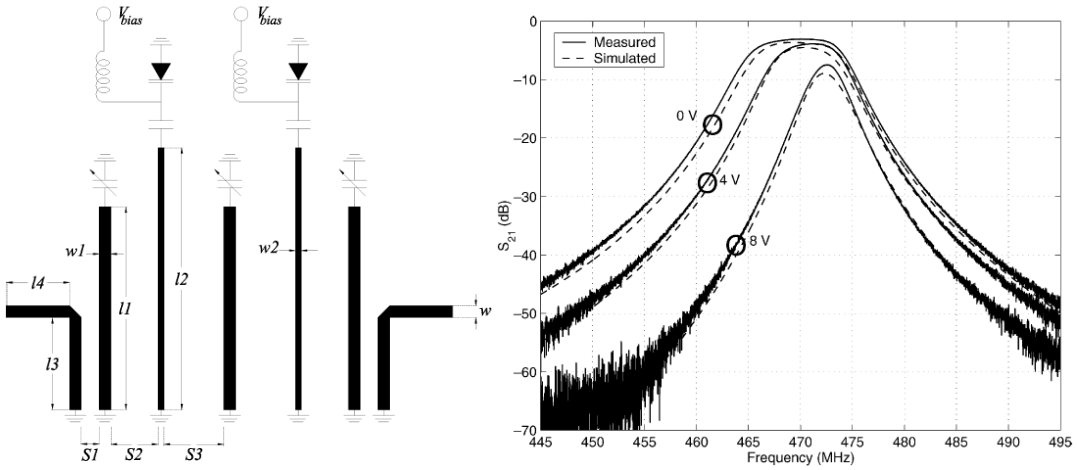

(a) (b)

Figure 2.28 (a) Layout of the filter; (b) Frequency responses of the bandwidth tuning.

2.3.2.3 Fully Reconfigurable Filter using Dual-behaviour Resonator

A fully reconfigurable high selective bandpass filter is demonstrated in [35] with the variable dual-behaviour resonator. As shown in Figure 2.29 (a), a 3-pole bandpass filter consists of two half-wavelength resonators and one dual-behaviour resonator, where the dual-behaviour resonator produces not only one transmission pole in the passband

but also two transmission zeros in each side of the stopband. Quarter-wavelength transmission lines are connected between resonators as impedance inverters. Mechanically adjustable capacitors are loading at ends of each resonators to adjust the resonating frequency. The bandwidth tuning for a constant centre-frequency is attained by only modifying the capacitors C_{c1} and C_{c2}. In the meantime, the two transmission zeros are moving with the passband keeping the passband selectivity. The frequency responses of the bandwidth tuning are shown in Figure 2.29 (b). Observed 3-dB bandwidth can be tuned from 279 MHz to 42 MHz while the measured minimum in-band insertion loss is raising from 0.5 dB to 2.1 dB.

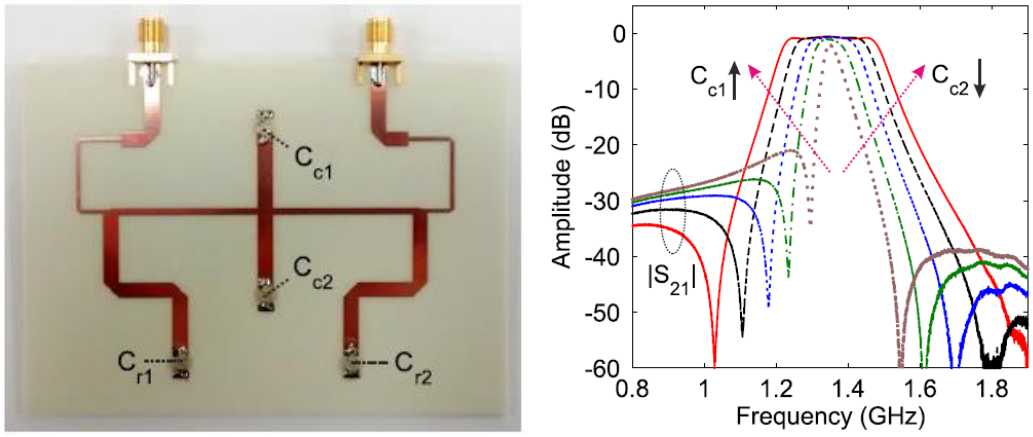

(a) (b)

Figure 2.29 (a) Manufactured fully-reconfigurable microstrip filter; (b) Bandwidth tuning [35].

2.3.3 Summary

In the above-reviewed works, filter frequency tuning techniques using switches and varicaps are demonstrated with properties of constant absolute bandwidth, reconfigurable transmission zeros, and high selectivity. Meanwhile, the bandwidth reconfigurations are mainly achieved by controlling coupling coefficients between resonators. We can find that due to the low-Q of varactors, all the varactor-tuned bandpass filters suffer from the high loss and the serious insertion loss variation. Acceptable filter performances are performed in [25], [35] using switch band or mechanical tuning elements, but the costs are high power consumption, large filter size or low tuning speed. To maintain the compact size and high tuning speed of the tunable filter, improvement methods for low-Q filters are desired.

2.4 Performance-Enhancement for High Loss Filters

The trade-off is usually made between the size and the quality factor (Q-factor) in the filter design. The low Q-factor of the resonator can cause high insertion loss and high loss variation in the passband while the high-quality factor often requires bulky size for the resonator such as cavity resonator. For a modern communication system, shrinking footage of filter becomes much important which restricts the quality factor of the resonator. Assuming an N^{th} -order Chebyshev bandpass network with uniform resonator Q_u and a cut-off frequency of 1, the insertion loss caused by the resonator dissipative loss at the centre frequency f_0 can be estimated by [7]

$$IL \approx 8.686\left|N-1.5\right|\frac{f_0}{BW\cdot Q_u} \tag{2.28}$$

Physically, the insertion loss in the filter can be also explained in the way of group delay. The more signals remain in the filter, the more energy dissipation is. The increase in the insertion loss can be found by

$$IL \approx 8.686\left(\frac{\tau_g(\omega)}{Q_u}\right) \tag{2.29}$$

where the $\tau_g(\omega)$ is the group delay of the filter in lossless condition at frequency ω. The insertion loss is higher where the group delay is large. Thus, the insertion loss at passband edges is usually larger than at the middle leading to large in-band insertion loss variation (also called round edge effect). As the group delay is inversely proportional to the fractional bandwidth, the round edge effect is much pronounced in narrowband filters.

An example to explain the effect of the limited resonator-Q here is the frequency responses of a 4-pole inline filter shown in Figure 2.30. The filter has a designed bandwidth of 50MHz at 1 GHz. Lossless resonators and low-Q resonators (high loss) are taken into simulations separately. In the lossless case, a 4-pole Chebyshev response has an equal in-band ripple of -0.0359 dB, and the same insertion loss can be observed at the edge of the passband. Thus, one can define the in-band insertion-loss variation or passband-flatness of this filter as 0.0359 dB. In the same graph, the blue-lines show the

S-parameters of this filter with a resonator-Q of 150. Compared to the lossless responses, additional insertion loss can be observed in the passband with a round band-edge rolloff. The passband edge (at 0.975 GHz defined by the lossless Chebyshev responses) is 1.347 dB below the passband centre. Therefore, the in-band insertion-loss variation of such a low resonator-Q filter is 1.347 dB. Alternatively, if we still consider the 0.0359 dB cutoff passband, the bandwidth of this high-loss filter shrinks to 15.7 MHz which is only 31% of the theoretical value. When such a filter precedes a nonlinearity in an RF chain, this insertion-loss variation can lead to severe degradation in communication system performance.

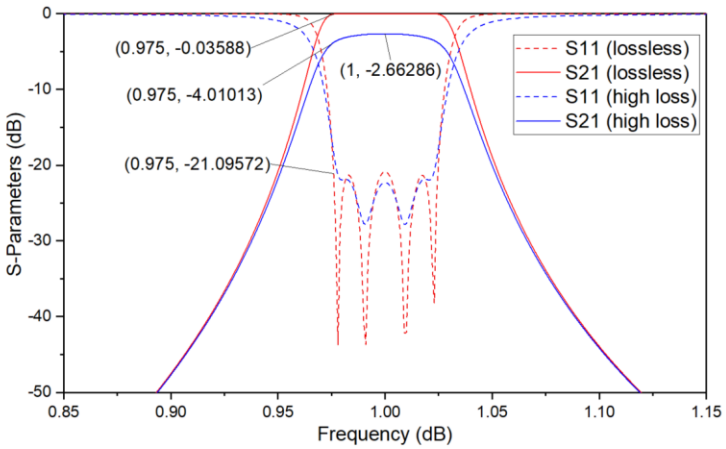

Figure 2.30 Responses of a 4-pole inline filter when the filter is lossless or high-loss.

To improve the passband-flatness performance of low-Q resonator filters, active components can be taken into the filter design to compensate the loss in filters [37]–[40]. Alternatively, lossy techniques are proposed to improve the passband flatness at the expense of insertion loss and return loss [41], [42].

2.4.1 Active Filter

Traditional tunable planar filters have been struggling from the high loss as the statement above. The active circuit with RF transistors has been proposed to overcome the high insertion loss of the filter. For example, negative resistance (NR) circuit which is commonly used in RF oscillator application has been applied to filter designs to achieve high-quality factor of the resonator.

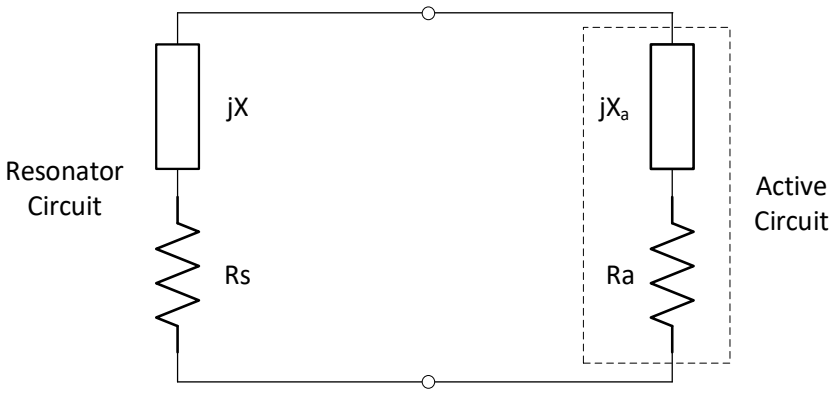

Figure 2.31 Generic circuit of a passive resonator with negative resistance compensation.

Figure 2.31 illustrates a generic circuit of the resistance cancellation for a passive resonator, where the external resonator having an impedance of $Z_r = R_s + jX$ is terminated with an active circuit with an impedance of $Z_a = R_a + jX_a$. For ideal loss compensation, we have the active circuit criterion:

$$R_a = -R_s \tag{2.30}$$

where the R_a is negative because of the passive loss $R_s > 0$, so as called negative resistance circuit. Note that, when the active circuit presents in a resonating tank, the effect of the imaginary part of the active circuit impedance jX_a is also an essential parameter for the prediction of characteristics of the resonator. Using this concept, high Q-factor resonator filters are achieved in [37]–[39].

2.4.1.1 Tunable Filter with Loaded Active Capacitance Circuit

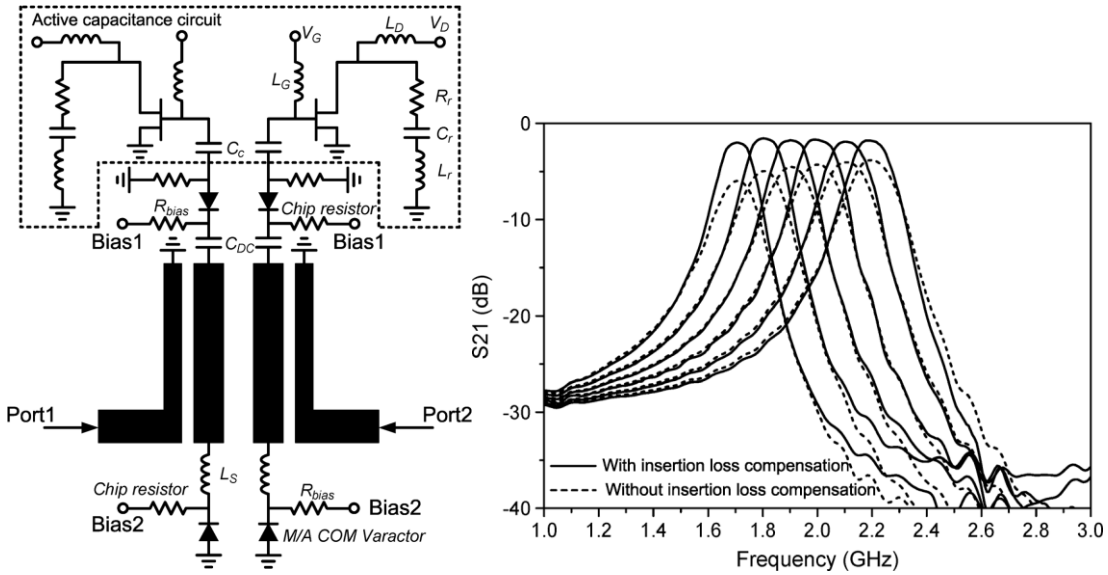

(a) (b)

Figure 2.32 Tunable filter with loaded active capacitance circuit, (a) filter layout, (b) comparison of the tunable filter with and without insertion loss compensation [39].

Figure 2.32 demonstrates a varactor-tuned combline filter loaded by the active capacitance circuits. The constant absolute bandwidth during the centre frequency tuning is achieved by using lumped series resonators which consist of series inductors and variable capacitors in place of the short-circuit end of combline. Meantime, the active circuit is loaded at the other end of resonator providing the negative resistance over the entire centre frequency tuning range. In such a manner, the compensation for filter insertion loss over the tuning range of 1.7 – 2.2 GHz is attained in Figure 2.32 (b). Since the active components are involved in the filtering circuit, the power-handling capability of the circuit is concerned. Figure 2.33 shows the filter responses with different input power. The filter can handle an input power of 5-8 dBm before a considerable distortion.

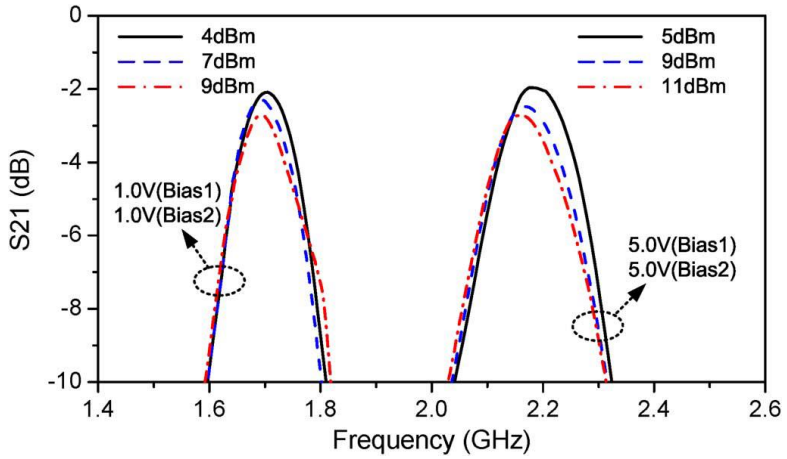

Figure 2.33 Measured filter responses with different input power.

2.4.1.2 Tunable Filter with Coupled Negative Resistance Circuit

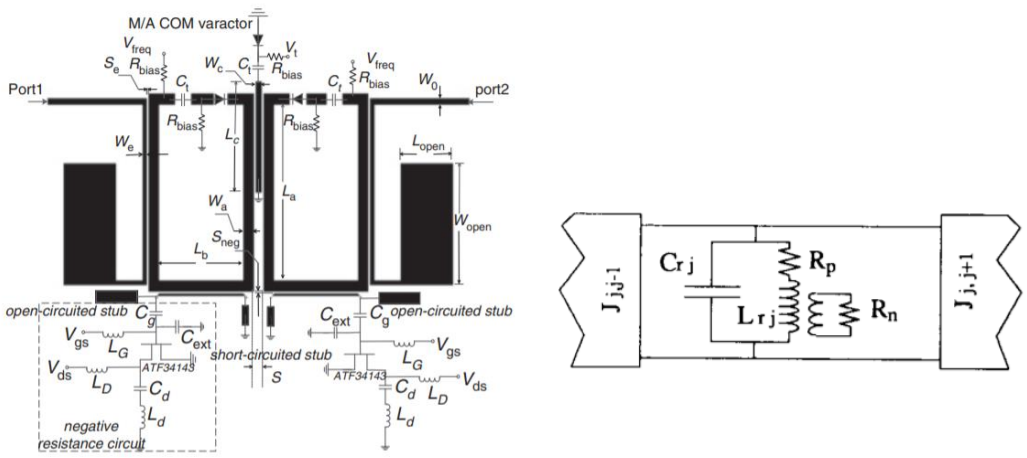

(a) (b)

Figure 2.34 (a) Layout of the tunable BPF with coupled NR circuit; (b) Equivalent circuit. [37], [38]

A similar negative resistive circuit was used in [38] with a different interfere method in tunable filter design. As shown in Figure 2.34 (a), the active circuit is not connected to the resonator but to a short-circuited stub. The equivalent circuit of the active resonator is given in Figure 2.34 (b). The negative resistance generated by the active circuit is fed into the filter circuit by the inductive coupling between stub and resonator. Such a configuration makes the characteristics of the resonator easy to predict, whereas the controlling for the NR effect is difficult. As a result, filter frequency responses are given in Figure 2.35 with the NR circuit turned on and off. The insertion loss compensated

below 0.88 dB is achieved for the frequency tuning from 0.8 GHz to 1GHz.

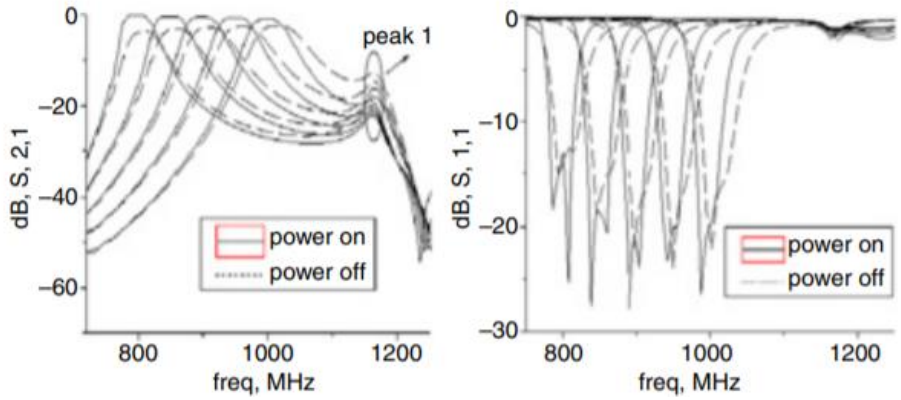

Figure 2.35 Frequency responses of the tuned filter with the NR circuit turned on/off [37].

2.4.2 Lossy Filter Techniques

Despite the fact that a high Q-factor resonator filter can be achieved by using active circuits to provide flat and low-loss transmission, [43] has pointed out the problem of intermodulation in the active filter technique. In the receiver path of a satellite transponder, the preselect-filter and low-noise-amplifier (LNA) cascade structure shown in Figure 2.36 (a) is a conventional configuration. The filter in such an architecture needs to be low-loss and high selective as the insertion loss of this filter can result in negative effect on the overall noise figure of the receiver. Although higher Q resonators such as cavity or coaxial resonators could be used in the preselect-filter to minimize the insertion loss and sharp the band edge rolloff, mass and volume are also very critical considerations from the practical design perspective. As suggested in [44], the architecture shown in Figure 2.36 (b) can give equivalent intermodulation and noise figure. In this case, the receiver amplifier is split into two blocks with a filter in between them. The first amplifier provides just enough gain for a reasonable noise figure without introducing too many intermodulation products. The filter after the first amplifier now can have a high-level passband insertion loss, but high selectivity is required to protect the second amplifier from interfering signals.

Assuming out-of-band interferes with power P_{int} create in-band third-order intermodulation products. All amplifiers are assumed to have the same output third-order intercept point I. The power level of in-band intermodulation products at the

output of the conventional architecture is:

$$P_{IM} = 3((P_{INT} - L_0) + G) - 2I \tag{2.31}$$

where the L_0 is the stopband insertion loss, and the G is the gain of the amplifier. The filter is considered as a lossless network. At the output of the second architecture, the intermodulation products power level P_{IM1} caused by the first amplifier and the power level P_{IM2} caused by the second amplifier are

$$P_{IM1} = 3(P_{INT} + G_1) - 2I - L_1 + G_2 \tag{2.32}$$

$$P_{IM2} = 3((P_{INT} + G_1 - L_2) + G_2) - 2I \tag{2.33}$$

where G_1 is the gain of the first amplifier, L_1 and L_2 are the in-band and out-band insertion loss of the filter, respectively, and the G_2 is the gain of the second amplifier.

When the third-order products from the first amplifier is equal in value to the products from the second amplifier, $P_{IM1} = P_{IM2}$, a relationship between the filter insertion-losses and the amplifier gain is obtained as

$$L_2 = \frac{2G_2 + L_1}{3} \tag{2.34}$$

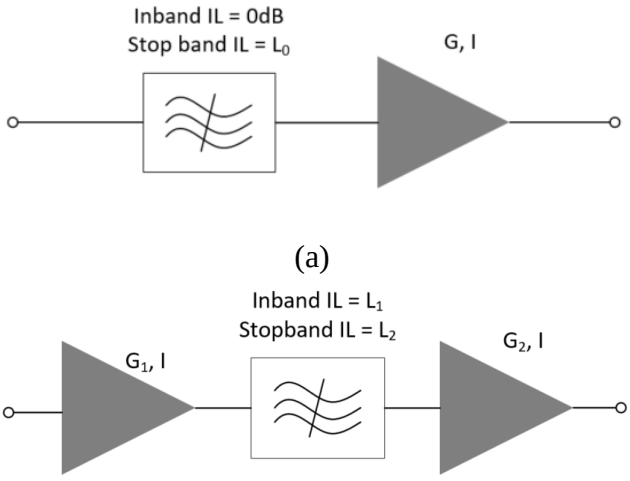

Figure 2.36 (a) Conventional filter-amplifier receiver path architecture; (b) Alternative architecture with a lossy filter. [44]

For instance, when we have components parameters of G = 40 dB, G_1 = 10 dB, G_2 = 36 dB, L_0 = 20 dB, L_1 = 6 dB, L_2 = 26 dB, and I = 20 dBm, the intermodulation power levels from both architectures in Figure 2.36 are P_{INT} + 20, but the second architecture gives an extra 6 dB tolerance for the filter in-band insertion loss. Therefore, with such an architecture, the filter in-band insertion loss is less critical. The challenge now is to design a compact filter with a good passband flatness.

Predistortion techniques were proposed to achieve high passband flatness as shown in Figure 2.37 [41]. The filter is mismatched deliberately to flatten the passband. However, the disadvantage of this type of technique is obvious that the low return loss can affect the performance of the amplifier before the filter.

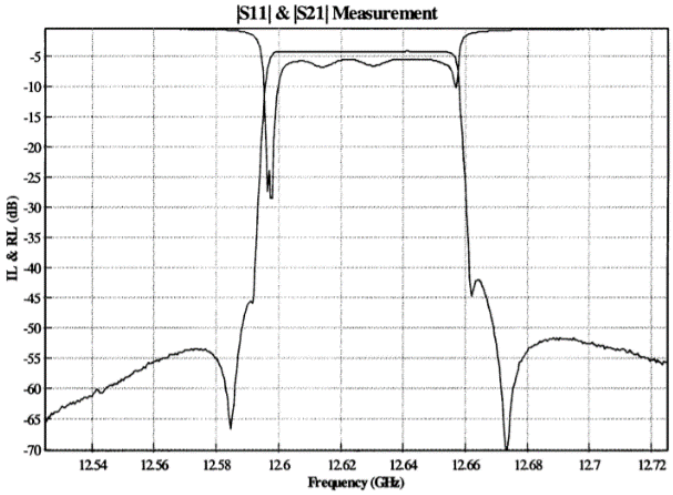

Figure 2.37 Typical predistortion frequency response [41].

Instead of predistortion, lossy filter techniques are introduced to flatten the passband without degenerating the return loss [3], [42], [45]. The concept of the lossy filter technique is achieving an improved passband flatness by playing with the distribution of the loss instead of playing with the matching. From the network perspective, the case of the lossy filter is equivalent to the configuration in Figure 2.38 (a), where two identical matched attenuators with an attenuation factor of $\sqrt{K}$ are placed at input and output ports of a lossless filter. In this case, all losses in the filter are represented by those two attenuators. The filter transmission and reflection will have a constant attenuation of K but an unchanged shape, as an example shown in Figure 2.38 (b). Compared to a normal filter, this type of filter has a higher relative loss level but a

flatness selectivity equivalent to a much higher quality factor of resonators.

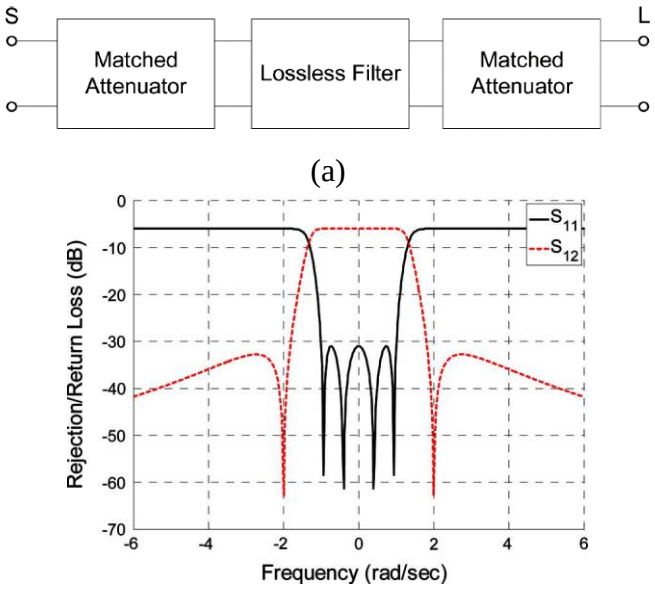

Figure 2.38 (a) Equivalent lossy filter network with same attenuation; (b) The conceptual response of a four-pole lossy filter. [45]

2.4.2.1 Non-uniform Q Distribution Method

As illustrated by equation (2.29), for a filter with uniform resonator unloaded-Q-factor Q_u, the increase in the insertion loss is proportional to the group delay, but this does not apply to those filters with non-uniform Q factors. For the parallel-connected filter network, the signal follows through multiple paths that each path is almost independently contributing the filter responses. Figure 2.39 (a) shows a 6-pole coupling diagram consisting of a dual-path transversal network, and all nodes are synchronous tuned. In the case of a transversal filter network, it is known that the path with a stronger coupling between nodes contributes more to the edges of the passband, while the middle band is more affected by the path with weak coupling. The signal path follows multiple paths, and each path contributes to the filter response almost independently. Thus, it offers a possibility to achieve the lossy responses by having the high-Q path and low-Q path configuration [3]. Figure 2.39 (b) is the response of the 6-pole transversal network. Increasing the Q of nodes 5, 6 sharpens the passband edges while the low-Q of nodes 2, 3 compress the transmission in the middle of the passband. As a result, the passband flatness is improved at the cost of higher insertion loss.

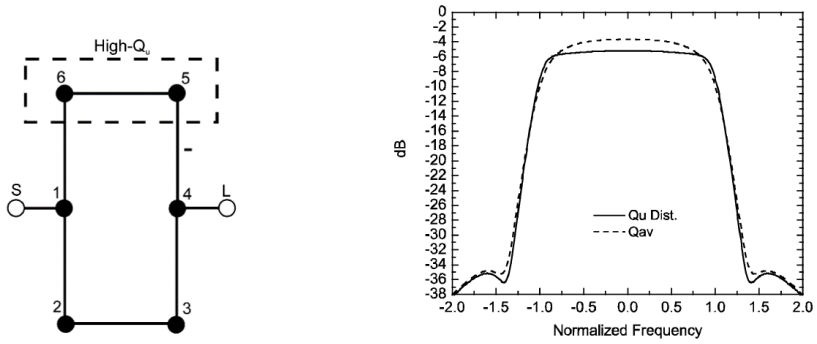

(a) (b)

Figure 2.39 Coupling diagram of a 6-pole coupling diagram with a dual-path network; (b) Responses of the 6-pole coupling diagram with multipath loss distribution compared with uniform-Q resonators.[3]

Regarding the synthesis process of the parallel-connected lossy filter, the coupling matrix is a common method that has been demonstrated in [42]. A 6-pole triple-path filter network is shown in Figure 2.40 (a), (b) with its coupling matrix, and the 3 paths are distinguished as high-Q, medium-Q, and low Q. As can be seen, the coupling matrix is almost the same as the lossless case which can be obtained by the normal coupling synthesis method in [9]. However, because of the dissipative loss in the filter, the values of diagonal elements in the matrix become a complex number with imaginary parts $j\delta_{ii}$, but the real parts of those elements remain the same. The value of δ_{ii} is given as

$$\delta_{ii} = \frac{f_0}{Q_{ui} \cdot BW} \tag{2.35}$$

where the f_0 is the centre frequency of the filter, and the BW is the bandwidth of the filter. S-parameters of this lossy coupling matrix, shown in Figure 2.40 (c), can be obtained by the synthesis method in [8]. One can see that the filter insertion loss flatness is improved with slight degenerations in the return loss. A physical configuration for this 6-pole filter is given in Figure 2.40 (d). The medium Q path is achieved by reducing the width of microstrip hairpin resonators, and engraved resistors on resonators introduce additional loss for the low-Q path.

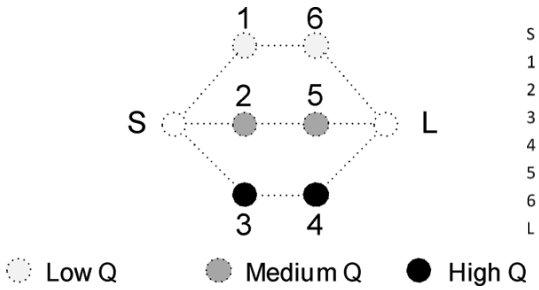

(a)

	S	1	2	3	4	5	6	L
S	0	0.653	0.645	0.462	0	0	0	0
1	0.653	j0.13	0	0	0	0	0.374	0
2	0.645	0	j0.08	0	0	-1.026	0	0
3	0.462	0	0	j0.05	1.249	0	0	0
4	0	0	0	1.249	j0.05	0	0	0.462
5	0	0	-1.026		0	j0.08	0	0.645
6	0	0.374	0	0	0	0	j0.13	0.653
L	0	0	0	0	0.462	0.645	0.653	0

(b)

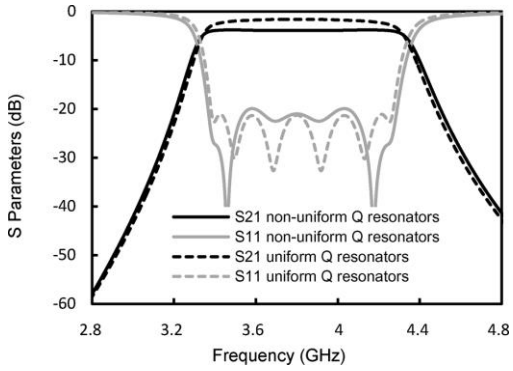

(c)

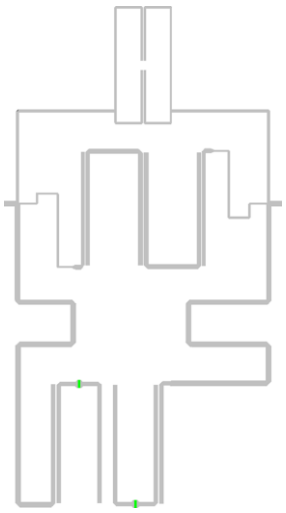

(d)

Figure 2.40 (a) Topology of a 6-pole triple-path transversal network with nonuniform Q distribution; (b) Coupling matrix; (c) Synthesised frequency responeses; (d) Physical implement. [42]

2.4.2.2 Resistive Cross-Couplings (RCCs)

The way of introducing loss into the filter through resistive cross-coupling is another popular class of lossy circuit techniques [42], [45]. The concept of resistive cross-coupling is that matrix rotations can change the physical topology of a network without affecting the electrical response. By doing so, the equivalent lossy filter network in Figure 2.41 (a) can be reconstructed by matrix rotation until no loss elements are on the diagonal of the matrix. The details of the matrix rotation to achieve the RCCs distribution are demonstrated in [3], [45]. Since the physical implementation of the lossy technique is more concerned, an example of a filter with two RCCs is given in Figure 2.41 [42]. As can be seen in the coupling diagram, resistances are introduced between nodes 2 and 4, nodes 3 and 5. Correspondingly, imaginary values are in the non-diagonal elements (m_{24}, m_{42}, m_{35} and m_{53}) of the coupling matrix which is different from the case of the non-uniform Q distribution. The physical implement on

microstrip filter is shown in Figure 2.41 (c). Lossy resistances are introduced by resistors connecting to non-resonating nodes, which are $\lambda/4$ transmission lines coupling to resonators. The passband flatness of 0.4 dB is achieved with a 3.4 dB insertion loss, shown in Figure 2.41 (d).

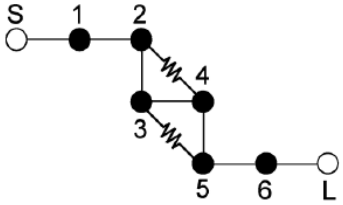

(a)

	S	1	2	3	4	5	6	L
S	0	1.304	0	0	0	0	0	0
1	1.304	j0.059	1.191	0	0	0	0	0
2	0	1.191	j0.091	0.696	j0.031	0	0	0
3	0	0	0.696	j0.091	0.679	j0.031	0	0
4	0	0	j0.031	0.679	j0.091	0.696	0	0
5	0	0	0	j0.031	0.696	j0.091	1.191	0
6	0	0	0	0	0	1.191	j0.059	1.304
L	0	0	0	0	0	0	1.304	0

(b)

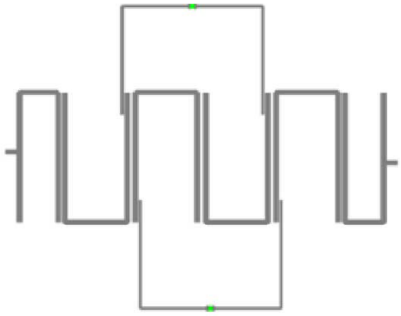

(c)

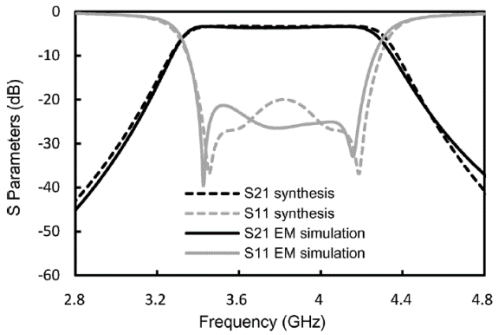

(d)

Figure 2.41 (a) Topology of a 6-pole filter with two RCCs; (b) Coupling matrix; (c) Physical implementation; (d) Frequency responses. [42]

2.4.3 Summary

Performance-enhancement methods for low-Q filters have been reviewed in this section. Active components can be introduced into the tunable filters to compensate losses in the passband, but the applicable frequency range of such active filter is limited by the working frequency range of the active circuits. As narrowband filters with low-Q resonators suffer from serious insertion-loss variation, lossy filter techniques are proposed to improve the filter passband flatness. However, as can be seen, there is still a lack of effort on the implementation of the tunable lossy filter.

2.5 Reference

[1] J. s Hong, 'Reconfigurable Planar Filters', *IEEE Microwave Magazine*, vol. 10, no. 6, pp. 73–83, Oct. 2009.

[2] R. R. Mansour, F. Huang, S. Fouladi, W. D. Yan, and M. Nasr, 'High-Q Tunable Filters: Challenges and Potential', *IEEE Microwave Magazine*, vol. 15, no. 5, pp. 70–82, Jul. 2014.

[3] A. C. Guyette, I. C. Hunter, and R. D. Pollard, 'The Design of Microwave Bandpass Filters Using Resonators with Nonuniform Q', *IEEE Transactions on Microwave Theory and Techniques*, vol. 54, no. 11, pp. 3914–3922, Nov. 2006.

[4] R. M. Livingston, 'Predistorted Waveguide Filters for Use in Communications Systems', in *1969 G-MTT International Microwave Symposium*, May 1969.

[5] Young-Hoon Chun, Jae-Ryong Lee, Sang-Won Yun, and Jin-Koo Rhee, 'Design of an RF Low-noise Bandpass Filter using Active Capacitance Circuit', *IEEE Transactions on Microwave Theory and Techniques*, vol. 53, no. 2, pp. 687–695, Feb. 2005.

[6] D. M. Pozar, *Microwave Engineering*, 4th Revised edition edition. Hoboken, NJ: John Wiley & Sons, 2011.

[7] G. Matthaei, E. M. T. Jones, and L. Young, *Microwave Filters, Impedance-Matching Networks, and Coupling Structures*. Norwood, Mass: Artech House, 1980.

[8] J.-S. Hong, *Microstrip Filters for RF / Microwave Applications*, 2nd Edition edition. Hoboken, N.J: Wiley-Blackwell, 2011.

[9] R. J. Cameron, C. M. Kudsia, and R. Mansour, *Microwave Filters for Communication Systems: Fundamentals, Design and Applications*, 2 edition. Hoboken, NJ, USA: Wiley-Blackwell, 2018.

[10] Jia-Sheng Hong and M. J. Lancaster, 'Design of Highly Selective Microstrip Bandpass Filters with a Single Pair of Attenuation Poles at Finite Frequencies', *IEEE Transactions on Microwave Theory and Techniques*, vol. 48, no. 7, pp. 1098–1107, Jul. 2000.

[11] B. Yassini, M. Yu, D. Smith, and S. Kellett, 'A Ku-Band High-Q Tunable Filter With Stable Tuning Response', *IEEE Transactions on Microwave Theory and Techniques*, vol. 57, no. 12, pp. 2948–2957, Dec. 2009.

[12] B. Yassini, M. Yu, and B. Keats, 'A Ka-Band Fully Tunable Cavity Filter', *IEEE Transactions on Microwave Theory and Techniques*, vol. 60, no. 12, pp. 4002–4012, Dec. 2012.

[13] Tae-Yeoul Yun and Kai Chang, 'Piezoelectric-transducer-controlled Tunable Microwave Circuits', *IEEE Trans. Microwave Theory Techn.*, vol. 50, no. 5, pp. 1303–1310, May 2002.

[14] F. Huang and R. R. Mansour, "Tunable Compact Dielectric Resonator Filters," *2009 European Microwave Conference (EuMC)*, Rome, Italy, 2009, pp. 559-562.

[15] M. A. El-Tanani and G. M. Rebeiz, 'High-Performance 1.5-2.5 GHz RF-MEMS Tunable Filters for Wireless Applications', *IEEE Transactions on Microwave Theory and Techniques*, vol. 58, no. 6, pp. 1629–1637, Jun. 2010.

[16] G. Rebeiz *et al.*, 'Tuning in to RF MEMS', *IEEE Microwave*, vol. 10, no. 6, pp. 55–72, Oct. 2009.

[17] Young-Hoon Chun, Jia-Sheng Hong, Peng Bao, T. J. Jackson, and M. J. Lancaster, 'Tunable Bandstop Filters using BST Varactor Chips', in *2007 European Microwave Conference*, Oct. 2007, pp. 110–113.

[18] J. Nath *et al.*, 'An Electronically Tunable Microstrip Bandpass Filter using Thin-film Barium-Strontium-Titanate (BST) Varactors', *IEEE Transactions on Microwave Theory and Techniques*, vol. 53, no. 9, pp. 2707–2712, Sep. 2005.

[19] 'TCP-5033UB – 3.3 pF Passive Tunable Integrated Circuits (PTIC)', ON Semiconductor. Available: https://www.onsemi.com/pub/Collateral/TCP-5033UB-D.PDF.

[20] 'SMV2019-SMV2023 Series: Hyperabrupt Junction Tuning Varactors', SKYWORKS. Available: https://www.rogerscorp.com/acs/products/42/RO3003-Laminates.aspx.

[21] R. Ludwig and P. Bretchko, *RF Circuit Design: Theory and Applications*. Upper Saddle River, NJ: Prentice Hall, 2000.

[22] 'M/A-COM:MA46580 & MA46585, data sheet', M/A-COM Lowell, 2006.

[23] S. Gevorgian, 'Agile Microwave Devices', *IEEE Microwave Magazine*, vol. 10, no. 5, pp. 93–98, Aug. 2009.

[24] 'MA46H120 Series.pdf'. Accessed: Mar. 24, 2020. Available: https://cdn.macom.com/datasheets/MA46H120%20Series.pdf.

[25] F. Gentili, L. Urbani, G. Bianchi, L. Pelliccia, and R. Sorrentino, 'PIN Diode-based 4-channel Switched Filter Bank with Low-power, TTL-compatible Driver', in *2014 IEEE MTT-S International Microwave Symposium (IMS2014)*, Jun. 2014, pp. 1–4.

[26] B.-W. Kim and S.-W. Yun, 'Varactor-tuned Combline Bandpass Filter using Step-Impedance Microstrip Lines', *IEEE Transactions on Microwave Theory and Techniques*, vol. 52, no. 4, pp. 1279–1283, Apr. 2004.

[27] X. G. Wang, Y. H. Cho, and S. W. Yun, 'A Tunable Combline Bandpass Filter Loaded With Series Resonator', *IEEE Transactions on Microwave Theory and Techniques*, vol. 60, no. 6, pp. 1569–1576, Jun. 2012.

[28] M. A. El-Tanani and G. M. Rebeiz, 'A Two-Pole Two-Zero Tunable Filter With Improved Linearity', *IEEE Transactions on Microwave Theory and Techniques*,

vol. 57, no. 4, pp. 830–839, Apr. 2009.

[29] W. Tang and J. S. Hong, 'Varactor-Tuned Dual-Mode Bandpass Filters', *IEEE Transactions on Microwave Theory and Techniques*, vol. 58, no. 8, pp. 2213–2219, Aug. 2010.

[30] R. Berezdivin, R. Breinig, and R. Topp, 'Next-generation Wireless Communications Concepts and Technologies', *IEEE Communications Magazine*, vol. 40, no. 3, pp. 108–116, Mar. 2002.

[31] W. M. Fathelbab and M. B. Steer, 'A Reconfigurable Bandpass Filter for RF/microwave Multifunctional Systems', *IEEE Transactions on Microwave Theory and Techniques*, vol. 53, no. 3, pp. 1111–1116, Mar. 2005.

[32] Y. C. Chiou and G. M. Rebeiz, 'Tunable 1.55 – 2.1 GHz 4-Pole Elliptic Bandpass Filter With Bandwidth Control and $> 50 hbox dB$ Rejection for Wireless Systems', *IEEE Transactions on Microwave Theory and Techniques*, vol. 61, no. 1, pp. 117–124, Jan. 2013.

[33] T. Yang and G. M. Rebeiz, 'Tunable 1.25-2.1-GHz 4-Pole Bandpass Filter With Intrinsic Transmission Zero Tuning', *IEEE Transactions on Microwave Theory and Techniques*, vol. 63, no. 5, pp. 1569–1578, May 2015.

[34] M. Sanchez-Renedo, R. Gomez-Garcia, J. I. Alonso, and C. Briso-Rodriguez, 'Tunable Combline Filter with Continuous Control of Centre Frequency and Bandwidth', *IEEE Transactions on Microwave Theory and Techniques*, vol. 53, no. 1, pp. 191–199, Jan. 2005.

[35] R. Gómez-García, J. M. Muñoz-Ferreras, and D. Psychogiou, 'Fully-Reconfigurable Bandpass Filter with Static Couplings and Intrinsic-switching Capabilities', in *2017 IEEE MTT-S International Microwave Symposium (IMS)*, Jun. 2017, pp. 914–917.

[36] A. Miller and J. Hong, 'Cascaded Coupled Line Filter With Reconfigurable Bandwidths Using LCP Multilayer Circuit Technology', *IEEE Transactions on Microwave Theory and Techniques*, vol. 60, no. 6, pp. 1577–1586, Jun. 2012.

[37] C.- Chang and T. Itoh, 'Microwave Active Filters Based on Coupled Negative Resistance Method', *IEEE Transactions on Microwave Theory and Techniques*, vol. 38, no. 12, pp. 1879–1884, Dec. 1990.

[38] J. Chen, X. Zhu, C. Ge, and L. Cao, 'Tunable Bandpass Filter with Low-loss and Enhanced Selectivity Based on Controllable Coupled Negative Resistance', *Electronics Letters*, vol. 49, no. 24, pp. 1544–1545, Nov. 2013.

[39] X. Wang, Y. Cho, and S. Yun, 'A Tunable Combline Bandpass Filter Loaded With Series Resonator', *IEEE Transactions on Microwave Theory and Techniques*, vol. 60, no. 6, pp. 1569–1576, Jun. 2012.

[40] Y. Gao, J. Powell, X. Shang, and M. J. Lancaster, 'Coupling Matrix-Based Design of Waveguide Filter Amplifiers', *IEEE Transactions on Microwave Theory and*

Techniques, vol. 66, no. 12, pp. 5300–5309, Dec. 2018.

[41] M. Yu, W.-C. Tang, A. Malarky, V. Dokas, R. Cameron, and Y. Wang, 'Predistortion Technique for Cross-coupled Filters and Its Application to Satellite Communication Systems', *IEEE Transactions on Microwave Theory and Techniques*, vol. 51, no. 12, pp. 2505–2515, Dec. 2003.

[42] A. Basti, A. Périgaud, S. Bila, S. Verdeyme, L. Estagerie, and H. Leblond, 'Design of Microstrip Lossy Filters for Receivers in Satellite Transponders', *IEEE Transactions on Microwave Theory and Techniques*, vol. 62, no. 9, pp. 2014–2024, Sep. 2014.

[43] I. C. Hunter and S. R. Chandler, 'Intermodulation Distortion in Active Microwave Filters', *Antennas and Propagation IEE Proceedings – Microwaves*, vol. 145, no. 1, pp. 7–12, Feb. 1998.

[44] I. Hunter, A. Guyette, and R. D. Pollard, 'Passive Microwave Receive Filter Networks using Low-Q Resonators', *IEEE Microwave Magazine*, vol. 6, no. 3, pp. 46–53, Sep. 2005.

[45] V. Miraftab and M. Yu, 'Generalized Lossy Microwave Filter Coupling Matrix Synthesis and Design Using Mixed Technologies', *IEEE Transactions on Microwave Theory and Techniques*, vol. 56, no. 12, pp. 3016–3027, Dec. 2008.

CHAPTER 3
TUNABLE DUAL-MODE LOSSY FILTER

3.1 Introduction

Dual-mode filters are attractive because of its doubly tuned resonant circuit [1], resulting in a compact filter configuration. The tunable dual-mode filter has been demonstrated in [2], [3] where varactors loaded dual-mode resonators are employed for frequency tuning. One can observe that those tunable filters have serious in-band losses and high insertion-loss variation. Furthermore, [4] reports a dual-mode filter with non-uniform Q lossy techniques by utilising the dual-path topology of the dual-mode resonator. A flat passband can be achieved by simply loading resistor on the resonator to reduce the Q of odd mode. In this Chapter, the non-uniform Q distribution lossy method is introduced into a type of dual-mode filter with a cascaded configuration. Bandwidth and frequency tunability are applied to the lossy filter using varactor diodes.

3.2 Dual-Mode Open-Loop Resonator Based Microstrip Filter

3.2.1 2-pole Dual-Mode Bandpass Filter

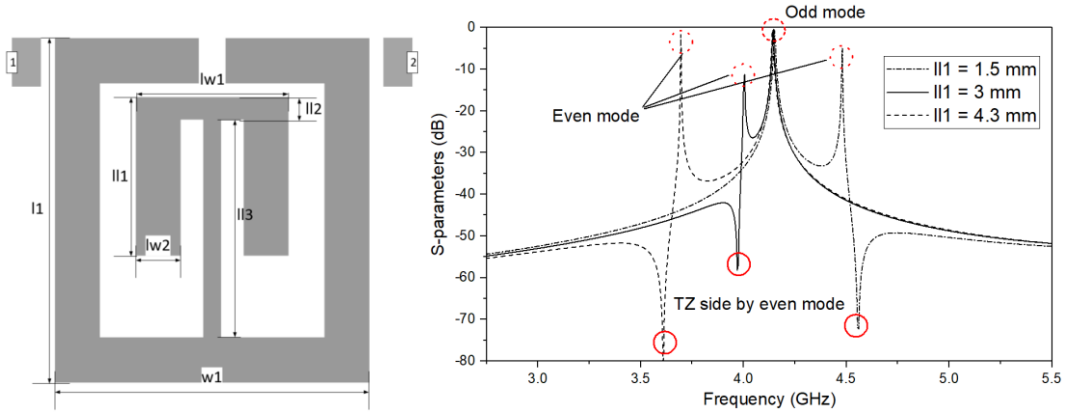

(a) (b)

Figure 3.1 (a) A typical dual-mode microstrip open-loop resonator under weak excitation; (b) Frequency response of the weak excited resonator.

A typical dual-mode microstrip open-loop resonator is given in Figure 3.1 (a) [1]. The

resonator is based on a substrate RO3003 with a dielectric constant of 3 and a thickness of 1.02 mm. A loading element or perturbation is attached at the middle point of an open-loop resonator so that an additional resonance is introduced. Using weak excitation in a commercial full-wave EM simulator, the resonating characteristic of the dual-mode open-loop resonator can be observed. Figure 3.1 (b) shows the simulated frequency responses of the dual-mode resonator when the length of the loading element $l1$ varies. The even mode frequency is located at a higher frequency of 4.55 GHz when $l1 = 1.5\ mm$. After increasing the length $l1$, the even mode peak is moving toward a lower frequency, for example, 3.6 GHz for $l1 = 4.3\ mm$. The frequency of the odd mode peak does not move for any change of the loading element. Thus, the even mode and the odd mode are decoupled. Additionally, an intrinsic transmission zero can be found in the stopband on the side of even mode frequency which is caused by the property of dual mode resonator.

For our investigation, symmetrical-plane analysis can be applied for the even and odd modes characterising as shown in Figure 3.2 (a). A symmetrical plane can be placed on the middle plane of the resonator. When a magnetic plane presents on the symmetrical plane, no current can follow on the plane. The corresponding equivalent layout for the even mode can be found in Figure 3.2 (b) where the left/right half resonator is equivalently opened. On the other hand, when an electric plane presents on the midplane, the left/right half resonator is equally connecting to the ground acting like a quarter wavelength resonator. The loading element now does not affect the resonating frequency. Note that, the odd mode is the original mode of an open-loop resonator without a loading element.

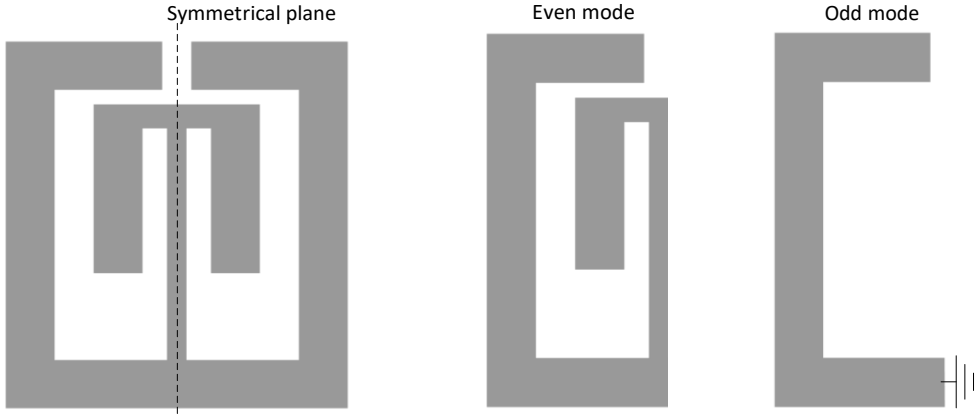

(a) (b) (c)

Figure 3.2 (a) Symmetrical plane on a dual open-loop resonator; (b) Even mode equivalent layout; (c) Odd mode equivalent layout.

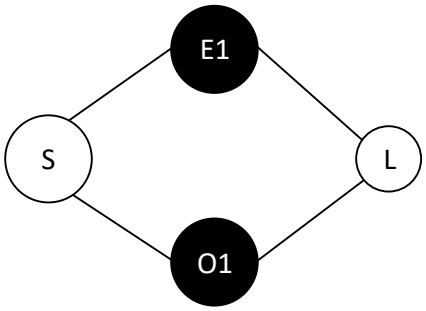

$$\begin{bmatrix} m_{SS} & m_{Se} & m_{So} & m_{SL} \\ m_{eS} & m_{ee} & m_{eo} & m_{eL} \\ m_{oS} & m_{oe} & m_{oo} & m_{oL} \\ m_{LS} & m_{Le} & m_{Lo} & m_{LL} \end{bmatrix}$$

(a) (b)

Figure 3.3 (a) Dual-path topology; (b) Coupling matrix, the subscript "e" is the even node, "o" is the odd node, and the "S" and "L" are the source and the load, respectively.

Therefore, the dual-mode open-loop microstrip resonator can be described as a paralleled dual-path configuration in Figure 3.3 (a), where node E1 is the even mode, node O1 is the odd mode, S and L are termination nodes. The coupling matrix for this 2-pole configuration is given in Figure 3.3 (b), where the coupling between source to even node is expressed by m_{Se}, etc.

The relationship between filter parameters (even/odd mode frequencies and the external quality factors Q_e, Q_o) and the coupling matrix elements can be found as [2]

$$\begin{aligned} f_e &= f_0\left(1-\frac{m_{ee}\cdot FBW}{2}\right) \\ f_o &= f_0\left(1-\frac{m_{oo}\cdot FBW}{2}\right) \end{aligned} \tag{3.1}$$

$$Q_{o/e} = \frac{1}{m_{so/se}^2 \cdot FBW} \tag{3.2}$$

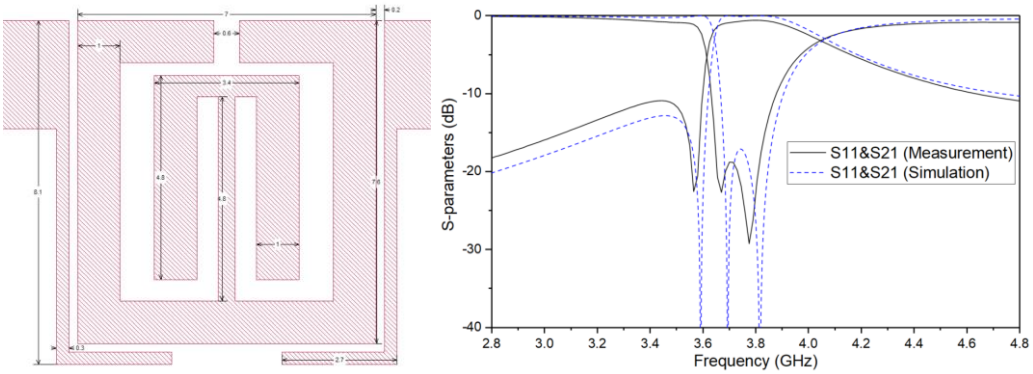

(a) (b)

Figure 3.4 (a) Layout of a two-port dual-mode microstrip filter on a substrate with a dielectric constant of 3 and a thickness of 1.02 *mm*; (b) Simulation and measurement frequency responses of the filter.

An example of the filter matrix extraction is described next. The 2-pole dual-mode filter in Figure 3.4 (a) is resonating at f_0 = 3.75 GHz with a bandwidth of $FBW = 0.044$. A lower-side transmission-zero enhances the selectivity of the left side of the passband. The parameter extraction method in Chapter 2.1.3 is used here for matrix elements calculation. As shown in Figure 3.5 (a), (b), with weak even/odd excitations, the resonating frequency f_e, f_o of each mode can be observed at the peaks of the group delay responses of the S_{11e} and S_{11o}, where the S_{11e} and S_{11o} are S-parameters under even mode excitation and odd mode excitation, respectively. In the meantime, the extracted external-Q can be calculated by extracting the group delay responses with the feeding structure. Therefore, the matrix elements m_{ee}, m_{oo}, m_{so}, and m_{ee} can be obtained using equations (3.1) – (3.2).

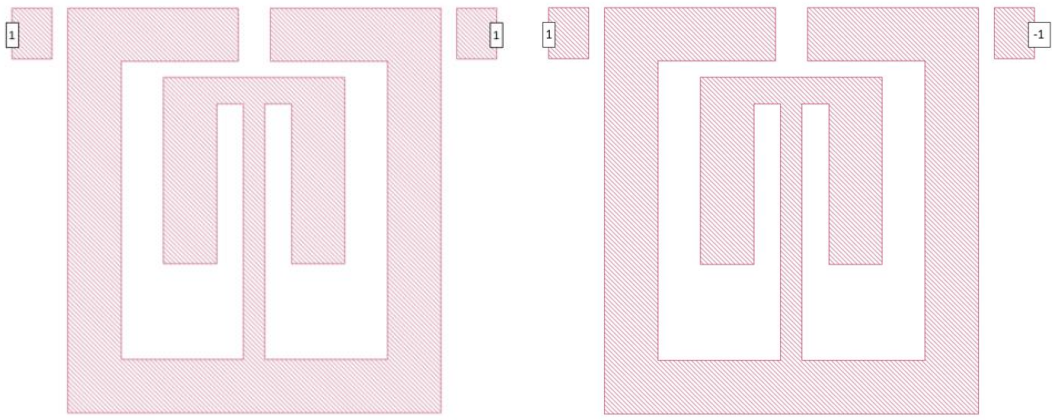

(a) (b)

Figure 3.5 Group delay extracting configuration, (a) even mode excitation; (b) Odd mode excitation.

Since the even mode and the odd mode are decoupled, matrix elements m_{12} and m_{12}, which represent the coupling between even and odd, are equal to 0. Therefore, the $n+2$ coupling matrix of the filter in Figure 3.4 is

$$\begin{bmatrix} 0 & 0.4376 & 0.9806 & 0 \\ 0.4376 & 0.666 & 0 & -0.4376 \\ 0.9806 & 0 & -1.309 & 0.9806 \\ 0 & -0.4376 & 0.9806 & 0 \end{bmatrix} \tag{3.3}$$

where $m_{S1} = -m_{1L}$ are for the even mode and $m_{S2} = m_{2L}$ are for the odd mode. Using equation (2.17) – (2.19), Figure 3.6 shows the S-parameters plots in which a similar frequency response to the Figure 3.4 (b) is observed.

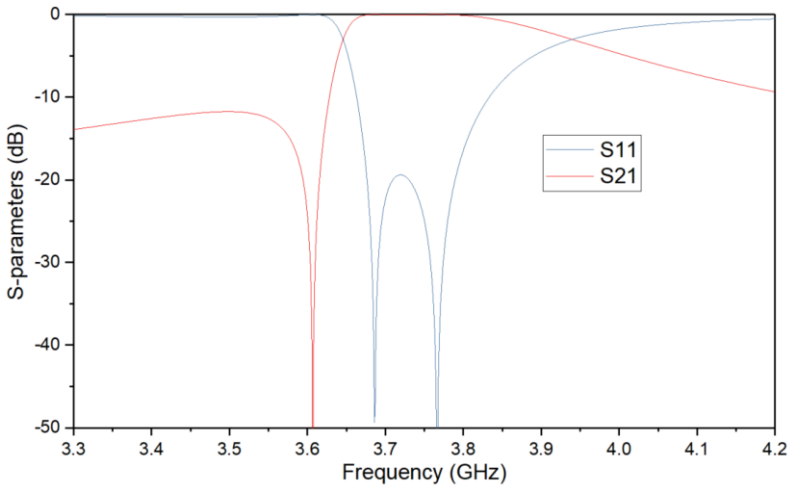

Figure 3.6 Theoretical filter response.

3.2.2 High Selective 4-pole Dual-Mode Filter

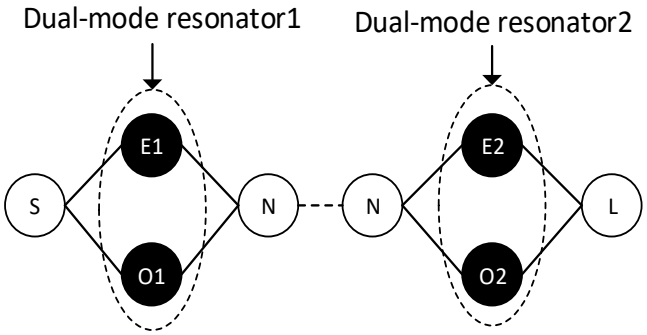

Figure 3.7 Cascaded coupling topology of a 4-pole dual-mode filter.

The filter in the previous section can achieve asymmetric frequency selectivity as a finite-frequency transmission zero on one side of the passband. As a matter of fact, a four-pole filter can be designed based on the dual-mode resonators to produce two transmission zeros, one on each side, improving the overall selectivity of the passband. A simple way to design a 2-order 4-pole dual-mode filter is to cascade two dual-mode resonator blocks [1]. Figure 3.7 gives the coupling topology of a 4-pole filter consisting of two cascaded dual-mode resonators connected by non-resonating nodes. For a four-pole filter which has a bandwidth of $FBW = 0.084$ at $f_0 = 2\ GHz$, a coupling matrix can be given as equation (3.4).

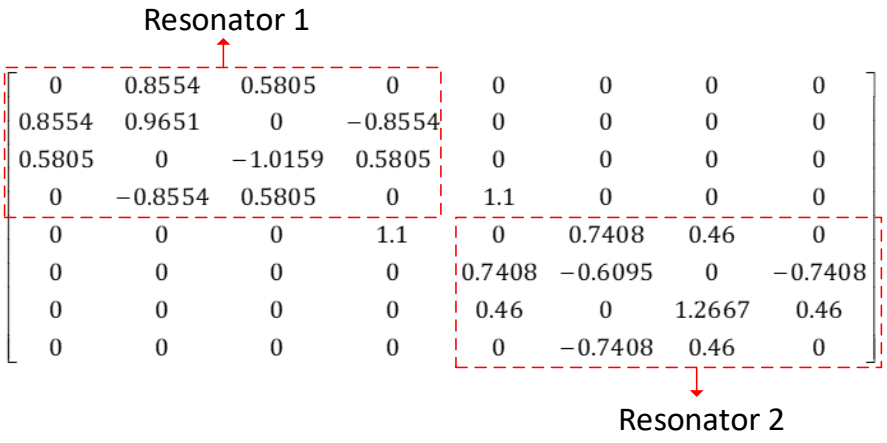

$$\begin{bmatrix} 0 & 0.8554 & 0.5805 & 0 & 0 & 0 & 0 & 0 \\ 0.8554 & 0.9651 & 0 & -0.8554 & 0 & 0 & 0 & 0 \\ 0.5805 & 0 & -1.0159 & 0.5805 & 0 & 0 & 0 & 0 \\ 0 & -0.8554 & 0.5805 & 0 & 1.1 & 0 & 0 & 0 \\ 0 & 0 & 0 & 1.1 & 0 & 0.7408 & 0.46 & 0 \\ 0 & 0 & 0 & 0 & 0.7408 & -0.6095 & 0 & -0.7408 \\ 0 & 0 & 0 & 0 & 0.46 & 0 & 1.2667 & 0.46 \\ 0 & 0 & 0 & 0 & 0 & -0.7408 & 0.46 & 0 \end{bmatrix} \tag{3.4}$$

As illustrated in the coupling matrix, two second-order-transversal-network blocks connected by non-resonating nodes can be found in the matrix that each represents the coupling matrix for one resonator. In practice, therefore, each second-order block can be designed separately, then cascaded together. The diagonal elements in the matrix for the non-resonating nodes are zero because it has no reactance, similar to the source and load nodes. Thus, the theoretical responses can be calculated by equation (2.17) – (2.19) but with a modification that

$$[\mathrm{A}] = [m] + \Omega[U'] - j[q] \tag{3.5}$$

In this case, the frequency variable matrix $\Omega[U']$ has not only $[U]_{11} = [U]_{n+2,n+2} = 0$, but also $[U]_{ii} = 0$, the subscript i is the sequence number of non-resonating nodes. In a practical implementation, the non-resonating node can be played by a short section of transmission line whose resonating frequency is away from the passband.

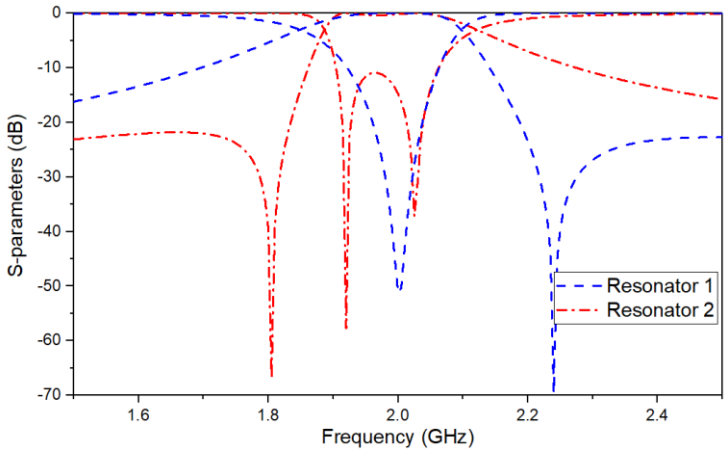

(a)

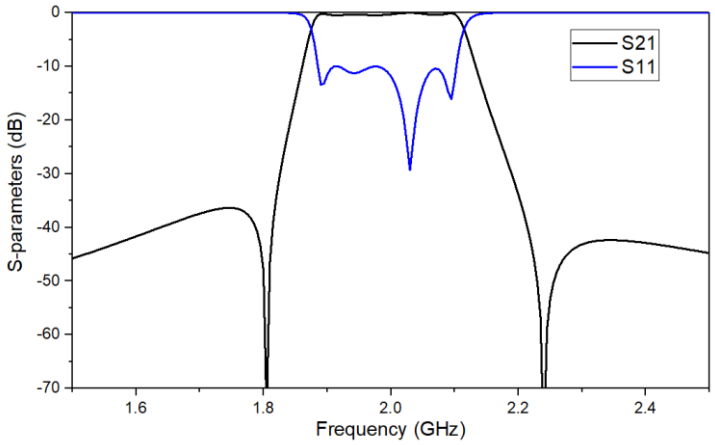

(b)

Figure 3.8 (a) Frequency responses for each resonator; (b) Theoretical responses from the given coupling matrix.

Subsequently, Figure 3.8 (a) shows the calculated frequency responses of individual 2-pole sub-filter block. Each block has 2-pole filtering responses with one transmission zero. Then, the combination results in a 4-pole high selective bandpass response, shown in Figure 3.8 (b). It is notable that the resonator 1 produces a right-side transmission zero, while a transmission zero appears in the lower-side stopband of the resonator 2. The locations of two transmission zeros have no change after the cascading.

The practical implementation of the filter is demonstrated in Figure 3.9 (a). The two dual-mode resonators are cascaded by a short section of the transmission line which controls the coupling between two resonators. Figure 3.9 (b), (c) shows the full EM simulation responses of each resonator and the cascaded 4-pole filter. As the filter is

composed of asynchronously tuned resonators, 4 poles in the passband can be individually matched to the four nodes, as indicated in the plotting. We can observe that two odd-mode poles are placed in the middle of the passband while two even-mode poles are placed on the two edges of the passband. The fabrication and measurement results of the 4-pole dual-mode filter are shown in Figure 3.10. A spurious peak can be observed at 2.85GHz which is caused by the non-resonating nodes.

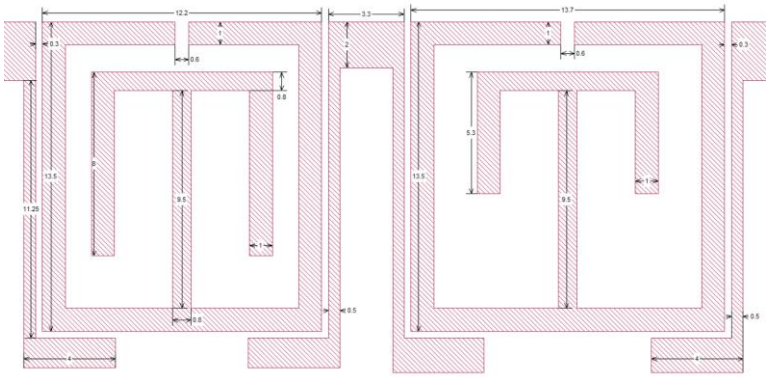

(a)

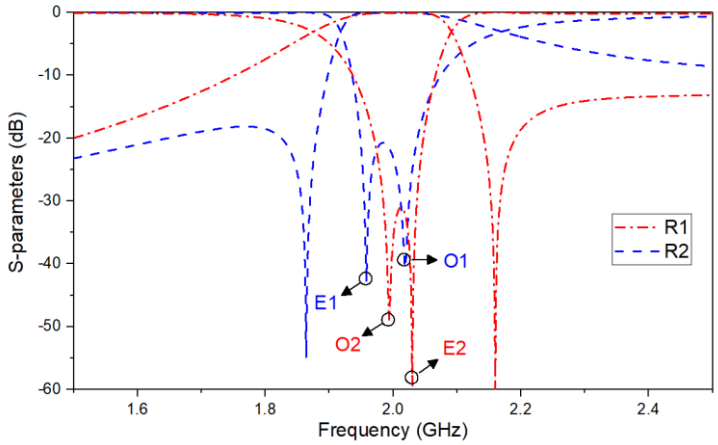

(b)

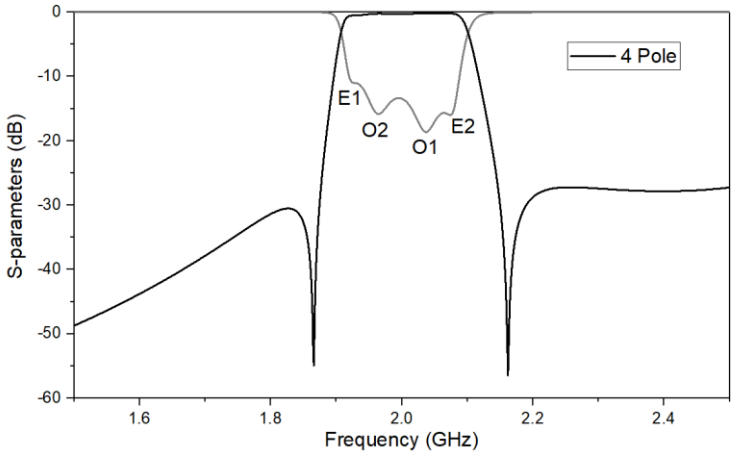

(c)

Figure 3.9 (a) Layout of a 4-pole dual-mode resonator filter on a 1.02 *mm* thick substrate with a relative dielectric constant of 3; (b) Frequency responses of each individual dual-mode resonator block; (c) Frequency responses of the 4-pole dual-mode filter.

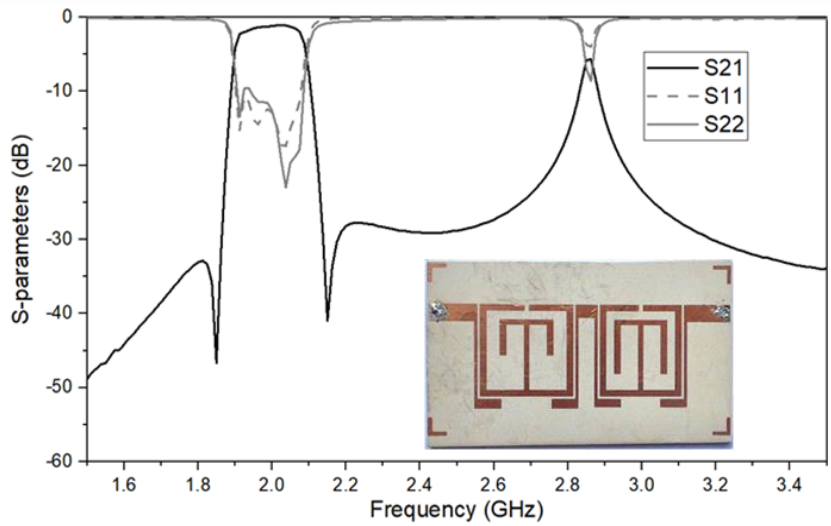

Figure 3.10 Measurement responses of the 4-pole dual-mode filter with high selectivity, inset with a photograph of the fabricated filter.

3.3 Dual-mode Bandpass-Filter with Non-uniform Q (Quality Factor) Distribution

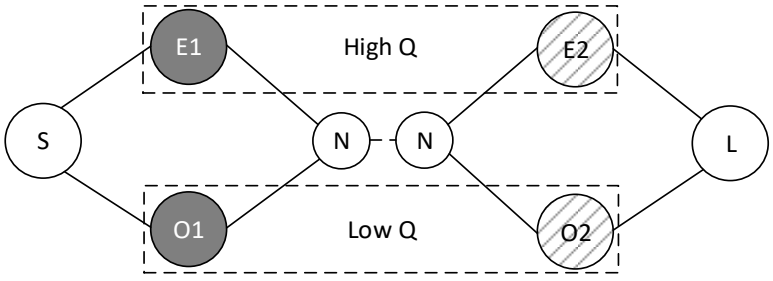

Figure 3.11 Topology of the dual mode filter with non-uniform Q distribution

In [4], a 4-pole dual-mode lossy filter was presented with a non-uniform Q distribution method, in which directly coupling between resonators is used for the dual-mode filter implement. In this section, we present an investigation of applying the non-uniform Q distribution method on a dual-mode filter with a cascaded configuration. This cascaded

configuration has an inline structure which is more adaptive to the further tunable implementation. As discussed in the previous section, the even-mode and the odd-mode of the resonator are de-coupled. The 4-pole filter has its two odd-mode frequencies in the middle of the passband while the two even-mode frequencies are at the passband edges. Therefore, the filter network can be considered as a transversal pair network consisting of an odd-mode path and an even-mode path. In the aspect of the passband insertion loss, the path of even-mode mainly contributes to the insertion loss at the passband edges, while the odd-mode path affects the middle. Therefore, to achieve a good passband flatness, the non-uniform Q distribution method can be exploited using such a feature. The topology of the 4-pole dual-mode filter with non-uniform Q distribution is shown in Figure 3.11, which consists of two high-Q even modes and two low-Q odd modes. The characteristics of this topology are synthesised by the coupling matrix in the following section.

3.3.1 Coupling Matrix Synthesis

Generally, the coupling matrix is purely real in lossless conditions as (3.4). Considering the dissipative losses in the resonators, the coupling matrix of the 4-pole dual-mode filter with finite unloaded quality factor can be written as

$$\begin{bmatrix} 0 & 0.8554 & 0.5805 & 0 & 0 & 0 & 0 & 0 \\ 0.8554 & 0.9651-j\delta_{O1} & 0 & -0.8554 & 0 & 0 & 0 & 0 \\ 0.5805 & 0 & -1.0159-j\delta_{E1} & 0.5805 & 0 & 0 & 0 & 0 \\ 0 & -0.8554 & 0.5805 & 0 & 1.1 & 0 & 0 & 0 \\ 0 & 0 & 0 & 1.1 & 0 & 0.7408 & 0.46 & 0 \\ 0 & 0 & 0 & 0 & 0.7408 & -0.6095-j\delta_{O2} & 0 & -0.7408 \\ 0 & 0 & 0 & 0 & 0.46 & 0 & 1.2667-j\delta_{E2} & 0.46 \\ 0 & 0 & 0 & 0 & 0 & -0.7408 & 0.46 & 0 \end{bmatrix} \tag{3.6}$$

where non-zero diagonal elements in the matrix become complex with imaginary parts ($j\delta_{E1}, j\delta_{O1}, j\delta_{E2}$ and $j\delta_{O2}$) representing the dissipative losses within each node respectively. The relationship between the loss elements δ_0 and the unloaded quality factor of the resonator Q_{u0} is given by

$$\delta_0 = \frac{f_0}{BW \cdot Q_{u0}} \tag{3.7}$$

where the BW is the filter bandwidth and f_0 is the centre frequency. Considering a filter with a uniform resonator Q-factor of 100 ($\delta_{E1}, \delta_{O1}, \delta_{E2}, \delta_{O2} = 0.119$), the calculated frequency responses from the coupling matrix is given by the red dash line in Figure 3.12. The passband edges have more loss comparing to the middle leading to large in-band variation. In order to flatten the passband, non-uniform Q distribution can be implemented by introducing the extra loss elements $\Delta\delta_{O1} = 0.25$ and $\Delta\delta_{O2} = 0.35$ into the odd-mode nodes. Consequently, the complex coupling matrix is now given as (3.8), and the calculated frequency responses are given in Figure 3.12 in solid lines. The result presents an improved passband flatness after the nonuniform Q distribution, and the insertion loss level is expensed.

$$\begin{bmatrix}
0 & 0.8554 & 0.5805 & 0 & 0 & 0 & 0 & 0 \\
0.8554 & 0.9651 - j0.369 & 0 & -0.8554 & 0 & 0 & 0 & 0 \\
0.5805 & 0 & -1.0159 - j0.119 & 0.5805 & 0 & 0 & 0 & 0 \\
0 & -0.8554 & 0.5805 & 0 & 1.1 & 0 & 0 & 0 \\
0 & 0 & 0 & 1.1 & 0 & 0.7408 & 0.46 & 0 \\
0 & 0 & 0 & 0 & 0.7408 & -0.6095 - j0.469 & 0 & -0.7408 \\
0 & 0 & 0 & 0 & 0.46 & 0 & 1.2667 - j0.199 & 0.46 \\
0 & 0 & 0 & 0 & 0 & -0.7408 & 0.46 & 0
\end{bmatrix} \tag{3.8}$$

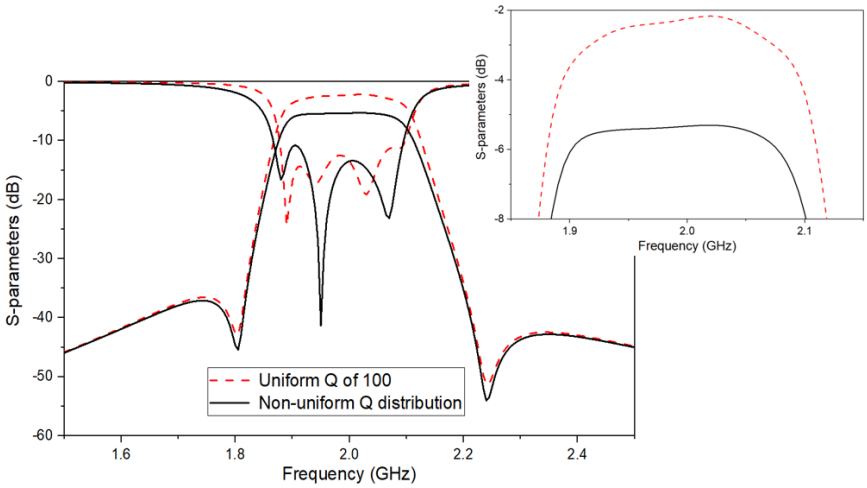

Figure 3.12 Theoretical curves of coupling matrix with a uniform resonator Q factor of 100 and non-uniform Q distribution.

3.3.2 Loss Microstrip Filter Implementation

3.3.2.1 End Loading Implementation

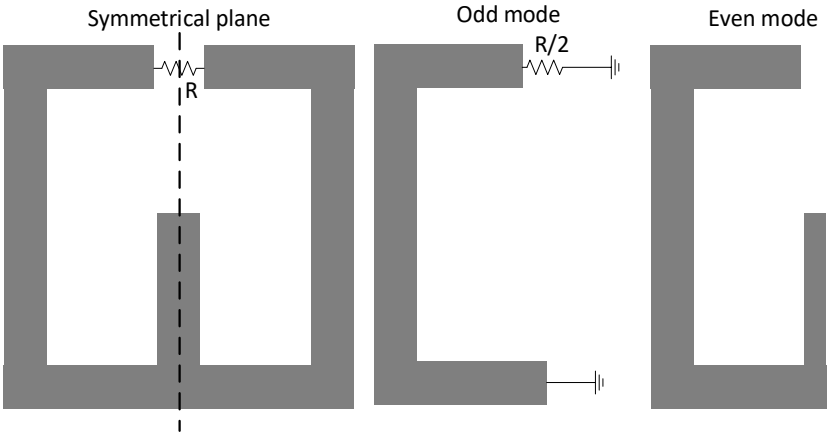

(a) (b) (c)

Figure 3.13 (a) Layout of a conceptual dual-mode resonator with resistive loading; (b) Odd mode equivalent circuit; (c) Even mode equivalent circuit.

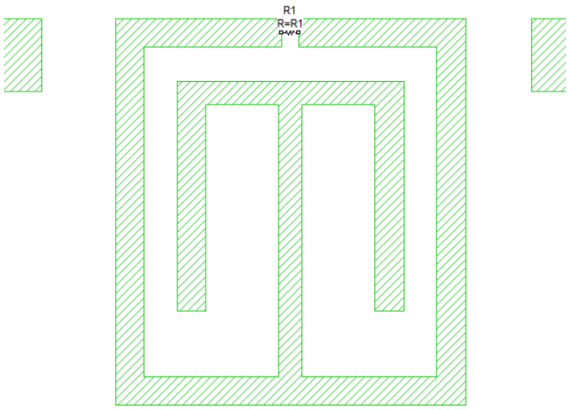

(a)

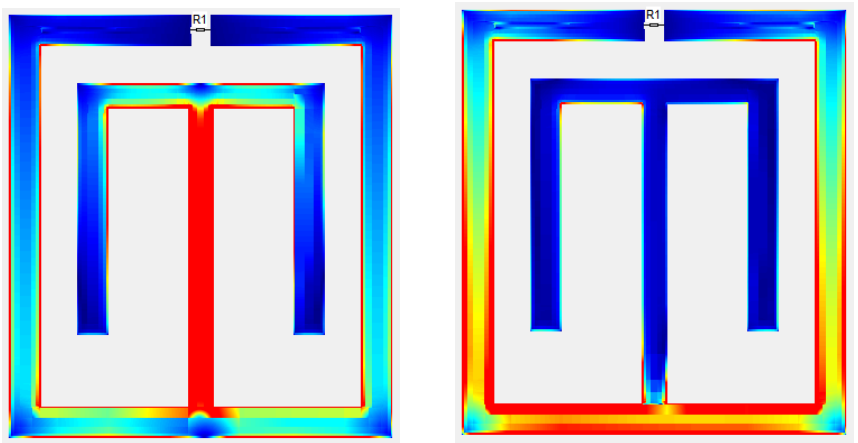

(b) (c)

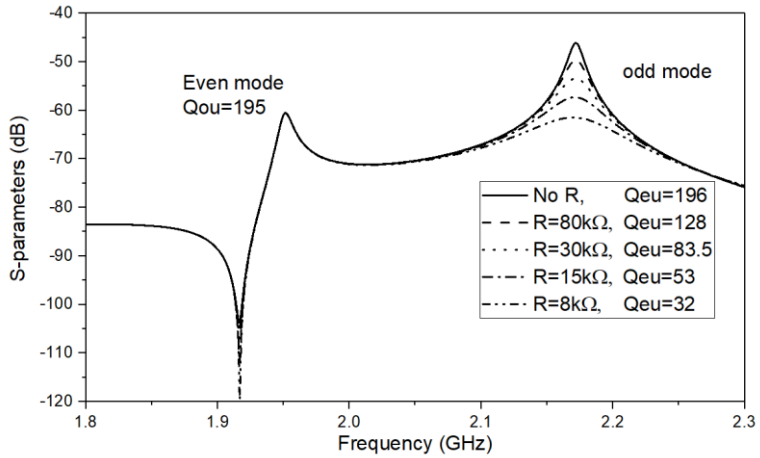

(d)

Figure 3.14 (a) Layout of the resonator with asymmetrically placed resistor, weakly coupled ports for the unloaded Q extraction; (b) Current distribution at even mode frequency; (c) Current distribution at odd mode frequency; (d) Frequency responses and extracted unloaded quality factors for different resistances.

Figure 3.13 shows the conceptual resonator layout for nonuniform Q distribution implement. Resistors are loaded between two ends of the open-loop resonator to introduce additional loss into odd-modes. Odd/even-symmetrical plane analysis is applied to the dual-mode resonator. When the odd-symmetrical plane presents as shown in Figure 3.13 (b), the loaded resistors are connected to the virtual ground by half-value of resistance introducing additional losses to the odd-modes. In the case of even-modes, Figure 3.13 (c), the resistor is equivalent to terminating to an open-circuit along the symmetrical plane. Therefore, the odd-modes Q-factor is reduced but the even-modes are not affected. Figure 3.14 (a) shows the extraction configuration for the unloaded Q factor of a dual-mode resonator with the proposed loading resistor. The current distributions at even/odd mode frequencies are given in Figure 3.14 (b), (c) respectively. The light colour area has a higher current. The effect of the loading resistor can be found in Figure 3.14 (d). The dual-mode resonator has an intrinsic uniform Q factor of 195 for both even and odd mode due to the conducting loss and the dielectric loss. By attaching the loading resistance from 80 kΩ to 8 kΩ, the unloaded Q factor of the odd mode experiences a decrease from 195 to 32, while the Q_u of the even mode remains the constant.

To validate the proposed concept, a lossy dual-mode microstrip open-loop filter is designed at 4 GHz with an FBW of 9%, as illustrated in Figure 3.15 (a). The simulation

results of the filter without any resistor loading is given in Figure 3.15 (a), while the simulation & measurement results after resistor loading are plotted in Figure 3.15 (b) and (c) respectively. As can be seen, in the simulation, the passband flatness of the filter is improved after resistor loading. However, the measurement has a serious mismatching. Our further investigation figures out that the measured mismatching is caused by the parasitic capacitance of the surface mounting resistor. For a general 0402 packaged chip resistor with high resistance, empirically, the parasitic capacitance can have a value of 0.03 – 0.04 pF. The high-frequency performance electrical model of the chip-resistors is detailed in the Appendix. The effect of this capacitance is expected to be suppressed.

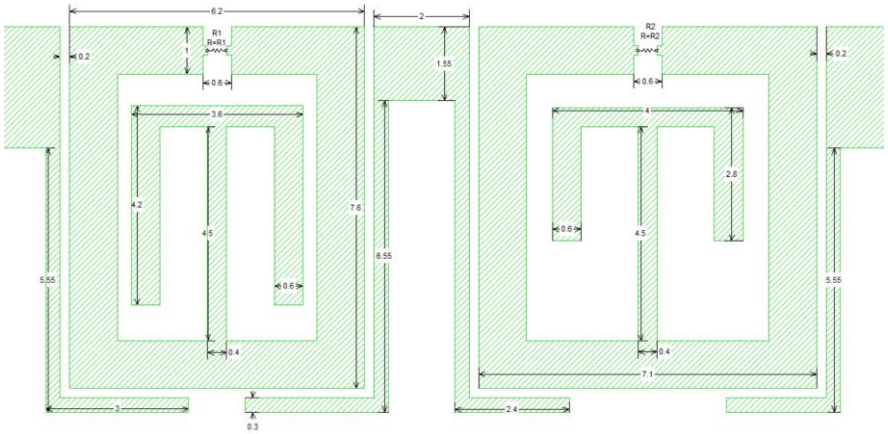

(a)

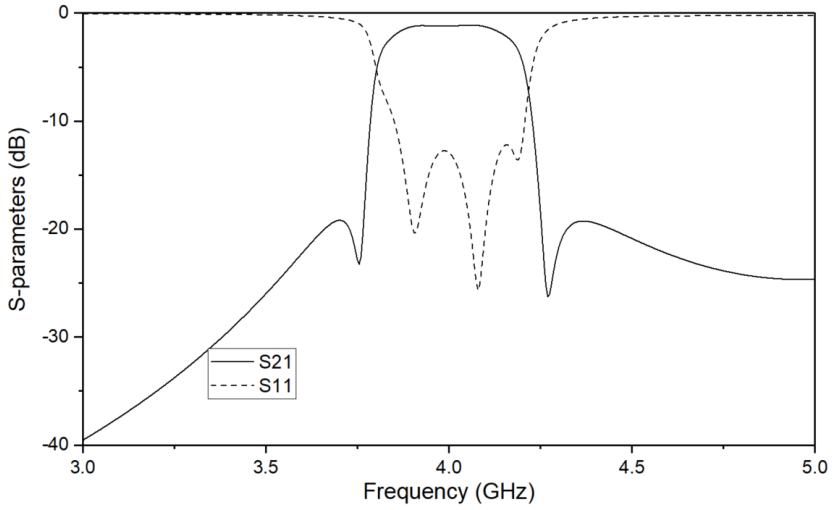

(b)

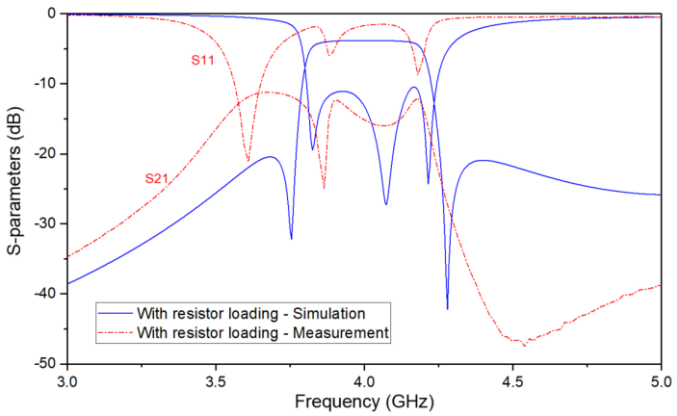

(c)

Figure 3.15 Lossy filter operating at 4GHz with 9% fractional bandwidth, (a) Layout of the dual-mode filter with resistance loading; (b) Frequency responses of the filter without resistor loading; (c) Simulation and measurement results after the resistor loading.

3.3.2.2 Stub Loading Implement

The electric field is dominant closing to the open end of the resonator, and this will lead to a larger electric potential to the ground. Therefore, odd-mode unloaded-Q and resonating frequency are much sensitive to the loading resistive and capacitance when the components are loaded close to the open-end. In order to remove the effect of the parasitic, estimated parasitic capacitance can be taken into the simulation to adjust the dimension of resonators. However, considering the uncertain tolerance of the parasitic capacitance of each resistor, this compensation method is not a good solution. To suppress the effect of this parasitic capacitance, the loading position of the resistor can be moved from the open end of the resonator toward the middle where the electric field is less dense Figure 3.16 (a). For the investigation, we assume a resistor for loading has a resistance of 500 Ω and a parasitic capacitance of 0.035 pF while the resistor is symmetrically loaded on the resonator with a connection distance of dx. After this resistive loading R, the unloaded Q factor Q_{uo} of the odd mode now becomes

$$Q_{uo} = \frac{1}{Q_{uo0}} + \frac{1}{Q_R} \tag{3.9}$$

where Q_{uo0} is the origin Q of the resonator without a resistor, and the Q_R represents the additional loss brought by the resistor. If the microstrip resonator is lossless, the extracted unloaded Q in EM simulation is equal to the Q_R. Using weak excitation

configuration, the frequency responses for different loading distance dx are given in Figure 3.16 (b) which indicates the variation of the resonator unloaded Q factor and the resonating frequency shifting of the resonator. As the extracted results, the resonator with a shorter loading distance dx is less affected by the parasitic capacitance but also less affected by the resistance. It is interesting that the even mode resonating frequency is less disturbed by the parasitic capacitance comparing to the odd mode. To mathematically predict the effect of the resistor after the modification, an evaluation for the Q_R is given by [4]

$$\begin{aligned} W_0 &= 2\times\frac{1}{2}\int_0^{\frac{\pi}{2}}\frac{V_0^2\sin^2\theta}{Z_1\omega_0}\cdot d\theta \\ P_R &= 2\times\frac{V_0^2\sin^2\theta_1}{2\times R/2} \end{aligned} \tag{3.10}$$

$$Q_R = \omega_0\frac{W_0}{P_R} = \frac{\pi R}{8Z_1\sin^2\theta_1} \tag{3.11}$$

where W_0 is the stored energy in odd-mode, V_0 is the maximum voltage in the odd-mode, $\theta_1 = \frac{\pi\cdot dx}{2l}$ is the electrical length from the resistor tapping position to the resonator centre respect to the central frequency, and the l is the physical length of the odd-mode resonator. The shifting of the odd mode resonating frequency can be obtained by calculating the odd-mode's input admittance Y_{ino}, and it is given by

$$\begin{aligned} Y_{in1} &= j\left(\omega C_p - \frac{Y_1}{\tan\theta_1}\right) \\ Y_{ino} &= Y_1\cdot\frac{Y_{in1} - jY_1\tan\theta_2}{Y_1 - jY_{in1}\tan\theta_2} \end{aligned} \tag{3.12}$$

where C_p is the parasitic resistance, and the θ_2 is the electrical length from the resistor tapping position to the resonator open-end. It is notable that electrical length θ_1, θ_2 are varying against the frequency ω. Thus, the odd mode resonating frequency can be found when the $Y_{ino} = 0$. The mathematically predicted Q_R and the frequency shifting Δf are also plotted in Figure 3.16 (c) for a comparison with the extraction. As can be seen, the calculation is very close to the extracted results. In such a manner, the balance

can be made between the loading position and the resistor's characteristics.

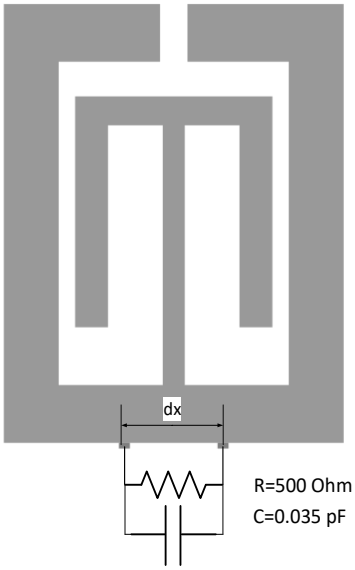

(a)

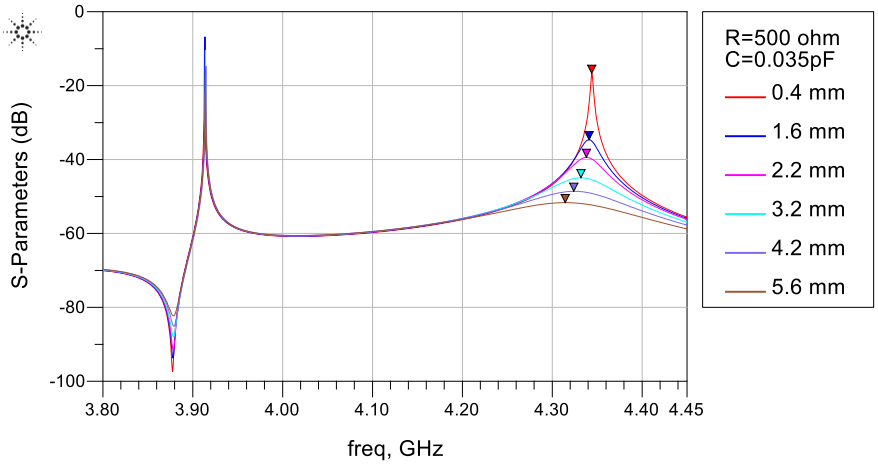

(b)

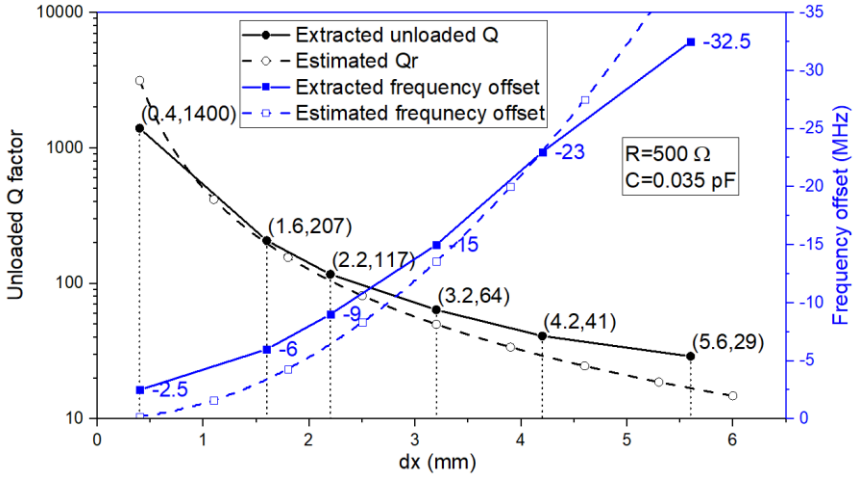

(c)

Figure 3.16 (a) Modified resistance loading; (b) Weak excited frequency responses of the resistor loaded resonator for different loading positions; (c) Extracted unloaded Q factors and frequency offsets against the distance dx, inset with estimated Q_r from equation (3.11).

To avoid bending the resonator for placing the SMD resistor, symmetrically extended stubs can be applied as shown in Figure 3.17 (a). The influence of these two additional lines can be offset by using the EM simulation. The proposed filter has a dimension of 20 $mm \times 10$ mm on a Rogers substrate with a relative dielectric constant of 3 and a thickness of 1.02 mm. The centre frequency of the filter is 4 GHz with a fractional bandwidth of 7%. Two resistors (R = 100 Ω and 150 Ω) are loaded on symmetrical planes of resonators. As illustrated in Figure 3.17 (c), the measured filter-passband insertion loss is around 3.6 dB after resistors attached with clearly middle band insertion loss absorption while the return loss is kept above 10 dB. An asymmetrical return loss ($S_{11} \neq S_{22}$) is exhibited in the passband due to the asymmetric configuration of the filter. Two transmission zeros are located at 3.83 GHz and 4.25 GHz enhancing the selectively.

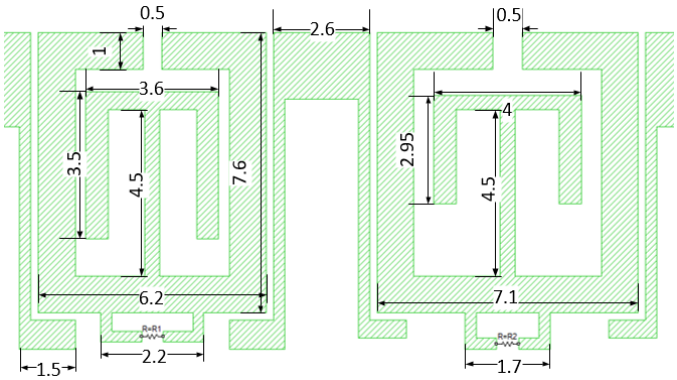

(a)

(b)

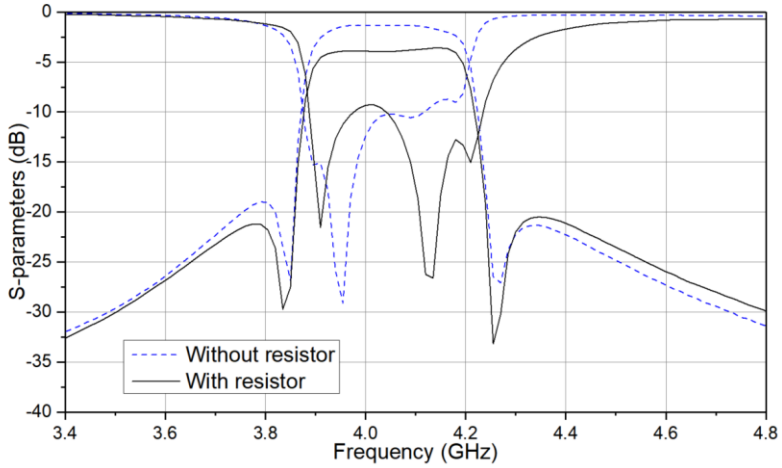

(c)

Figure 3.17 (a) Layout of the proposed lossy filter; (b) Photography of the fabrication; (c) Measurement of the lossy filter at 4 GHz with a comparison to the filter without resistor loading.

In conclusion, a new type of lossy dual-mode bandpass filter with cascaded configuration has been investigated in this Section. The filter passband flatness can be improved by purposely making the odd modes lossier with lower and unequal Q factors in a simple manner of loading resistors on the even-odd symmetrical plane of dual-mode resonators. Two experimental 4-pole filters of this type have been designed, fabricated, and tested. The employment of non-resonating nodes does not affect the lossy implement and can be used in higher-order filter design in the future. The lossy filter with the proposed layout is going to be extended to the reconfigurable filter in the next Section.

3.4 Varactor-Tuned Dual-mode Bandpass Filter With Non-Uniform Q Distribution

Since passband flatness can be only achieved by a lossy technique with a particular Q distribution, the challenge of the tunable lossy filter is maintaining a desired lossy distribution during the tuning, especially for the filter bandwidth tuning. Few efforts have been put on the tunable filter with lossy techniques. As a lossy filter based on dual-mode resonator topology has been discussed, varactor-based tunability of this type of lossy filter is demonstrated in this Section.

3.4.1 Coupling Matrix Synthesis

$$\begin{bmatrix} 0 & 0.8554+\Delta m_{S1} & 0.5805+\Delta m_{S2} & 0 & 0 & 0 & 0 & 0 \\ 0.8554+\Delta m_{S1} & 0.9651+\Delta m_{O1}-j\delta_{O1} & 0 & -0.8554-\Delta m_{S1} & 0 & 0 & 0 & 0 \\ 0.5805+\Delta m_{S2} & 0 & -1.0159-\Delta m_{E1}-j\delta_{E1} & 0.5805+\Delta m_{S2} & 0 & 0 & 0 & 0 \\ 0 & -0.8554-\Delta m_{S1} & 0.5805+\Delta m_{S2} & 0 & 1.1 & 0 & 0 & 0 \\ 0 & 0 & 0 & 1.1 & 0 & 0.7408+\Delta m_{3L} & 0.46+\Delta m_{4L} & 0 \\ 0 & 0 & 0 & 0 & 0.7408+\Delta m_{3L} & -0.6095-\Delta m_{O2}-j\delta_{O2} & 0 & -0.7408-\Delta m_{3L} \\ 0 & 0 & 0 & 0 & 0.46+\Delta m_{4L} & 0 & 1.2667+\Delta m_{E2}-j\delta_{E2} & 0.46+\Delta m_{4L} \\ 0 & 0 & 0 & 0 & 0 & -0.7408-\Delta m_{3L} & 0.46+\Delta m_{4L} & 0 \end{bmatrix}$$

(3.13)

The proposed 4-pole tunable dual-mode lossy filter with an initial fractional bandwidth of 10% centred at 1.6GHz can be modelled by the coupling matrix of (3.13), which composed of 2 transversal networks in series with two non-resonating nodes. Each transversal network represents one dual-mode resonator. Similar to the previous, the dissipative loss in the filter has been included in the coupling matrix as $j\delta_0$ on diagonal. The value of $j\delta_{11}$ and $j\delta_{33}$ represents the added resistive loss for the odd-mode nodes. Thus, the filter network has a non-uniform Q distribution of $Q_{uo1} = 33$, $Q_{ue1} = 100$, $Q_{uo2} = 25$ and $Q_{ue2} = 100$. To perform the tunability in the coupling matrix, additional variable elements $\Delta m_{ij}(i, j = S, 1,2, O, E \cdots)$ denote the coupling variation and resonating frequency variation. Bandwidth reconfiguration is achieved by separating four nodes' resonating frequencies by Δm_{ii} with corresponding coupling variation $\Delta m_{ij}(i \neq j)$. Figure 3.18 (a) shows the matrix frequency response of frequency variation from 1.45 GHz to 1.75 GHz with a fractional bandwidth of 10%. The bandwidth variation is also given in Figure 3.18 (b), in which the filter passband is tuned from 10% to 20% at 1.6GHz with the same non-uniform Q distribution. The filter passband keeps a good passband flatness of IL variation < 1dB when the frequency and bandwidth are tuned. Its dispersive loss remains the same. Therefore, it is possible to achieve a good passband flatness for the tunable filter using constant resistance loadings.

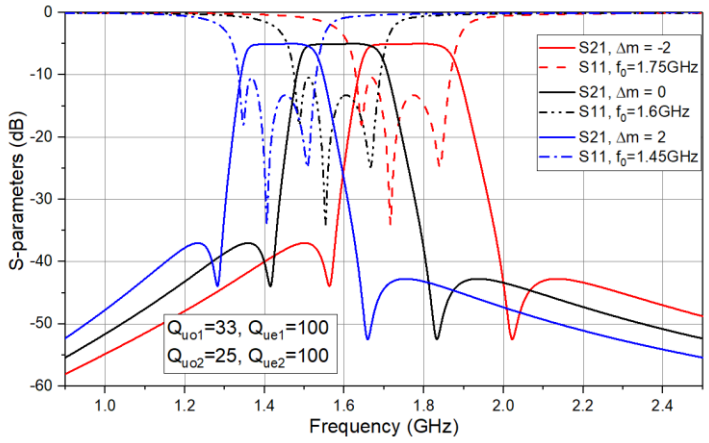

(a)

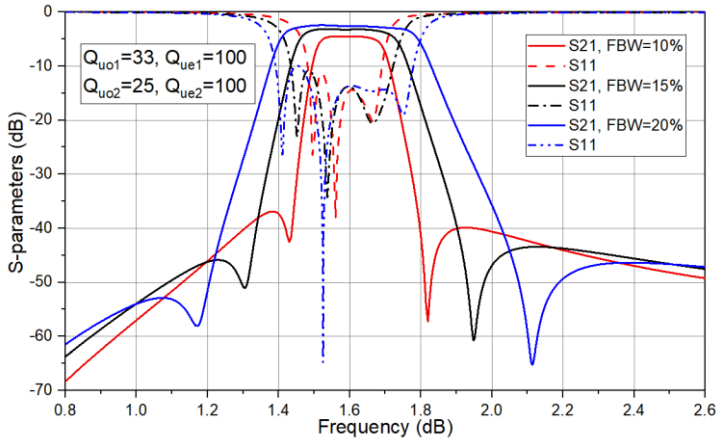

(b)

Figure 3.18 Reconfigurable characteristics of the proposed lossy filter synthesized by coupling matrix, with an unloaded Q distribution of 33, 100, 25, 100 (a) Frequency tuning; (b) Bandwidth tuning.

3.4.2 Tunable Filter Design

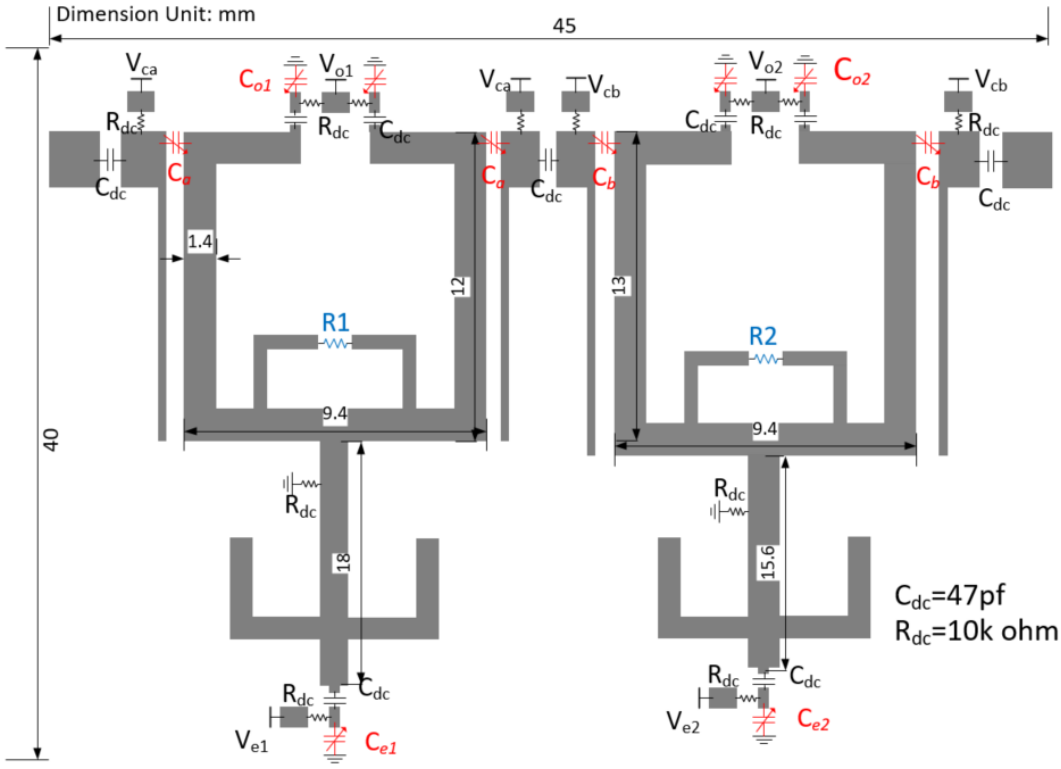

Figure 3.19 Layout of the proposed 4-pole tunable lossy filter including the DC biasing circuit.

The design layout of the proposed tunable filter is shown with the DC biasing circuit in Figure 3.19. Six controlling voltages can be found in the layout for controlling the varactors. 47pF capacitors and 10 kΩ resistors are used for DC block and RF chock. The tunability of bandwidth is provided by loading varactors C_a and C_b between resonators to vary the coupling. Centre frequency tuning is introduced by varactors C_{o1}, C_{o2}, C_{e1}, and C_{e2}. The equivalent circuits for odd and even modes are given in Figure 3.20 using symmetrical plane analysis. Note that C_{o1} and C_{o2} have the effect not only on the odd-mode resonating frequency but also on the even-mode resonating frequency. The varactors C_{e1} and C_{e2} are used to adjust the even-mode resonating frequency only. In the EM simulation, the resonating frequencies can also be found by the weak excitation method. Note that, we should keep the modal frequencies $f_{e1} < f_{o2} < f_{o1} < f_{e2}$ at all the tuning states.

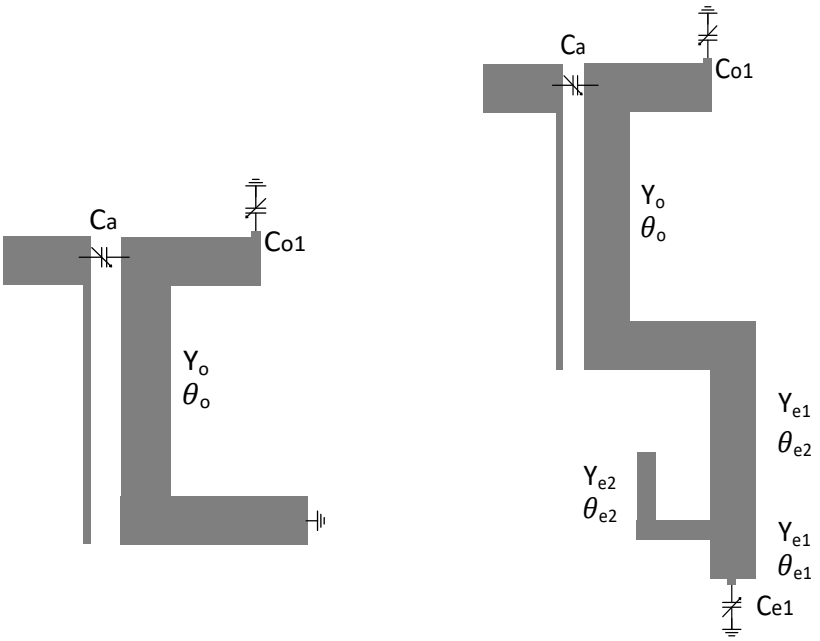

(a) (b)

Figure 3.20 Circuit model of (a) odd mode and (b) even mode.

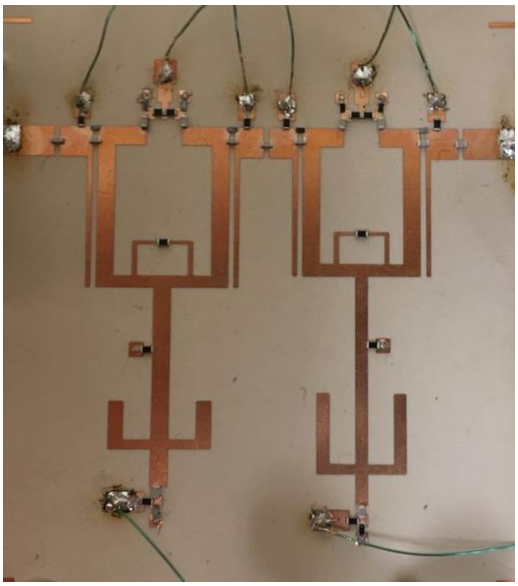

Figure 3.21 Photograph of the fabricated 4-pole tunable dual-mode filter with non-uniform Q distribution.

A prototype filter, as shown in Figure 3.21, is fabricated on RO3003 with a thickness of 1.02 *mm* and dielectric constant of 3. The filter has a layout size of $40\ mm \times 45\ mm$. All the variable capacitances are implemented with the MA46H120 varactor with tuning range of 0.17 pF to 1.1 pF. To obtain a stronger external coupling, additional capacitors with capacitances of 0.4 pF and 0.3 pF are paralleled with the external Q

control varactors C_a and C_b. The extracted external Q of the even and odd mode of the first resonator is given for different capacitances C_a in Figure 3.22. Varactors are controlled by the DC biases with a range of 0 V – 20 V. By using the full-wave EM simulation [6], the dielectric losses and metal losses are considered. The loss in varactors is taken into the simulation by an equivalent resistance in parallel as $R = Q_u/(\omega C)$ [5], where the Q_u is the unloaded Q of varactors, ω is the frequency and C is the capacitance of varactors. Panasonic chip resistors of 50 Ω and 100 Ω are chosen on purpose for a desired non-uniform Q distribution. With different combinations of DC bias voltages, bandwidth and centre frequency tuning are performed. The measurements have been obtained using Agilent 8510B microwave network analyzer.

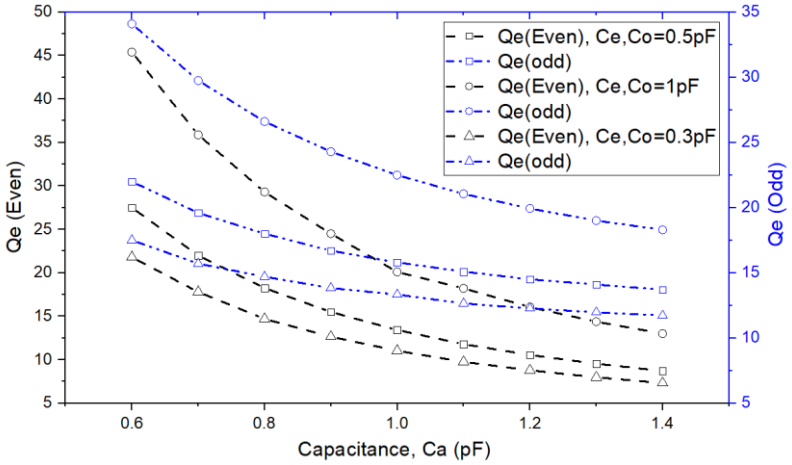

Figure 3.22 Extracted external quality factors for the even and odd mode when the capacitance C_a changes.

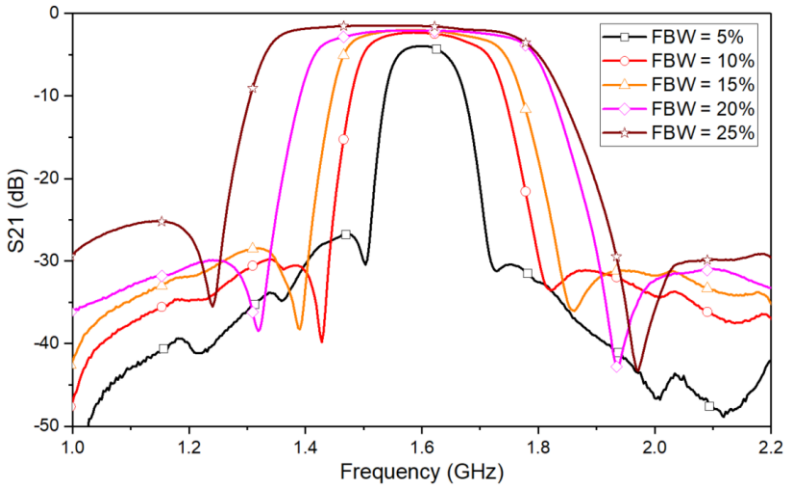

(a)

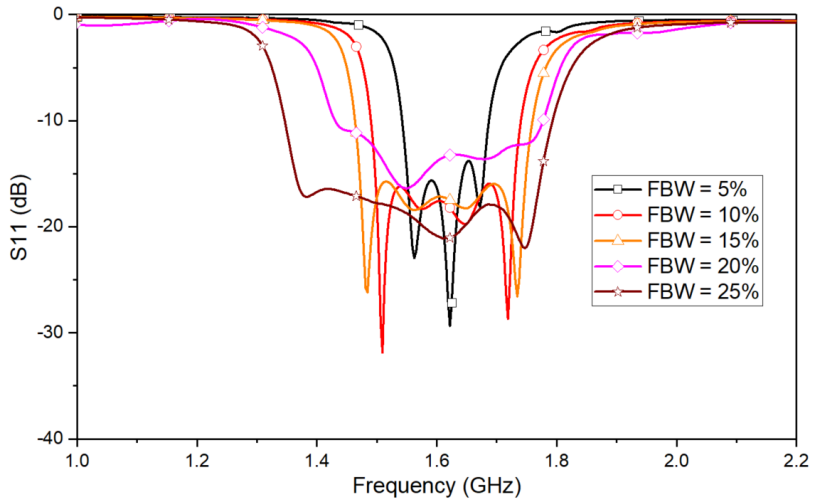

(b)

Figure 3.23 Bandwidth tuning of the fabricated 4-pole tunable filter without the resistor loading, (a) S21; (b) S11.

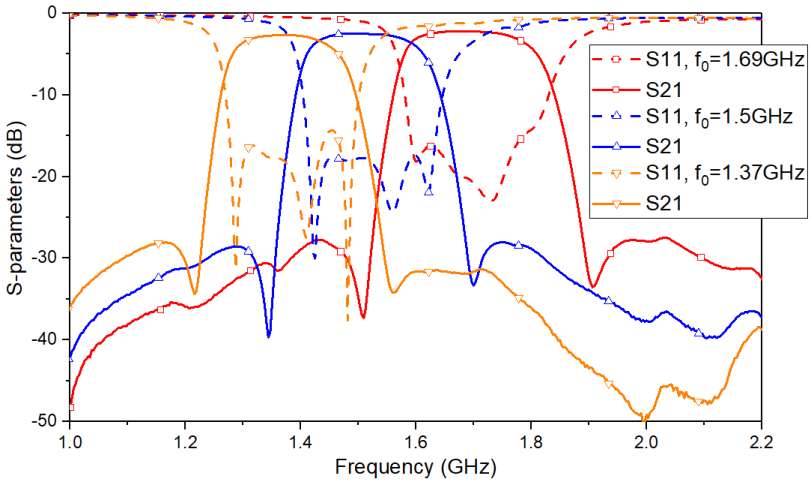

Figure 3.24 Centre frequency tuning of the measured filter.

Figure 3.23 shows the measurement results for the bandwidth tuning of the fabricated filter. The FBW of filter passband is tuned from 5% (80 MHz) to 20% (320 MHz) at a constant centre frequency of 1.6 GHz. A maximum bandwidth of 25% (390 MHz) can be achieved at the centre frequency of 1.56 GHz. As shown, the band-side transmission zeros are slightly moving away from the passband when the bandwidth is increasing. This is due to the ratio of the even to odd modes' external Q-factors are varying during the bandwidth tuning. The measured insertion loss is 1.5 dB for FBW = 25% and 2.3 dB for FBW = 10%. A rapid rise in insertion loss (3.95 dB) can be observed when the

FBW is 5%. Meanwhile, the tunability of the centre frequency of the filter is demonstrated in Figure 3.24 with the frequency coverage of 1.37 GHz – 1.69 GHz and a constant fractional bandwidth of 10%.

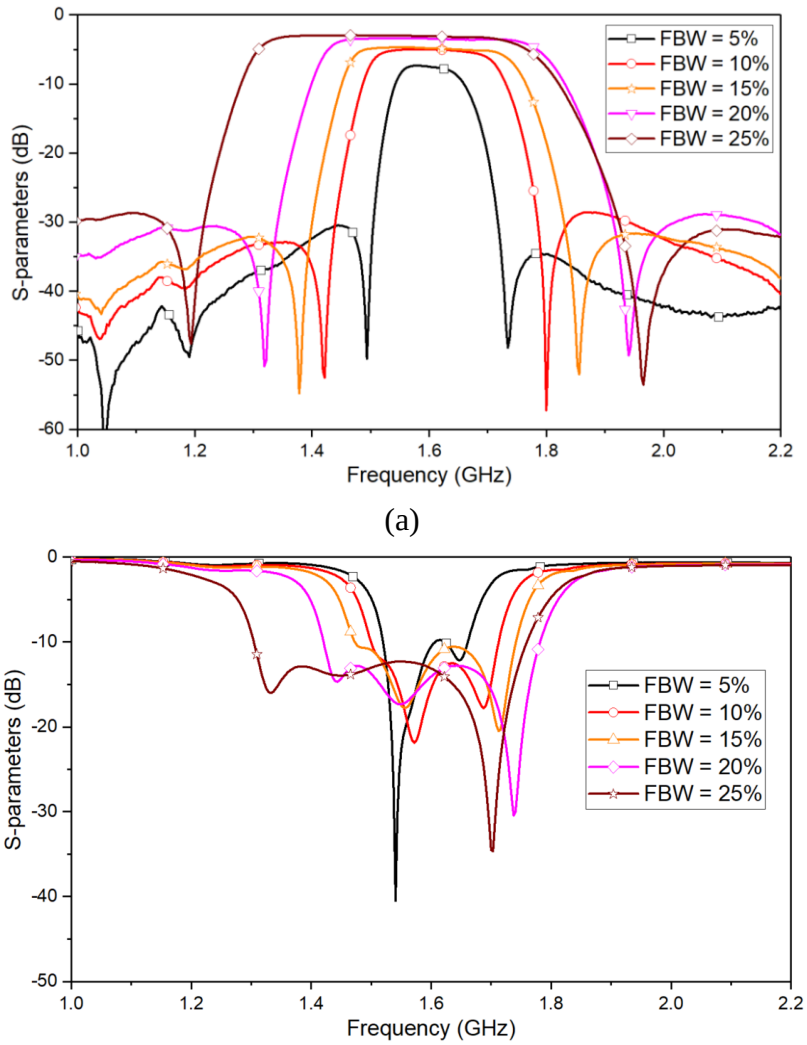

Figure 3.25 Experimental results of the filter for the fractional bandwidth tuning from 5% to 25%; (a) S21; (b) S11.

After lossy resistors are loaded, Figure 3.25 shows the filter bandwidth tuning from 5% to 25%. The non-uniform Q distribution by resistive loading is successfully improving the passband flatness of all bandwidth states, except for the FBW = 5%. At 5% FBW state, the left edge of the passband is higher than the right edge. Considering the two even modes loaded with varactors, at the narrow bandwidth state, the lower frequency node is loaded by a small capacitance while the higher frequency node is loaded by a

large capacitance. Note that a varactor with larger capacitance has a lower Q which causes unequal unloaded-Q factors of two even modes. Consequently, the passband at a narrow bandwidth state, which is much impacted by the resonator Q, is sloping toward the higher band edge.

To demonstrate the improvement in the passband flatness of the filter for the rest of bandwidth states, Figure 3.26 shows the comparison of the passband insertion-loss variation between filters with and without the non-uniform Q distribution. The insertion loss variations are given within the frequency range of $f_0 \pm 20\%BW$, $f_0 \pm 30\%BW$, $f_0 \pm 40\%BW$, and $f_0 \pm 50\%BW$ respectively. As shown, for the bandwidth state of FBW = 10%, the passband variation has been improved from 1.2 dB to 0.6 dB with at the expense of 2.6 dB passband insertion loss (from 2.3 dB to 4.9 dB). The overall improvement of the insertion loss variation at 20% FBW is from 1.3 dB to 0.76 dB with insertion loss raising from 2.1 dB to 3.3 dB. Meanwhile, the return loss within the passband of the tuned filter has been maintained under 10 dB. A good adjacent-band attenuation is larger than 25 dB.

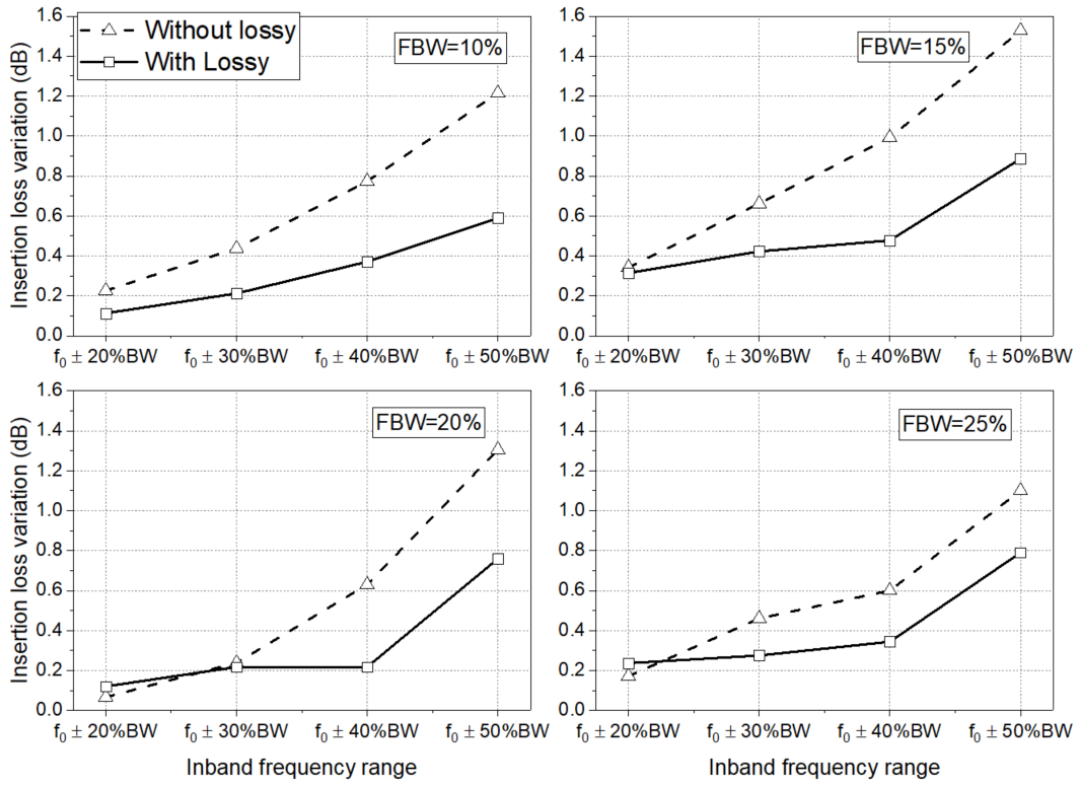

Figure 3.26 The improvement in the passband flatness for different bandwidth states by the non-uniform Q distribution, the insertion loss variation vs the frequency range in the passband.

Furthermore, the filter also preserves a good passband flatness during the centre frequency tuning. In Figure 3.26, the passband insertion loss variation attains 0.5 dB with a constant insertion loss of 4.8 dB when the centre frequency is varied from 1.35 GHz to 1.6 GHz with 10% FBW. Filter wideband responses with loading resistors are plotted in Figure 3.28 with the centre frequency of 1.6 GHz and tuned fractional bandwidths of 10% and 20%. A spurious resonating frequency can be found at 3.7 GHz which is caused by the non-resonating nodes.

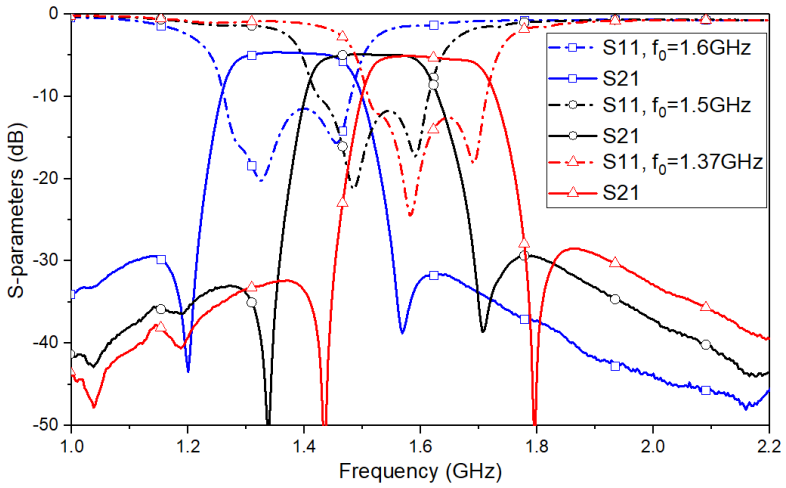

Figure 3.27 Frequency tuning of the measured filter with resistor loading.

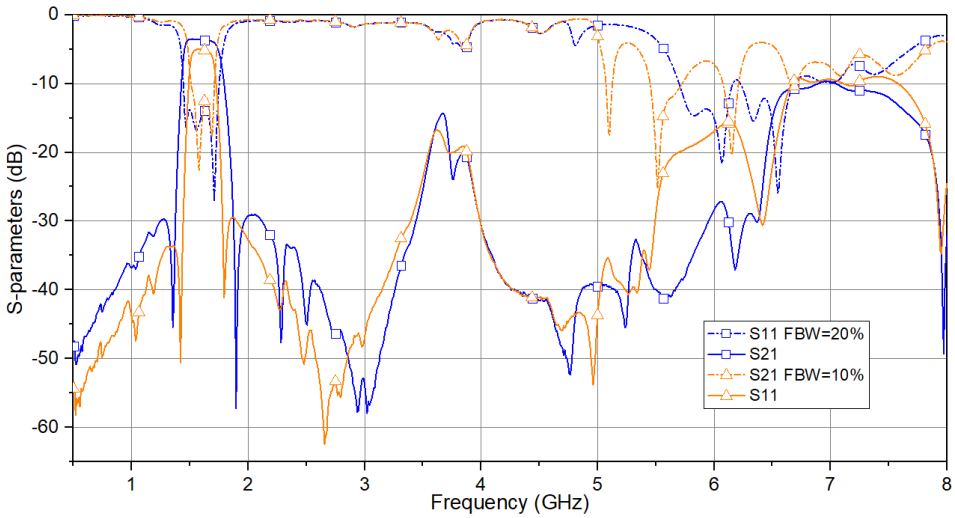

Figure 3.28 Wideband responses of the tunable filter with tuned 10% and 20% FBW.

3.5 Conclusion

A new type of tunable lossy dual-mode microstrip bandpass filter was introduced with both bandwidth and centre-frequency tuning. Varactors are used in continuous tuning of resonating frequency and coupling. The filter passband flatness can be enhanced in a simple way of loading resistors on the symmetrical plane of the resonator to reduce odd-mode Q. Measurement results have been demonstrated showing interesting characteristics. However, this type of tunable filter with the nonuniform Q distribution method fails to perform a good passband flatness when the bandwidth is tuned down to 5% FBW. In this regard, a novel lossy configuration for the narrow-bandwidth filter is going to be demonstrated in the next Chapter.

3.6 Reference

[1] J. S. Hong, H. Shaman, and Y. H. Chun, 'Dual-Mode Microstrip Open-Loop Resonators and Filters', *IEEE Transactions on Microwave Theory and Techniques*, vol. 55, no. 8, pp. 1764–1770, Aug. 2007.

[2] W. Tang and J. S. Hong, 'Varactor-Tuned Dual-Mode Bandpass Filters', *IEEE Transactions on Microwave Theory and Techniques*, vol. 58, no. 8, pp. 2213–2219, Aug. 2010.

[3] W. Tang and J.-S. Hong, 'Varactor-Tuned Dual-Mode Bandpass Filters', *IEEE Transactions on Microwave Theory and Techniques*, vol. 58, no. 8, pp. 2213–2219, Aug. 2010.

[4] L. F. Qiu, L. S. Wu, W. Y. Yin, and J. F. Mao, 'A Flat-Passband Microstrip Filter With Nonuniform- Q Dual-Mode Resonators', *IEEE Microwave and Wireless Components Letters*, vol. 26, no. 3, pp. 183–185, Mar. 2016.

[5] J.-S. Hong, *Microstrip Filters for RF / Microwave Applications*, 2nd Edition edition. Hoboken, N.J: Wiley-Blackwell, 2011.

[6] *Sonnet*. Sonnet Software Inc.

CHAPTER 4
MULTIPOLE HIGH SELECTIVE TUNABLE BANDPASS FILTER WITH IMPROVED PASSSBAND FLATNESS

4.1 Introduction

In Chapter 3, a dual-mode tunable filter using non-uniform Q distribution has achieved a bandwidth tuning from 10% FBW to 25% FBW with good improved passband flatness. However, it failed to keep a good flatness at the narrow bandwidth state of 5%. A class of inline filters with wide range bandwidth tunability has been presented in [1], which can achieve good in-band flatness at narrow bandwidth state (3.6%) using the predistortion technique. However, the drawback of using predistortion is obvious. The low return loss of such technique requires an extra isolator in the RF chain to absorb the high reflection.

In this chapter, a novel tunable lossy filter is presented with selectivity enhancement. It is aimed to tackle more challenging issues of narrow passband flatness (down to 2% fractional bandwidth) and wide bandwidth tuning (up to 1:8) with a multipole high selective filter response. In Section 4.2, fixed filter design is described first, which adopts a dual-behaviour resonator (DBR) to provide transmission-zeros for selectivity enhancement. This is then extended in Section 4.3 to implement bandwidth tuning with two adjustable band-side transmission zeros, and characterisation of capacitively-loaded DBR resonator is also presented. Because tunable components are implemented in the circuit, very limited space is left for RCCs. A novel centre-loaded resistive-cross coupling (CLRCC) path is introduced for passband flatness enhancement. The purpose of the introduced novel RCCs structure is to adapt the structural requirement of tunable filter circuits.

4.2 Filter with Dual-behaviour Resonators (DBR)

Dual behaviour resonator can not only generate a transmission pole, but also introduce a pair of transmission zeros on each side of the passband enhancing the selectivity of

the bandpass filter [2].

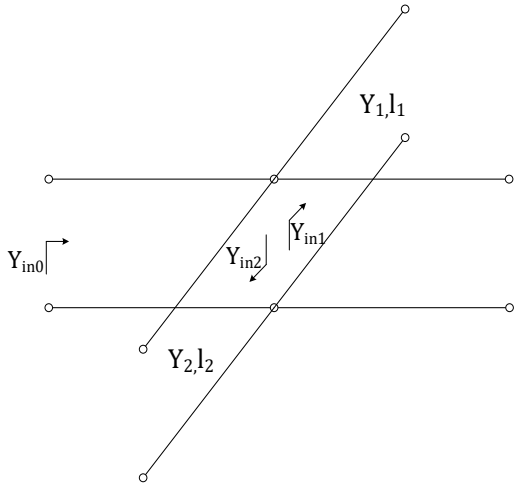

Figure 4.1 Basic structure of a dual-behaviour resonator (DBR).

Figure 4.1 shows the basic structure of a dual-behaviour resonator where two shunted quarter-wavelength open stubs are connected to a 50-ohm transmission line resulting in a transmission pole with two transmission zeros on two sides. General equations for the input admittance Y_{in0} of the resonator are given below

$$Y_{in1} = Y_1 \tan \theta_1 \tag{4.1}$$

$$Y_{in2} = Y_2 \tan \theta_2 \tag{4.2}$$

$$\begin{aligned} Y_{in0} &= Y_{in1} + Y_{in2} \\ &= Y_1 \tan\theta_1 + Y_2 \tan\theta_2 \end{aligned} \tag{4.3}$$

where, $\theta_n = \beta l_n$ $(n = 1,2)$ is the electrical length of each open-circuit stub, β is the propagation constant. Thus, three cases can be distinguished:

1. $Y_{in1} = \infty$ at frequency f_{z1} where the first transmission zero is observed.
2. $Y_{in2} = \infty$ at frequency f_{z2} where the second transmission zero is observed.
3. $Y_{in0} = 0$ at frequency f_0 where the resonance of the dual-behaviour resonator occurs.

Frequencies f_{z1}, f_{z2} and f_0 can be found when

$$\beta_{fz1} l_1 = \frac{\pi}{2}, \quad \beta_{fz2} l_2 = \frac{\pi}{2}$$
$$Y_1 \tan(\beta_{f0} l_1) + Y_2 \tan(\beta_{f0} l_2) = 0 \tag{4.4}$$

As can be seen, the frequencies of two transmission zeros are independently controlled by the length of open stubs l_1, l_2, while the transmission frequency f_1 of the resonator is not relative to only the length of stubs but also the characteristic admittance Y_1, Y_2 of the stubs. Generally, in the case of $f_1 < f_2$, a higher ratio of Y_1/Y_2 moves the transmission pole frequency closer to the upper transmission zero. Considering frequency shifting caused by coupling and tuning elements applied in practical design, an appropriate impedance ratio could be adjusted for the symmetrical allocation of transmission zeros.

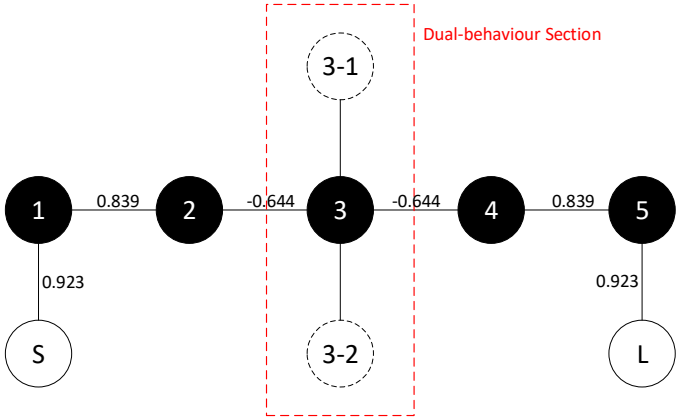

Figure 4.2 Topology of the proposed five-pole filter with dual-behaviour resonator

Figure 4.2 shows the proposed 5-pole filter topology in which the middle node is a DBR resonator, and normalised coupling coefficients are given in the topology. The in-band responses of the filter can be calculated using the normal filter synthesis method in [3]. The layout of a demonstrative filter designed at 1 GHz with an FBW of 6% is shown in Figure 4.3 (a). All filter layout parameters are given in an attached table. The design is based on the substrate RT/Duroid 6010 with a dielectric constant of 10.7 and a thickness of 1.27 *mm*. Uniform width (impedance) DBR resonator is applied with a resonating frequency of 1 GHz. Quarter-wavelength inverters provide the couplings between the hairpin resonator and the DBR (m_{23}, m_{34}), and this coupling coefficient is adjusted by

changing the tapping position t, the line width w_t, and the location of the transmission zeros. For a constant coupling coefficient of 0.644, the relationship between the centre-frequency-relative location of transmission zeros and the width of the quarter-wavelength inverter W_t is given in the Figure 4.3 (b). A larger width of the inverter W_t will provide a stronger coupling, but the coupling coefficient can be maintained by controlling the fractional bandwidth of two transmission zeros. Thus, the filter selectivity can be designed by choosing proper parameters. In this case, the locations of transmission zeros are predefined at 0.9 GHz and 1.12 GHz. The simulated frequency responses of the initial fixed example are given in Figure 4.4.

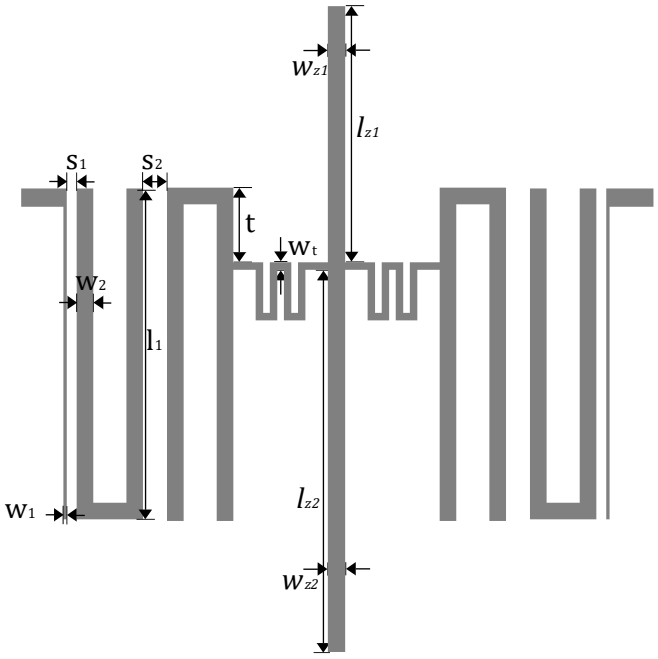

l_1	w_1	w_2	s_1	s_2	l_{z1}	w_{z1}	l_{z2}	w_{z2}	w_t	t
28.4	0.25	1	0.6	1.4	32	1.05	23	1.05	0.45	7.8

(a)

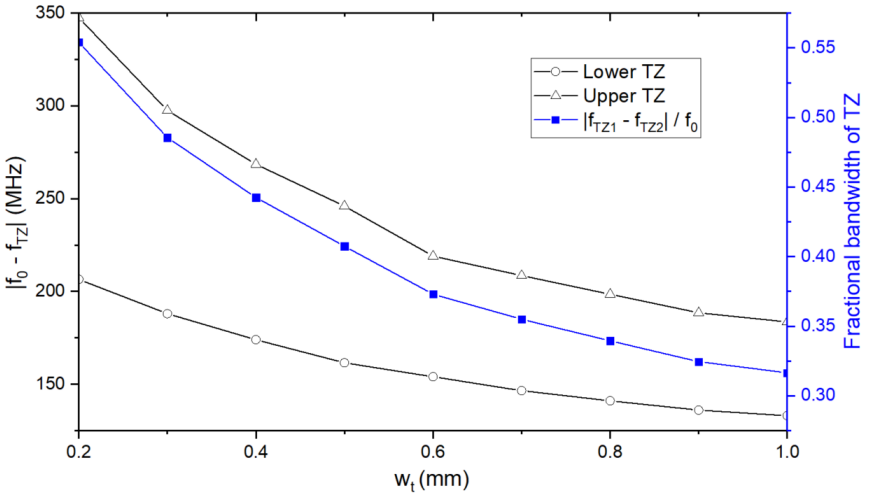

(b)

Figure 4.3 (a) Layout of the filter with DBR (unit: *mm*); (b) For a constant coupling coefficient of 0.644, locations of transmission zeros to the centre frequency vs. the width of the quarter-wavelength inverter.

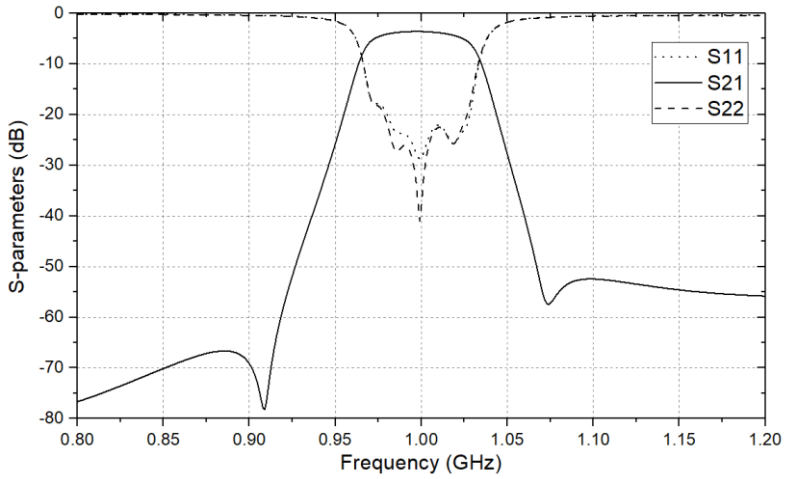

Figure 4.4 Simulated frequency response of proposed filter.

4.3 Design of Filter with Tunability

This section shows the development of a type of tunable filter based on the previous filter configuration. Filter tunability is carried out by loading variable capacitance on resonators. Characterisation of the capacitive loaded DBR is discussed below.

4.3.1 Tunable DBR Characterisation

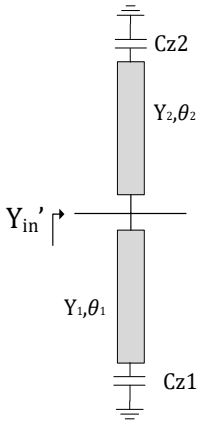

Figure 4.5 DBR with capacitive loading.

Flexible TZs and resonating can be accomplished by adding varicaps on each open stub of DBR, as shown in Figure 4.5. To characterise this DBR after capacitive loading, the input admittance equations (4.1), (4.2) of the open stubs now can be derived as

$$Y_{in1}' = Y_1 \frac{Y_{c1} + jY_1 \tan\theta_1}{Y_1 + jY_{c1} \tan\theta_1} \tag{4.5}$$

$$Y_{in2}' = Y_2 \frac{Y_{c2} + jY_2 \tan\theta_2}{Y_2 + jY_{c2} \tan\theta_2} \tag{4.6}$$

where $Y_{c1} = j\omega C_{z1}$ and $Y_{c2} = j\omega C_{z2}$ are the frequency-dependent admittances of loaded capacitors. Then, the admittance ratios of the stubs to the loaded capacitance are defined by

$$\begin{cases} k_1 = Y_1 / Y_{c1} \\ k_2 = Y_2 / Y_{c2} \end{cases} \tag{4.7}$$

The locations of transmission zeros caused by the capacitive loaded DBR now can be found by solving equations (4.8), and the transmission pole can be located by the equation (4.9).

$$\begin{cases} k_1 + j\tan\theta_1 = 0 \\ k_2 + j\tan\theta_2 = 0 \end{cases} \tag{4.8}$$

$$Y_1 \frac{1+ jk_1 tan\theta_1}{k_1 + jtan\theta_1} + Y_2 \frac{1+ jk_2 tan\theta_2}{k_2 + jtan\theta_2} = 0 \tag{4.9}$$

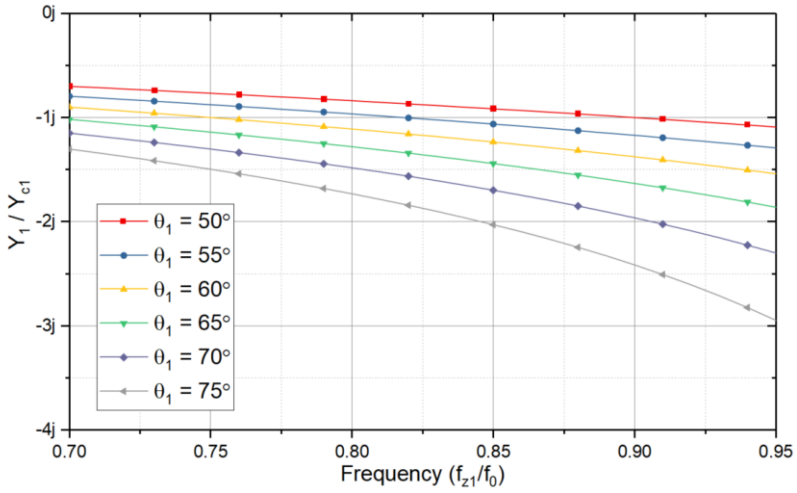

(a)

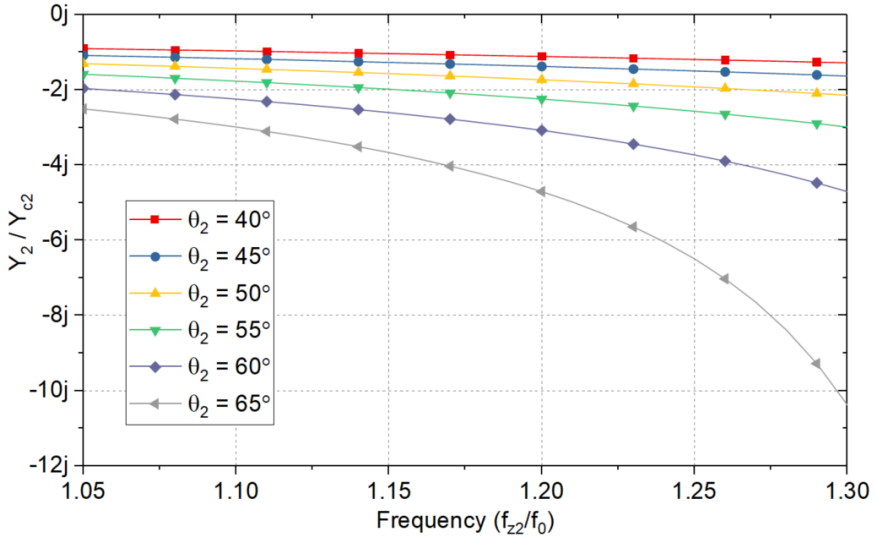

(b)

Figure 4.6 Transmission zero frequencies vs the admittances ratio between stub and loaded capacitance: (a) lower side transmission zero; (b) upper side transmission zero.

Moreover, the equation (4.9) implies that transmission zero locations are a function of the stub-lengths and the admittance ratios k_1, k_2. Figure 4.6 demonstrates the variation of transmission zero frequencies for different stub-lengths and admittance ratios. Here, all frequencies are normalised to the centre frequency f_0, and the electrical lengths θ_1 and θ_2 are also given at the filter centre frequency. Therefore, the required transmission zero frequencies and tuning range can be achieved by choosing stub-lengths and admittance ratios properly. In practice, the trade-off can be driven between fabrication-

limited line width (line admittance), line length, and the varactor diodes capacitance range.

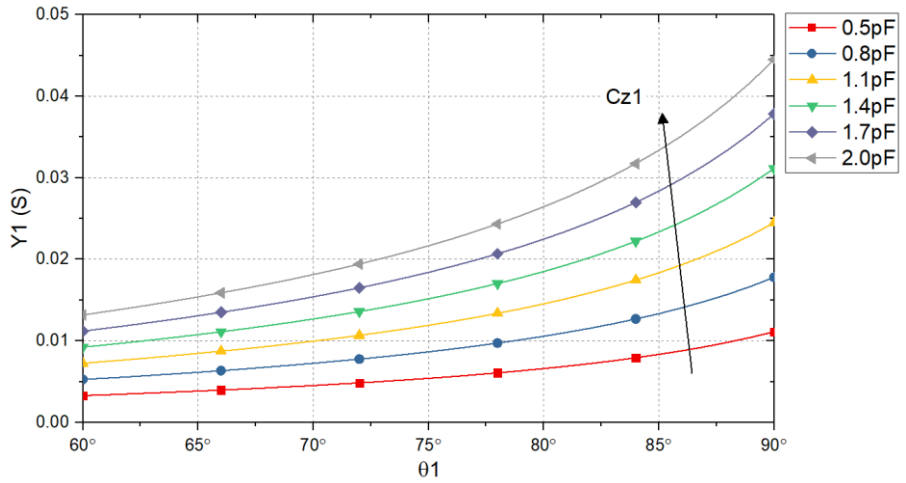

(a)

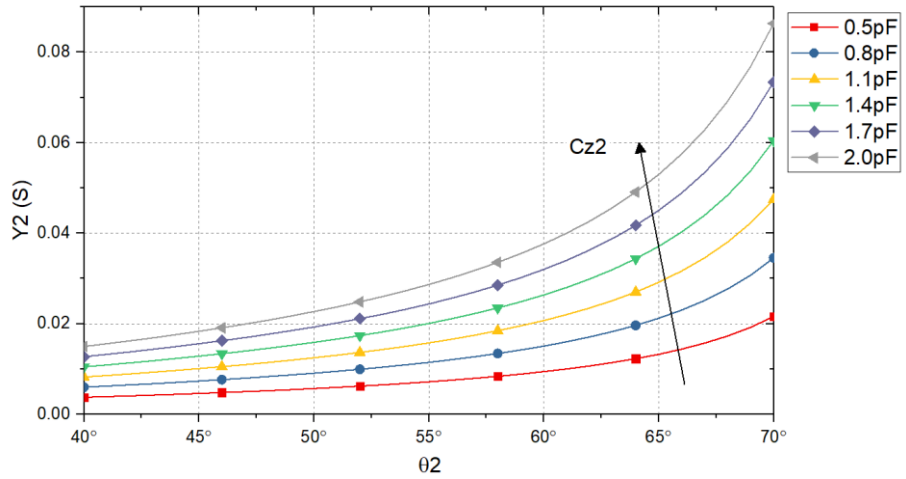

(b)

Figure 4.7 Calculated lines' length and admittance for different loading capacitances to obtain a TZ pair at $0.85f_0$ and $1.15f_0$. All electrical lengths are given at f_0.

To demonstrate the trade-off for achieving the desired allocation for two transmission zeros, we assume that two transmission zeros are allocated at 0.85 GHz and 1.15 GHz, and the filter frequency is centred at 1 GHz. For wanted transmission zeros frequencies, the stub-admittances and lengths with different loading capacitances are presented in Figure 4.7 by using (4.7), (4.8) and (4.9). In such a manner, appropriate design parameters can be decided for an initial state of the tunable filter depending on the practical requirements.

4.3.2 Tunable Filter Layout and Measurements

Based on previous discussions, Figure 4.8 shows a 5-pole filter designed at 1 GHz with bandwidth tunability. The filter has an overall size of $\sim 35\,mm \times 40\,mm$. Capacitances C_{cq}, C_{c1} and C_{c2} control couplings between each resonator for the bandwidth reconfigurable. Frequency tuning capacitance C_{r1}, C_{r2}, C_{z1}, and C_{z2} are loaded at open ends of each resonator for resonating frequencies adjustment when the bandwidth is changed. As the previous discussion on Figure 4.3(b), the coupling coefficient between the DBR and adjacent resonator can be changed by adjusting the fractional bandwidth of the transmission-zero pair. Thus, for a design with less restriction on selectivity, a fix capacitance or quarter-wavelength invertor could be used to replace C_{c2} for same bandwidth tunability that a controlling DC voltage can be reduced.

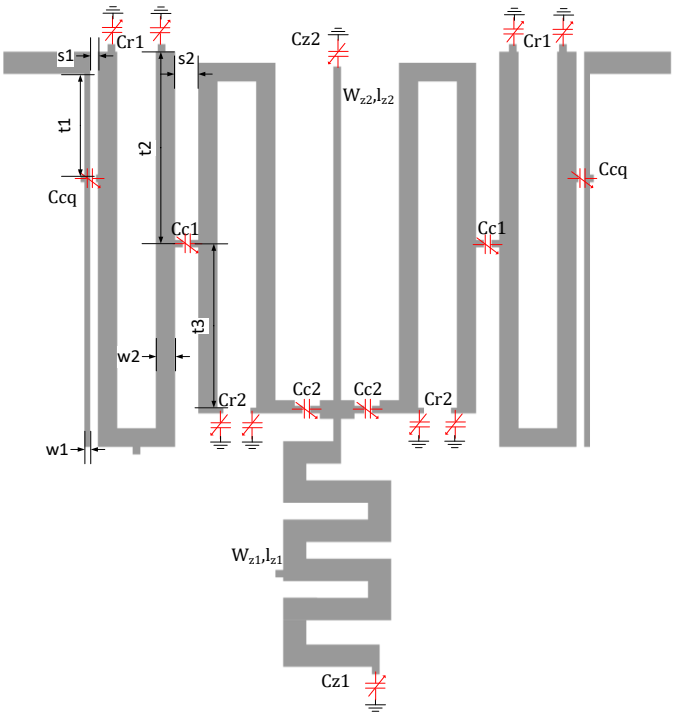

w_1	w_2	t_1	t_2	s_1	s_2	l_{z1}	w_{z1}	l_{z2}	w_{z2}
0.3	1	5.4	8.9	0.4	1.2	33.5	1.2	18	0.4

Figure 4.8 Layout and dimension parameters of the tunable filter with dual-behaviour resonator, unit: *mm*.

Dimension parameters of the proposed filter are given in Figure 4.8 with the layout. The filter was manufactured on the same substrate RT/Duroid 6010 as the previous one. The photograph of the fabricated filter is presented in Figure 4.9. The filter employs two types of varactor diodes: high-Q diodes MA46H120 ($0.2 - 1.1\ pF, R_s = 0.88\ \Omega$) for C_r, C_{z2} and relative low-Q diodes SMV2019-040LF ($0.3 - 2.2\ pF, R_s = 4.8\ \Omega$) for C_c, C_{z1}. A total number of 16 varactor diodes are applied in the circuit. The 100 $k\Omega$ resistors and 47 pF capacitors construct the DC bias circuit for varactor diodes. The full bandwidth reconfiguration is controlled by 7 DC bias voltages.

Figure 4.9 Fabrication of the tunable filter

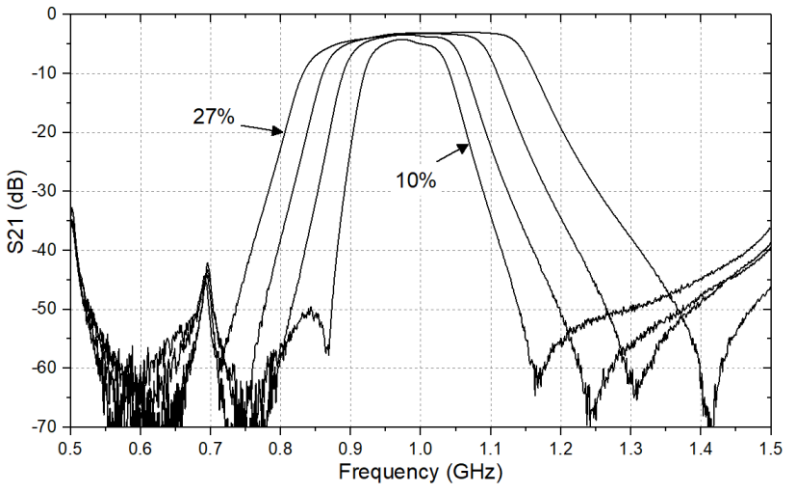

(a)

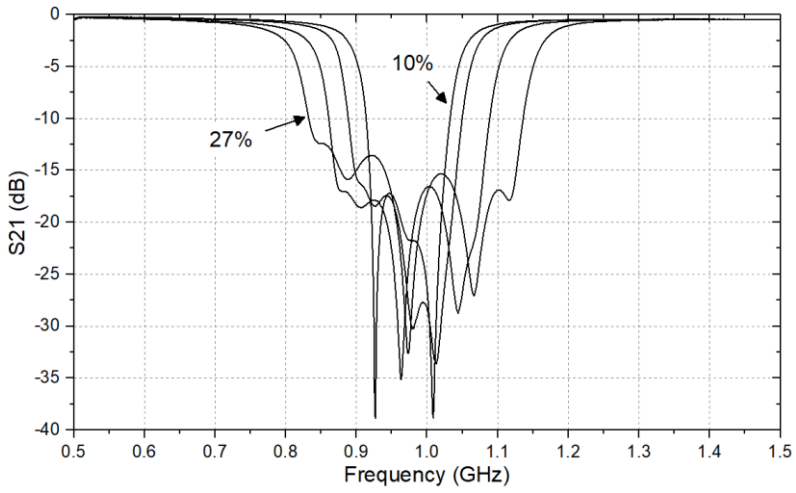

(b)

Figure 4.10 Bandwidth tuning of the fabricated filter. (a) Insertion loss; (b) Return loss.

The measurement responses of the filter are presented in Figure 4.10 where the filter fractional bandwidth is tuned from 10% to 27%. The passband frequency is centred at 0.97 GHz instead of 1 GHz due to the dielectric constant error. The transmission zeros are moving with the bandwidth tuning keeping the selectivity of the passband. Additionally, the filter also shows a slight tunability on the centre frequency in Figure 4.11 where the centre frequency varies from 0.95 GHz to 1.08 GHz with a constant absolute bandwidth of 200 MHz. It should be noticed that, along with the bandwidth tuning and the frequency tuning, the locations of transmission zeros were not able to maintain a constant frequency distance to the passband due to the limited capacitance ranges of C_{r2} and C_{c2}. In order to obtain a constant selectivity enhancement for the filter in the future, varactors with a large capacitance tuning range could be applied in the design. Besides, because of the loss of the microstrip and varactors, the insertion loss of the filter reaches 4.5 dB at the bandwidth state of 10%, and the in-band variation is 3.5 dB. The effects of loss will become more pronounced if the bandwidth is narrower. In the next section, a novel lossy method is proposed to achieve passband flattening for tunable filter applications.

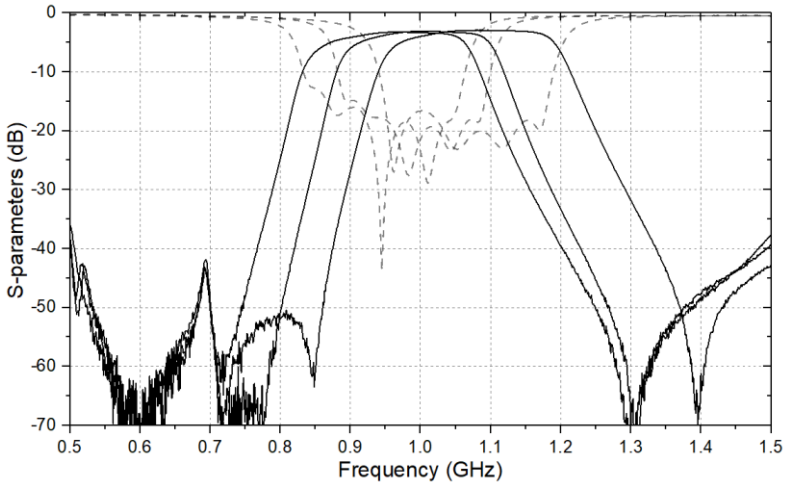

Figure 4.11 Frequency tuning of the measured filter

4.4 Centre-Loaded Resistive Loading (CLRCCs)

4.4.1 CLRCCs Lossy Topology Concept

The principle of the lossy filter deliberately distributes more losses in the mid-band so that the round-off passband edges will be sharpened leading to a good flatness along the entire passband. For an inline filter structure, the RCCs technique is a common method for the lossy responses as shown in Figure 4.12 [4]. Resistors are coupled to non-adjacent resonators through extra $\lambda/4$ lines. However, in most cases of tunable planar filter design, for example, in Figure 4.8, open ends of resonators are loaded with varactor circuits which makes the implementation of conventional RCCs difficult.

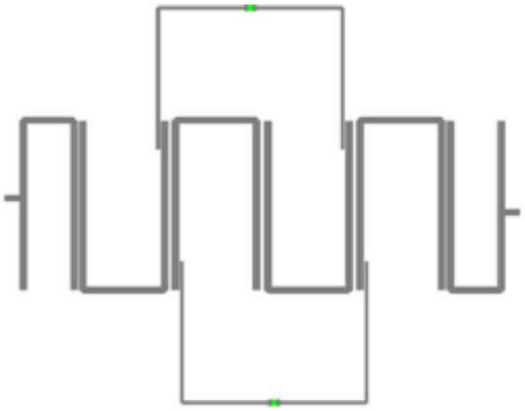

(a)

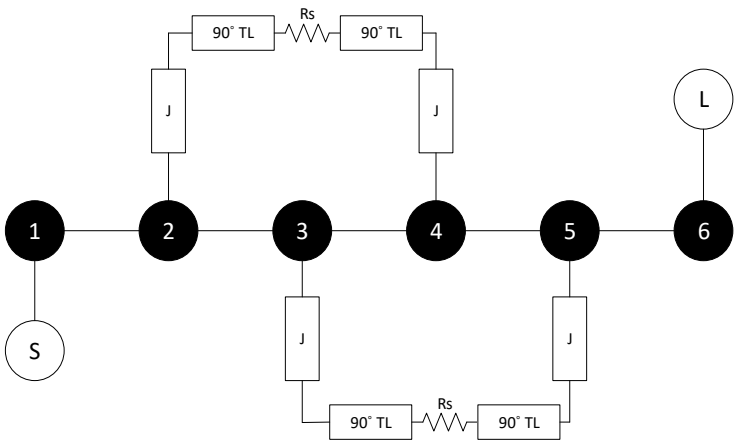

(b)

Figure 4.12 (a) Conventional resistive cross-coupling in an inline structure filter [4]; (b) Corresponding coupling topology.

In this regard, a new type of centre-loaded RCCs (CLRCCs) structure is introduced in Figure 4.13 (a). As showing, a resistor connects the middle of two resonators. According to the concept of dual-mode resonator analysis in Chapter 3, the loaded components in the middle of an open-loop microstrip resonator are de-coupled from the odd mode of the resonator. Since the odd mode is the fundamental mode of the open-loop resonator, there is no coupling between the resistor and the loaded resonator. Instead, when the even mode symmetrical plane presenting at the loading position, such loading configuration can be treated as a coupling path from the adjacent nodes to the resistor through a 90° transmission line (the path length along half resonator). Therefore, for the loading between the i^{th} and j^{th} nodes, the actual RCCs paths are between the adjacent nodes $i-1$, $i+1$ and nodes $j-1$, $j+1$, as shown in figure 4.13 (b). In such a manner, the RCCs can be achieved without conflicting with varactor circuits. Note that, because the even mode has a symmetric field distribution which lead to an additional 180° phase comparing the odd mode, the couplings from previous nodes to RCC line and from RCC line to the next nodes have the same magnitude, but opposite signs.

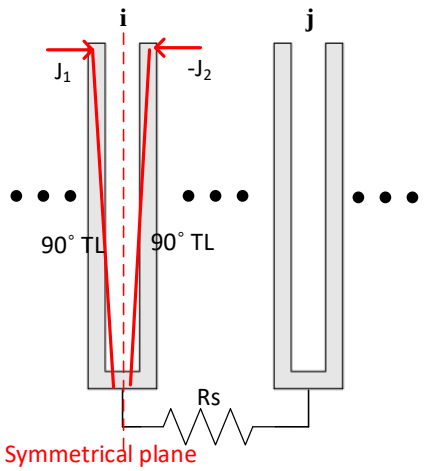

(a)

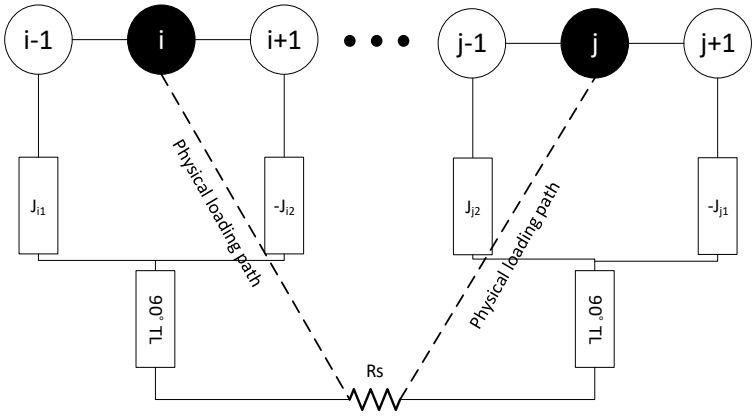

(b)

Figure 4.13 (a) CLRCCs loading structure; (b) Corresponding coupling topology of the CLRCCs.

4.4.2 Inline Filters with CLRCCs

4.4.2.1 Initial Design: 5-pole Microstrip Filter

For our investigation, an initial 5-pole hairpin microstrip filter has been designed at 1.98GHz with 4.4% fractional bandwidth as in Figure 4.14 (a). The filter is based on the substrate RO3003 having a thickness of 0.51 *mm*. The substrate permittivity is 3 and its loss tangent is $\tan\delta = 0.0013$. The full-wave EM simulation responses are given in Figure 4.14 (b). The insertion loss of the filter at its centre frequency is found to be 3.7 dB. Consequently, the unloaded quality-factor of the filter resonator can be estimated by equation (2.28) as 150. The simulated filter response shows an in-band insertion-loss variation of 2.3 dB.

(a)

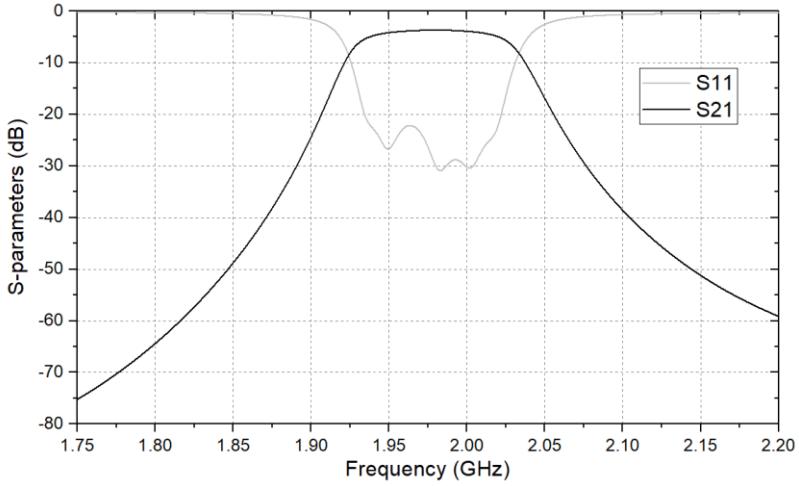

(b)

Figure 4.14 (a) Layout of the classical 5-pole inline filter; (b) Frequency response of the filter.

4.4.2.2 CLRCC Effect on Filter Passband

To investigate the lossy effect when resistors are connected between different resonators, Figure 4.15 (a) shows the indication of the connection on the filter layout, and a set of in-band frequency responses is shown in Figure 4.15 (b) for the CLRCC loaded between different resonators. The frequency responses are obtained by the co-simulation of Sonnet and AWR microwave office. All CLRCC are symmetrically deployed with a directly loaded resistance of 40 Ω. Generally, as can be seen in figure 4.15 (b), R1-R4 (resonator 1 to resonator 4) and R2-R5 CLRCC have more insertion loss produced at the lower part of the passband rather than the upper one. In the meantime, the in-band absorptions for the cases of [R1-R2, R4-R5], [R1-R3, R3-R5], and [R2-R3, R3-R4] are closer to the upper side of the passband with different magnitudes. For the filter with asymmetrical passband distortion as [5], appropriate loading topology could be adapted for the desired in-band absorption. Furthermore, when the resistor is loaded between R1 and R5, the absorption occurs at two edges of

passband degenerating the passband flatness of the filter. For a low-Q filter which has maximum power transmission at the middle of the passband and equal passband decay at two edges (see Figure 4.14 (b)), the CLRCC between R2 and R4 (the red curve in Figure 4.15 (b)) is preferred for passband flattening. Figure 4.15 (c) shows the full view of the frequency responses of all CLRCC topologies. One can observe a reduction in the selectivity of the filter after CLRCCs presenting because of the overall resonator-Q of the filter is lower [4].

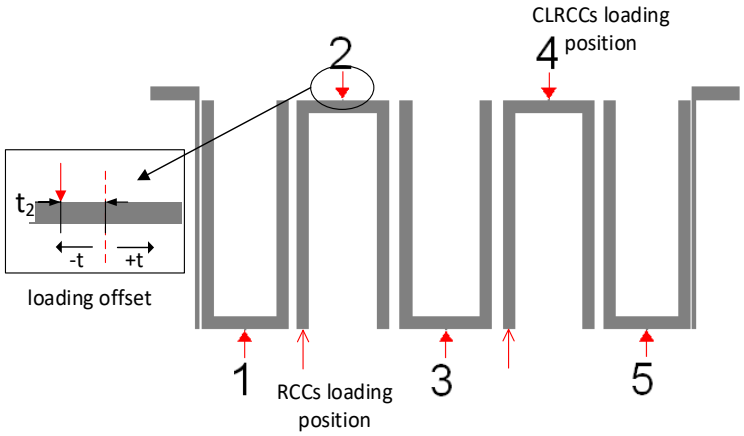

(a)

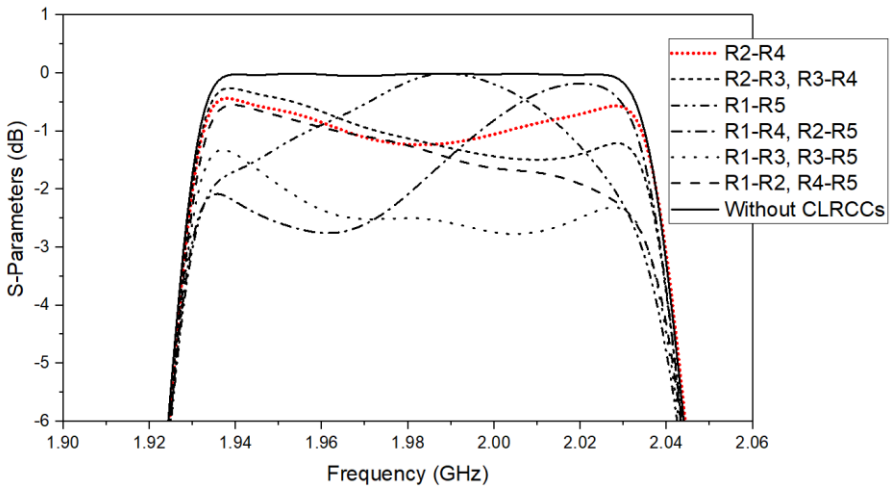

(b)

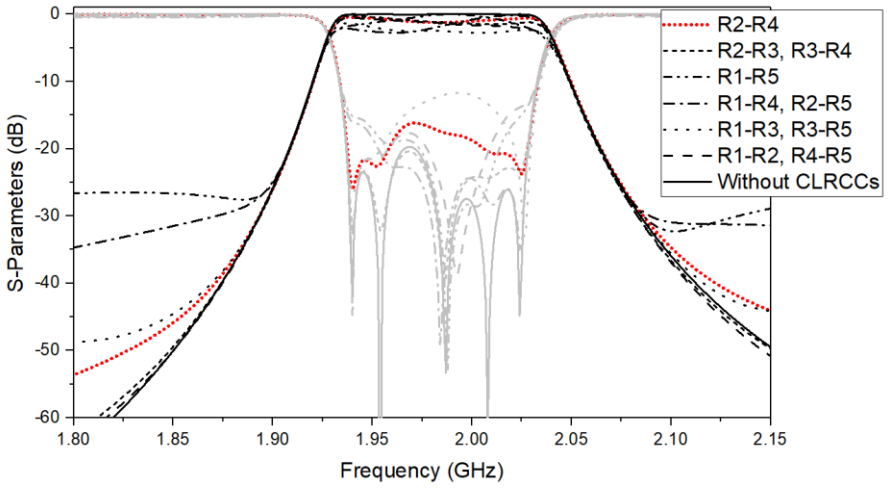

(c)

Figure 4.15 The effect of CLRCCs for loading between different resonators with the loading position indication; (a) CLRCCs loading layout; (b) Insertion loss variation caused by CLRCCs in the passband; (c) Full views of frequency responses.

A further study has been made to identify the effect of CLRCC loading position on the same resonators. An offset for the tapping position apart from the middle of the resonator can cause the frequency shifting of the absorption. Figure 4.16 (a) shows the frequency responses of the R2-R4 CLRCC with the tapping offsets of t_2 and t_4, and the initial state ($t_2, t_4 = 0\ mm$) is given for comparison. In an aspect of passband insertion loss, when the tapping position varies oppositely as $t_2 = -1\ mm, t_4 = +1\ mm$ and $t_2 = +1\ mm, t_4 = -1\ mm$, the passband slopes toward one side of the edge, as dot and dash-dot lines in Figure 4.16 (a). When the tapping positions move toward the same direction as $t_2 = +1\ mm, t_4 = +1\ mm$, the dashed line in Figure 4.16 (a) shows an absorption in the middle band. This response looks like the effect of the initial state but with a different loading resistance. To distinguish those lossy effects, we further shift the tapping position to $t_2, t_4 = 4.3\ mm$ while adjusting the loading resistance of the normal case $t_2, t_4 = 0\ mm$ to match the insertion loss to the offset one at the centre frequency, shown in Figure 4.16 (b). As can be seen, the tapping at the middle of the resonator produces absorption concentrating at the centre of the passband comparing the offset case. Notably, this conclusion only stands for the CLRCC connecting from R2 to R4. In practice, one can use different resistive cross-coupling loading configurations based on a specific filter lossy requirement to achieve a flattened passband.

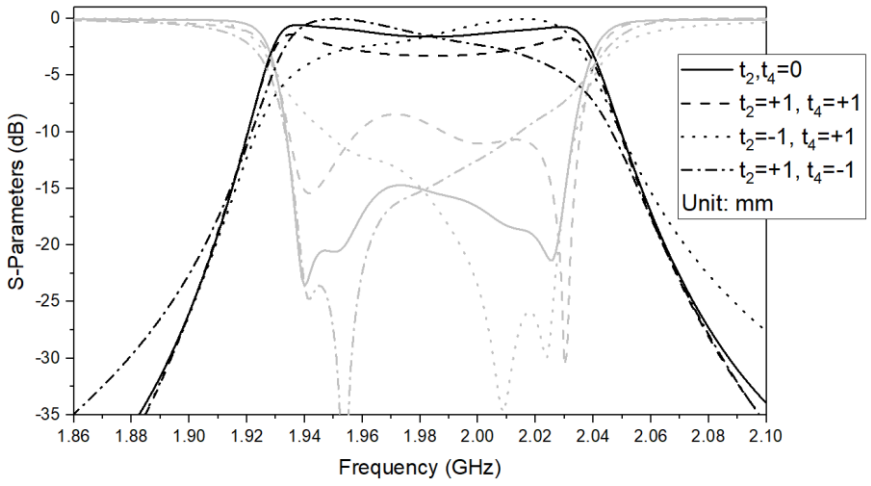

(a)

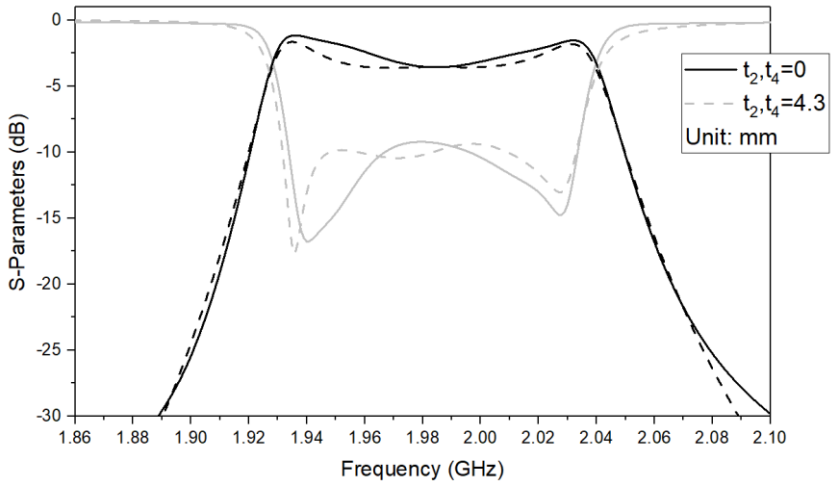

(b)

Figure 4.16 (a) Frequency responses for the offset of the CLRCC tapping position; (b) Comparison for the middle loading and the offset loading.

Instead of direct loading resistances between resonators, 180° extended lines are usually required to connect the lumped resistors in practice to keep the inline-filter configuration. To understand the impact of the extended line on the filter responses, Figure 4.17 shows the filter S-parameters when a loading resistance of 10 Ω is with different line impedances of the half-wavelength transmission lines. We can find that lower impedance produces more insertion loss at the passband edges while the S21 at the centre frequency remains the same. Therefore, to effectively eliminate the round-edge effect of a high loss filter, narrow lines (high impedance) are preferred for resistor connection because there is less compression at passband edges.

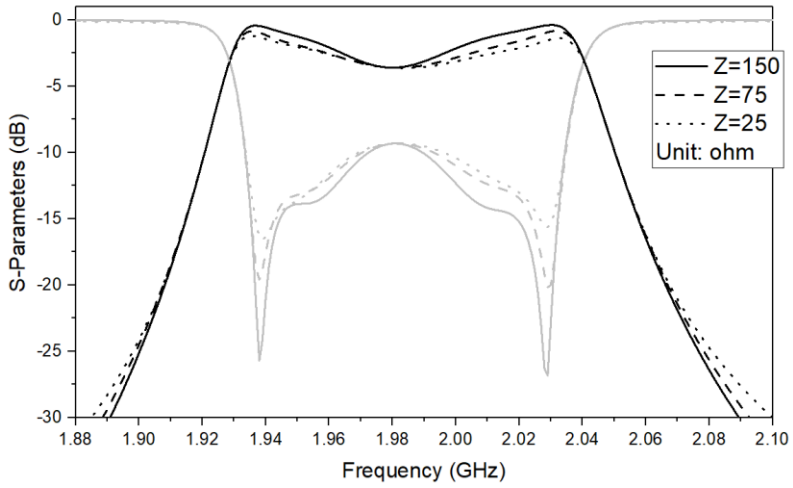

Figure 4.17 Simulated frequency responses for the 5-pole lossy filter with different line impedances.

4.4.2.3 Design Examples and Measurements

To demonstrate the implement of centre-loaded resistive cross-coupling in inline lossy filter designs, a five-pole filter and a six-pole filter are designed and measured with CLRCCs for passband flattening respectively in Figure 4.18. Filters are fabricated on the same substrate RO3003 as the reference filter in the previous part. Half-wavelength lines for CLRCCs with a line width of 0.3 *mm* are meandered for a compact size.

Shown in Figure 4.19 (a), the intrinsic in-band insertion loss variation of the fabricated 5-pole filter can be found as 1.5 dB. After a CLRCC resistance of 30 Ω is applied for the passband flattening, the lossy filter presents a passband flatness of 1 dB at a cost of additional mid-band insertion loss of 0.65 dB (S_{21} = -3.82 dB). In Figure 4.19 (b), measurements of the 6-pole lossy filter with a bandwidth of 4.4% at 1.98 GHz are also given with a comparison to the filter responses without CLRCCs. Passband flatness has been effectively improved from 1.95 dB to 0.88 dB with a mid-band insertion loss of 5.35 dB.

(a) (b)

Figure 4.18 Layout of lossy filter implemented as (a) 5 in-line coupled hairpin resonators and (b) 6 in-line coupled hairpin resonators.

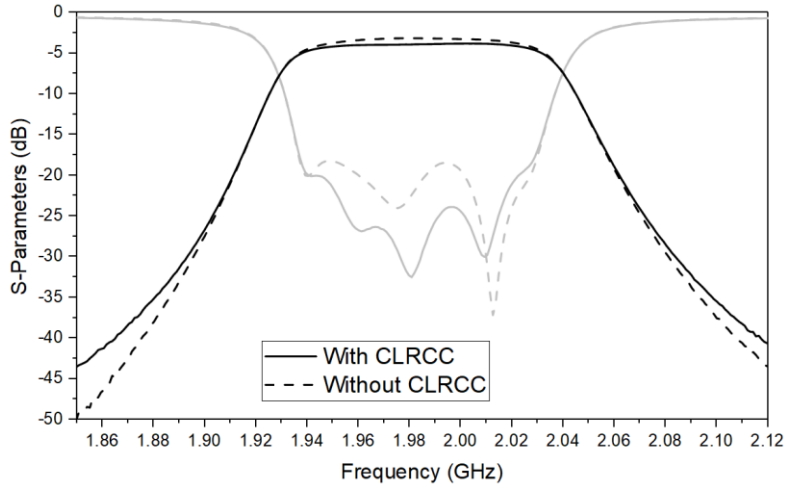

(a)

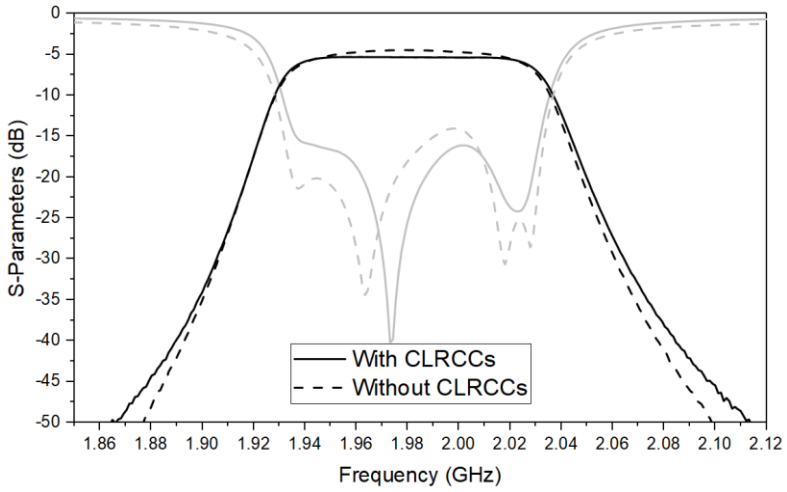

(b)

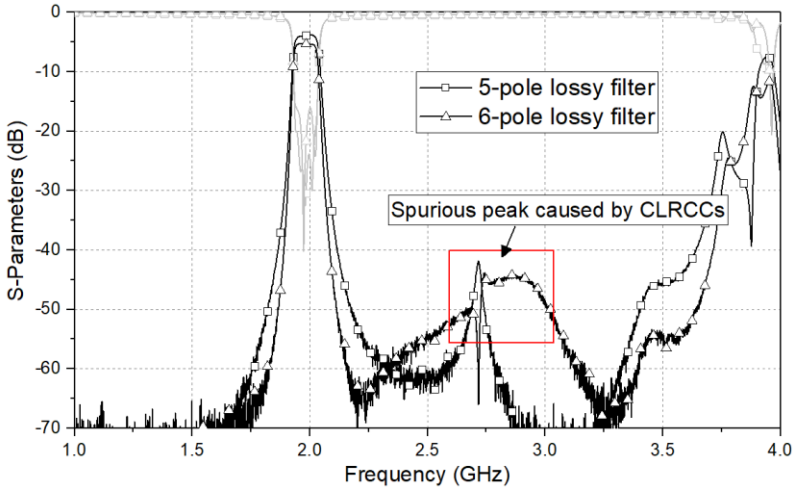

(c)

Figure 4.19 Measured results for lossy filters with CLRCCs, (a) 5-pole filter; (b) 6-pole filter; (c) Wideband responses for two lossy filters.

In addition, performances of two fabricated lossy filters on a wide frequency band are displayed in Figure 4.19 (c). Notably, Spurious peaks around 2.75GHz caused by the 180° extended lines can be observed with more than 40 dB suppression.

4.5 Tunable Filter with Selectivity and Lossy Improvement

A combination of bandwidth tunable filter with DBR and centre-loaded resistive cross-coupling is presented in this section to demonstrate the passband flatness improvement for the bandwidth tuned filter.

4.5.1 Lossy Configuration and Equivalent Circuit

In Sections 4.3 & 4.4, a 5-pole filter with DBR and its tunable form have been discussed. For the lossy case, different from the arrangement for the 5-pole filter in Section 4.4, a resistor is now deployed between the first and the last nodes of the filter for passband flattening instead of nodes 2 and 4. This alteration is because of the opposite signs of the coupling coefficients between the DBR node and its adjacent resonators, as in Figure 4.20. Using the equivalent circuit synthesis method presented in Chapter 2, the associating equivalent circuit of this type can be found in Figure 4.20 (a). The invertors J_{c1}, J_{c2} represent the coupling between the CLRCCs path and the adjacent resonators.

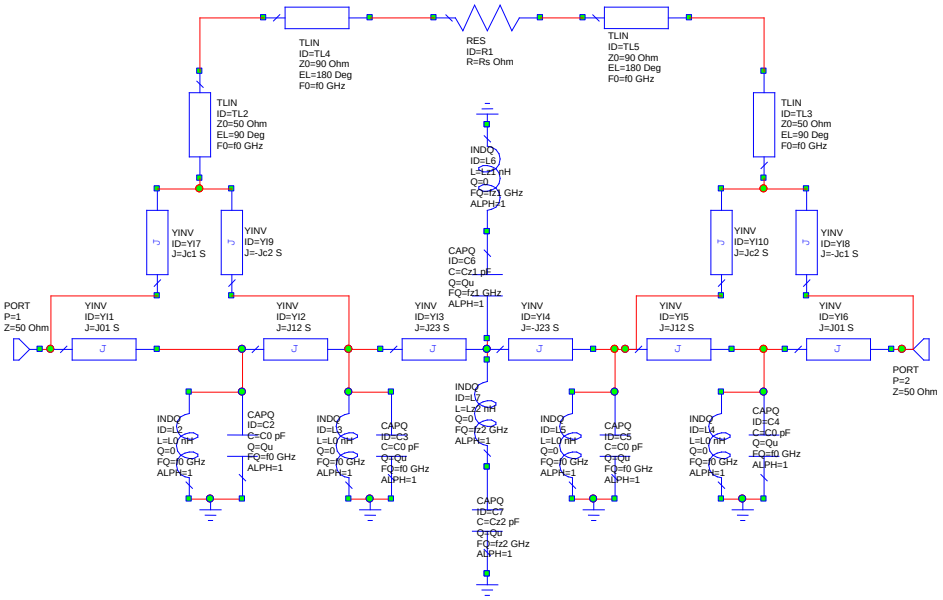

(a)

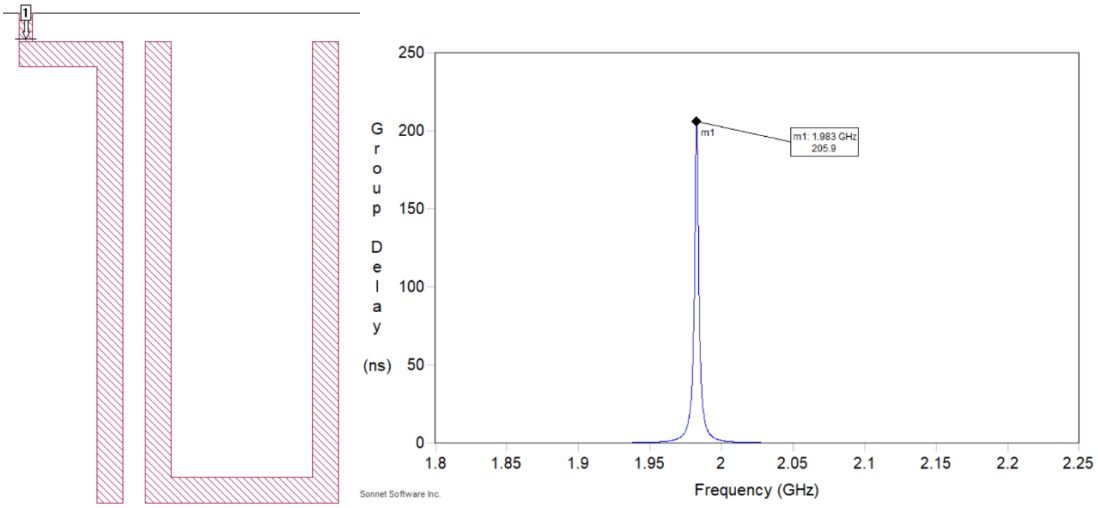

(b) (c)

Figure 4.20. (a) Equivalent circuit of the tunable filter with CLRCCs; (b) Example extraction configuration; (c) Group delay of S_{11}.

The values of the inverters J_{c1}, J_{c2} can be estimated by extracting the external Q at the connection position of the resistor. An example configuration of the extraction is given in Figure 4.20 (b). Thus, Q_e can be calculated by the group delay of S_{11} in Figure 4.20 (c). The invertors parameters J_c

$$J_c = \sqrt{\frac{b_1 Y_0}{Q_e}} \tag{4.10}$$

where b_1 is the slope parameter of the resonator, Y_0 is the terminal admittance (0.02 S).

Figure 4.21 demonstrates the frequency responses of the equivalent coupling network in improving the round passband edges. The filter round-edge passband could be flattened with a properly loaded resistance while the return loss is maintained. However, this also leads to a poorer stopband rejection level because of the resistive coupling between source and load. The source-to-load RCC also leads to two transmission zeros approaching passband edges. But the band edges' slope remains the same.

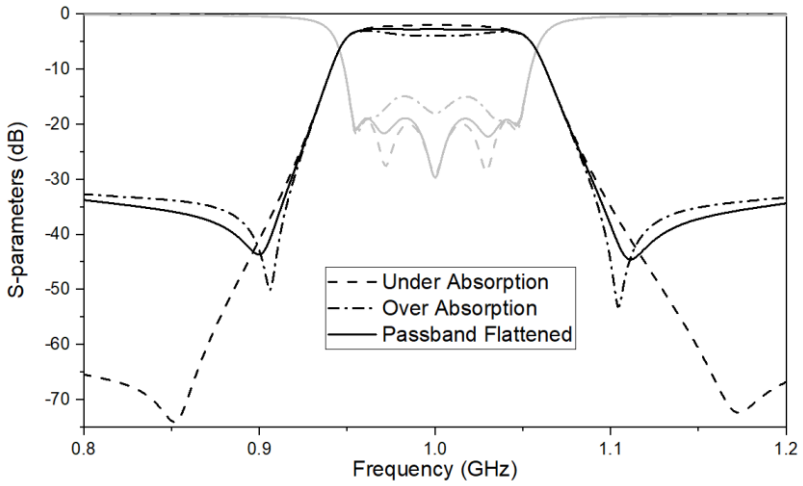

Figure 4.21 . Frequency responses of the equivalent circuit.

4.5.2 Filter Design and Fabrications

The proposed tunable lossy filter has been designed at 1 GHz and on the substrate RT/Duroid 6010 with a thickness of 1.27 *mm*, and the layout of the filter is shown in Figure 4.22 (a). The varactor MA46H120 ($C_t = 0.2 - 1.1\ pF, R_s = 0.88\ \Omega$) is used for all variable capacitance in the filter. The C_{z1} is composed of two varactors in parallel for a wider variation range (0.4 – 2.2 pF). For a symmetrical TZs pair at widest bandwidth state, the DBR has stub-lengths $l_1 = 25\ mm$ and $l_2 = 22.8\ mm$ while the widths w_1 and w_2 are 1.8 *mm* and 0.4 *mm*. Fixed capacitors C_{c2} with a capacitance of 3 pF are placed instead of varactor to reduce the number of DC suppliers as discussed before. The filter has an overall size of $45\ mm \times 64\ mm$.

Since the round edge phenomenon exacerbates at narrow bandwidth states, a variable

resistor is preferred to maintain a good passband flatness during the bandwidth reconfiguration. Therefore, this variable resistor is fulfilled with an attenuation diode SKYWORKS-SMP1307 which could provide an adjustable resistance ranging from 5 Ω to 2500 Ω. The 100 $k\Omega$ RF block resistors, 33 nH RF-choke inductors, and 47 nF DC block capacitor are applied for the biasing networks. The picture of the fabricated filter is shown in Figure 4.22 (b). In this case, 7 DC bias voltages with a range of 0 V to 20 V are required for bandwidth reconfiguration and the attenuator controlling.

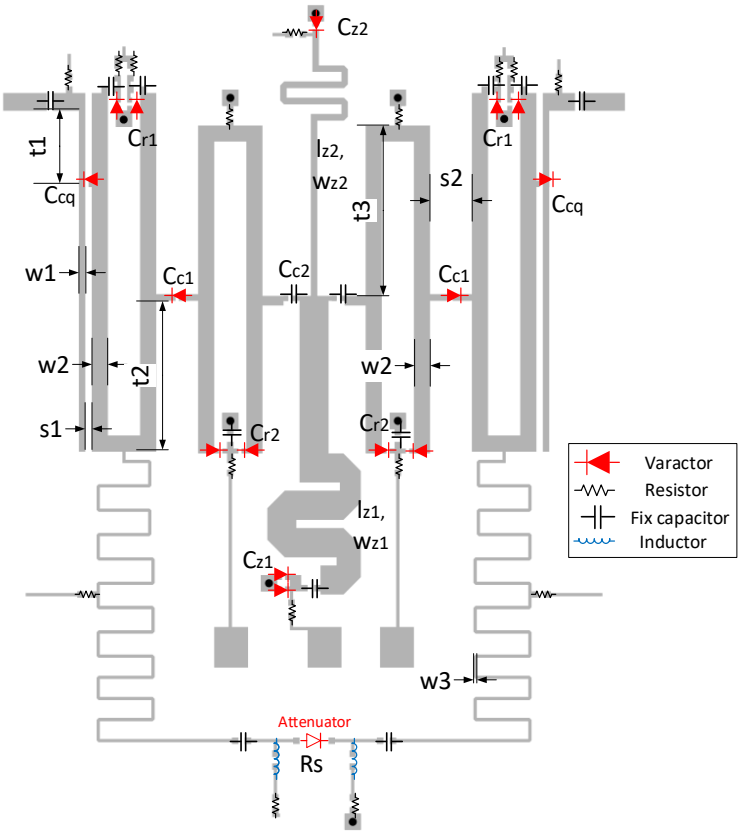

w_1	w_2	w_3	t_1	t_2	t_3	s_1	s_2
0.4	1	0.2	4.5	9.3	10.5	0.4	2.6
l_{z1}	w_{z1}	l_{z2}	w_{z2}	C_{c2}			
25	1.8	22.8	0.4	3 pF			

(a)

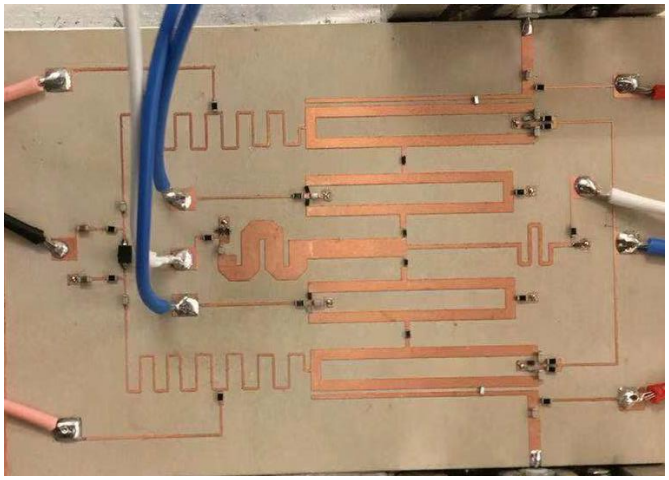

(b)

Figure 4.22. (a) The final layout of the proposed tunable lossy filter with DC biasing circuit. (Unit: *mm*) (b) Photograph of the fabricated filter.

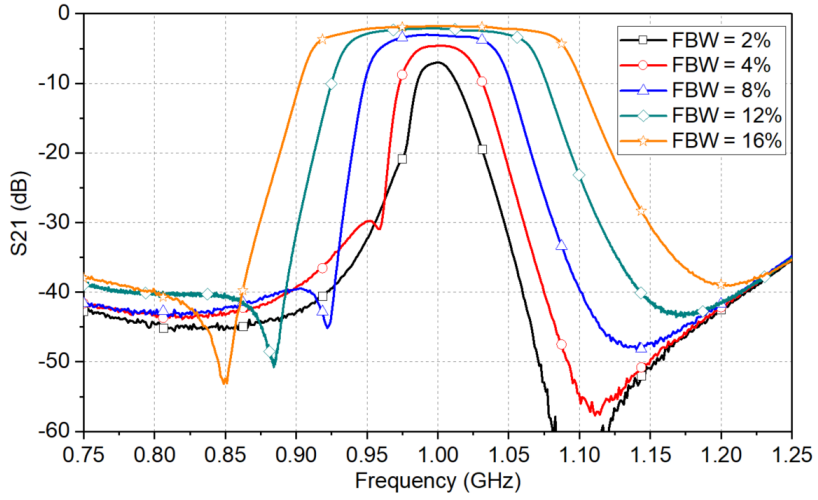

(a)

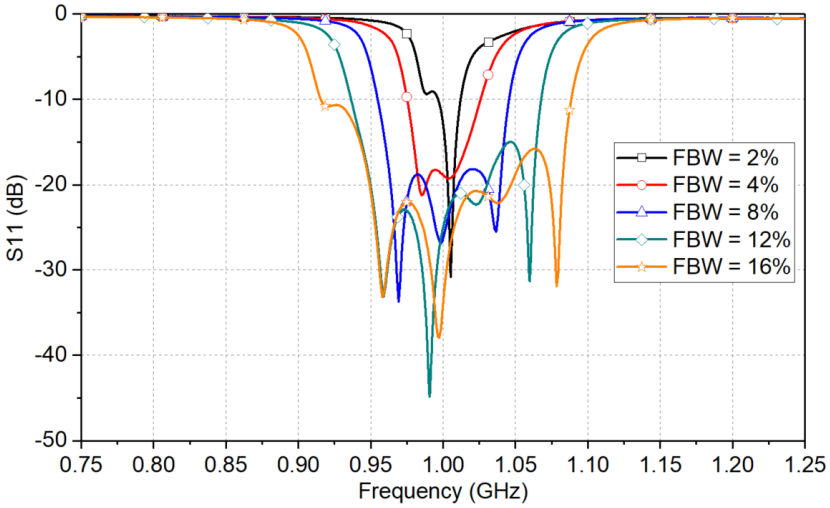

(b)

Figure 4.23 Frequency responses of the fabricated tunable filter without CLRCC, (a)

S21; (b) S11.

At first, Figure 4.23 shows the measured filter responses without CLRCC applied. The tuned bandwidth from the widest state to the narrowest state is listed as 160 MHz (16%), 120 MHz (12%), 80 MHz (8%), 40 MHz (4%), and 20 MHz (2%), centred at 1 GHz. At the band state of 16%, transmission zeros are located at 0.85 GHz and 1.2 GHz. When the filter changes to the narrow-bandwidth state, the selective of the passband becomes better as transmission zeros move closer to the passband. Meanwhile, the locations of two TZs become asymmetrical due to the admittance of the capacitor varies for the tuning. Moreover, the out-band rejection level of greater than 30 dB is preserved for all bandwidth states.

After the presenting of CLRCC, Figure 4.24 (a) depicts the improvement in passband flatness for the 8% fractional bandwidth state. The filter at this state presents an insertion loss variation of 0.08 dB, 0.12 dB, 1.01 dB within the frequency range of $f_0 \pm 10$, $f_0 \pm 25$ and $f_0 \pm 40$ MHz, respectively. The shape of the measured response is equivalent to a conventional filter with a uniform unloaded Q of 320. The in-band return loss is maintained below 14 dB. Aside from the in-band responses, as described in Figure 4.24 (b), band-side transmission zeros are moving toward the passband slightly because of the resistive coupling between the source and the load. Meanwhile, the out-band rejection has a degeneration, but the passband edge slope is unchanged because of TZs.

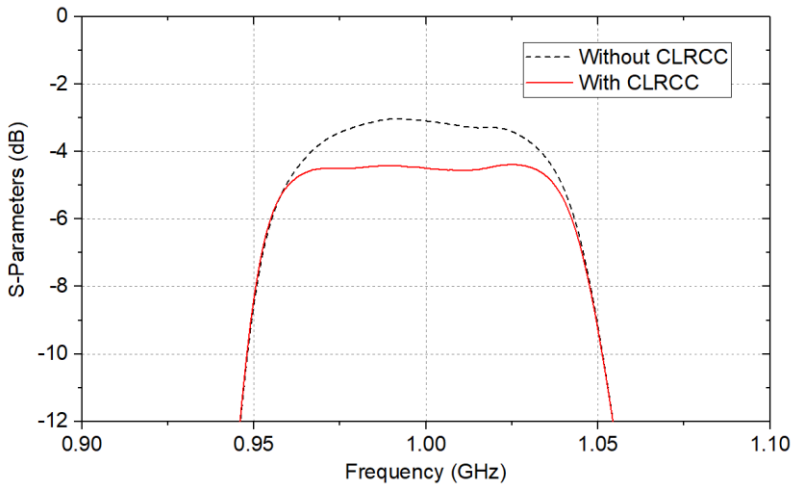

(a)

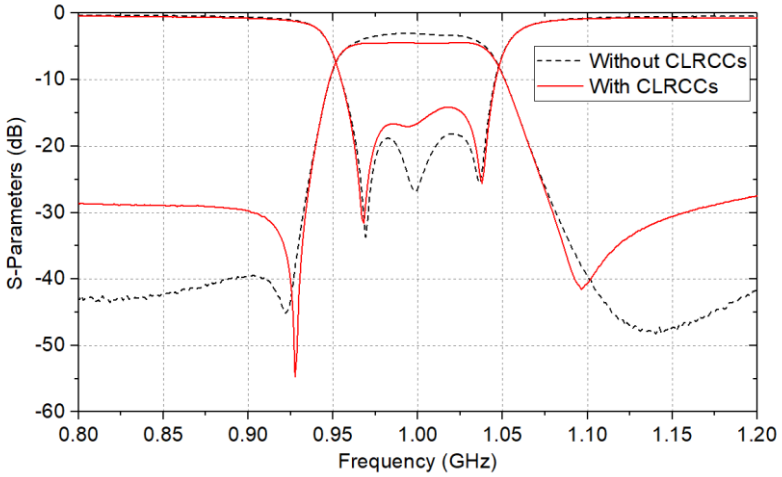

(b)

Figure 4.24. (a) Comparative responses with and without the proposed CLRCCs for the filter at the 8% FBW state; (b) The full view of the frequency responses.

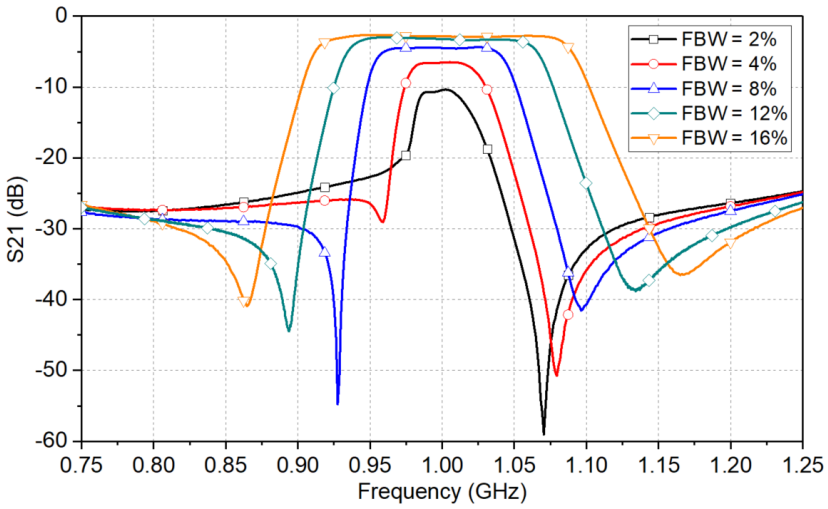

(a)

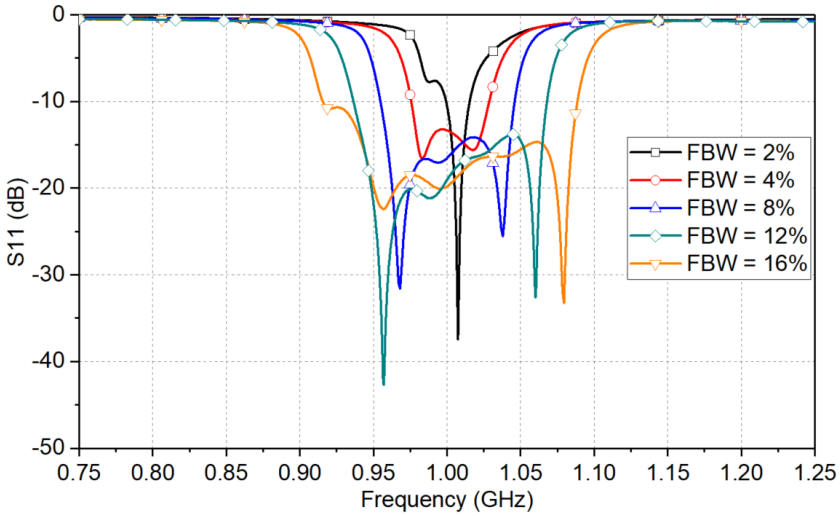

(b)

Figure 4.25 Measured frequency response of the lossy tunable filter. (a) S21; (b) S11.

Figure 4.25 shows the tunable lossy filter responses from the 2% state to the 16% state. The passband return loss remains below 10 dB except for 2% fractional bandwidth state, due to the matching adjustment for compensating the fabrication and dielectric constant error. In the aspect of passband flatness, the filters present an improved in-band variation during the tuning. To demonstrate this improvement for all of the bandwidth states, Figure 4.26 shows the comparison of the passband insertion-loss variation between filters with and without the centre-loaded resistive cross-coupling. As can be seen, the filter in-band insertion-loss variation is maintained within 1 dB during the bandwidth tuning. Especially, when the bandwidth is 20 MHz (2%), the implemented tunable CLRCC still functions well in flattening in-band insertion loss. Such reliable performance is rare in current publications on low-Q tunable planar filters. Moreover, a proper rejection level of greater than 25 dB is preserved for all bandwidth states. Table 4-1 gives a performance comparison with related works in the literature.

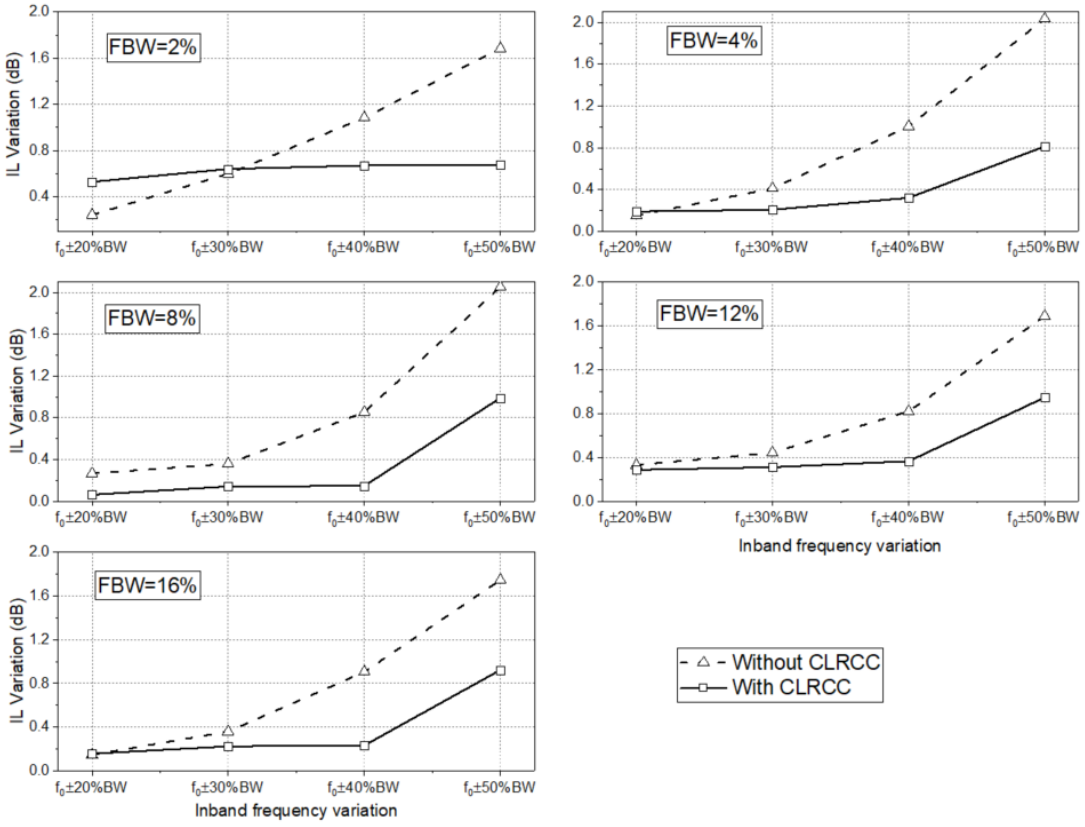

Figure 4.26 The improvement in the passband flatness for different bandwidth states by the proposed CLRCC lossy method, the insertion loss variation vs the frequency range in the passband

Table 4-1
Comparison between the proposed filter with other related works

Ref.	Order	Lossy techniques	f_0(GHz)/FBW	In-band variation (dB)	TZs	Tunable
[6]	6	Nonuniform Q and RCCs	0.96 / 6.2%	≈0.85	Yes	No
[5]	6	RCCs	1 / 25%	1.3	Yes	No
[4]	6	RCCs	3.8 / 21%	0.7	No	No
		Nonuniform Q			No	No
[1]	6	Pre-distortion	1 / 3.6%-50%	1	Yes	Yes
[7]	4	Nonuniform Q	1.6 / 10%-20%	0.7	Yes	Yes
This work	5	CLRCCs	1 / 2% - 16%	1	Yes	Yes

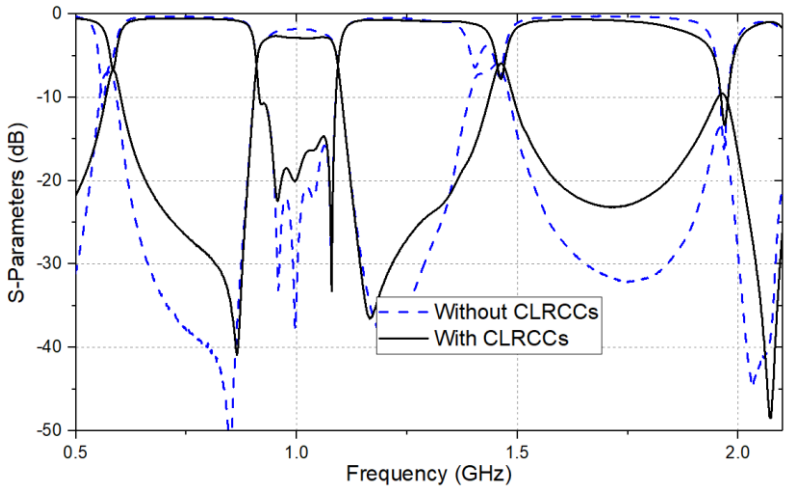

Figure 4.27 Wideband responses of the tunable lossy filter, FBW=16%.

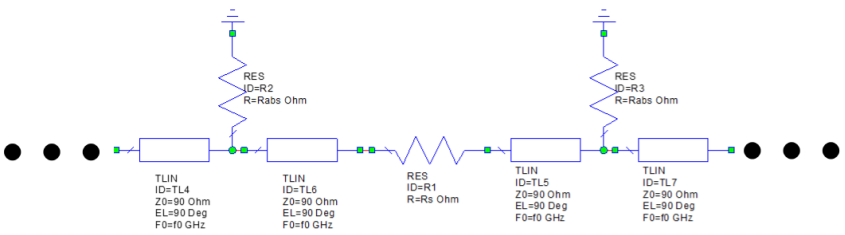

(a)

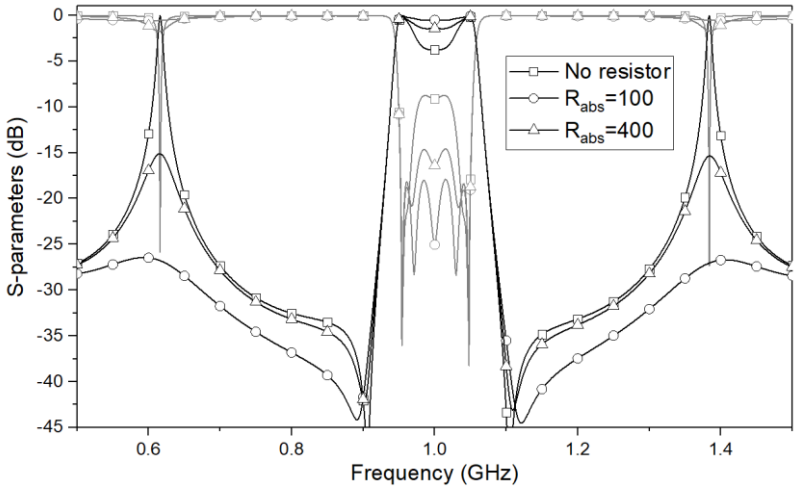

(b)

Figure 4.28 (a) Resistors in shunt; (b) Wideband frequency responses for different resistances.

Finally, the wideband responses of the fabricated filter at 16% FBW state are plotted in Figure 4.27. Two spurious peaks at frequencies of 0.59 GHz and 1.457 GHz are unaltered when the bandwidth is varied. Such spurious peaks are caused by two 180° transmission-lines in the CLRCCs circuit. To suppress those spurious peaks, additional resistors (R_{abs}) can be shunted at the halfway of two 180° TLs as illustrated in Figure 4.28 (a). Equivalent circuit simulation is employed to show the spurious peaks suppression as given in Figure 4.28 (b). Filter wideband responses are compared for different shunted resistances. It can be seen that spurious peaks can be effectively suppressed below -25 dB by a shunted resistance $R_{abs} = 100\ \Omega$. However, the in-band absorption of CLRCCs decays as the spurious peaks are suppressed. A proper resistance can be determined between passband flattening and spurious-peak suppression.

4.6 Conclusion

A high selective bandpass filter is reported with bandwidth tunability and passband flatness enhancement. A hybrid-structure consist of hairpin resonators and DBR is developed for independent controlled transmission zero. A novel lossy technique named CLRCCs is developed for adapting tunable circuit structure and efficiently improving the passband flatness of the tuned passband. Five-pole filters of this type are

examined and demonstrated. The measured filter has a bandwidth tuning capability from 2% FBW to 16% FBW 1GHz. Effective improvement for the passband flatness is observed at all bandwidth states of the measurement results. The passband insertion loss variation during the bandwidth tuning is maintained within 1 dB.

4.7 Reference

[1] R. Gómez-García, J. Muñoz-Ferreras, J. Jimenéz-Campillo, F. Branca-Roncati, and P. Martín-Iglesias, 'High-Order Planar Bandpass Filters With Electronically-Reconfigurable Passband Width and Flatness Based on Adaptive Multi-Resonator Cascades', *IEEE Access*, vol. 7, pp. 11010–11019, 2019.

[2] C. Quendo, E. Rius, and C. Person, 'Narrow Bandpass Filters Using Dual-Behavior Resonators', *IEEE Transactions on Microwave Theory and Techniques*, vol. 51, no. 3, pp. 734–743, Mar. 2003.

[3] J.-S. Hong, *Microstrip Filters for RF / Microwave Applications*, 2nd Edition edition. Hoboken, N.J: Wiley-Blackwell, 2011.

[4] A. Basti, A. Périgaud, S. Bila, S. Verdeyme, L. Estagerie, and H. Leblond, 'Design of Microstrip Lossy Filters for Receivers in Satellite Transponders', *IEEE Transactions on Microwave Theory and Techniques*, vol. 62, no. 9, pp. 2014–2024, Sep. 2014.

[5] J. Ni, J. Hong, and P. M. Iglesias, 'Compact Microstrip IF Lossy Filter with Ultra-Wide Stopband', *IEEE Transactions on Microwave Theory and Techniques*, pp. 1–8, 2018.

[6] A. C. Guyette, I. C. Hunter, and R. D. Pollard, 'The Design of Microwave Bandpass Filters Using Resonators With Nonuniform Q', *IEEE Transactions on Microwave Theory and Techniques*, vol. 54, no. 11, pp. 3914–3922, Nov. 2006.

[7] H. Guo, J. Ni, and J. Hong, 'Varactor-Tuned Dual-Mode Bandpass Filter with Nonuniform Q Distribution', *IEEE Microw. Wireless Compon. Lett.*, vol. 28, no. 11, pp. 1002–1004, Nov. 2018.

CHAPTER 5
TUNABLE ACTIVE FILTER

5.1 Introduction

High-performance reconfigurable microwave and RF filter with low loss are in huge demand for modern wireless communication systems. However, it is difficult to obtain a high-Q factor resonator while keeping a compact size, especially when the high-loss varactors present in a narrow bandpass filter. Lossy techniques such as non-uniform Q distribution and resistive cross-coupling have been proposed to overcome the high in-band insertion loss variation caused by the low Q of resonators. In previous chapters, tunable filters with different lossy techniques have been developed to improve the passband flatness at the expense of high passband insertion loss. However, for the same absolute bandwidth, filters working at a higher frequency have even greater loss than the low frequency because the fractional bandwidth is less. The lossy filter techniques may not be applicable in this case because of the selectivity degradation caused by the high loss.

Alternatively, the active filters including active resonator [3] – [6], active couplings [7] and other types [8] are well-known that it can compensate the loss within the filters. Loss in tunable filters is mainly contributed by varactors loss, conductor loss, dielectric loss, and radiation loss. An equivalent resistance could be applied to represent all the passive losses in the resonator. A negative resistance, which is different from the ordinary resistor, is a behaviour that the current and voltage are inversely proportional to each other. Thus, effectively loss cancellation could be realized by introducing an appropriate amount of negative resistance created using active transistor circuits [9].

In this chapter, the focus has been put on the development of a varactor-tuned 2-pole active filter. With the proposed coupling configuration, the coupling coefficient variation between resonators can be adjusted, so the constant ABW can be maintained. The filter loss and varactor loss are compensated by the active circuits with negative resistances. Experiments are carried out to validate the design.

5.2 Tunable Filter with A Constant ABW

5.2.1 Design Fundamentals

In frequency reconfigurable filters, the characteristic of the bandwidth variation is an important issue. The control of coupling coefficients and external Q factor against the tuning of resonator frequency is essential. For instance, a constant coupling coefficient between resonators will produce a constant FBW. To maintain a constant absolute bandwidth for a centre frequency tuned filter, the coupling coefficient must vary inversely with the tuning frequency, while the external Q factor should vary proportionally against the frequency. Tunable combline filters have been proposed in [10], [11] for the constant absolute bandwidth of filters. In [10], step impedance microstrip-line resonators are applied to control the ratio between electric and magnetic couplings, so the coupling coefficient between resonators can vary properly against the centre frequency. The desired coupling coefficient can also be achieved by using bent combline resonator as presented in [11], where the magnetic coupling is dominating. In our design, an open-end coupling scheme is implied to achieve the required coupling coefficient for the constant absolute bandwidth.

5.2.2 Coupling Configuration for Constant ABW

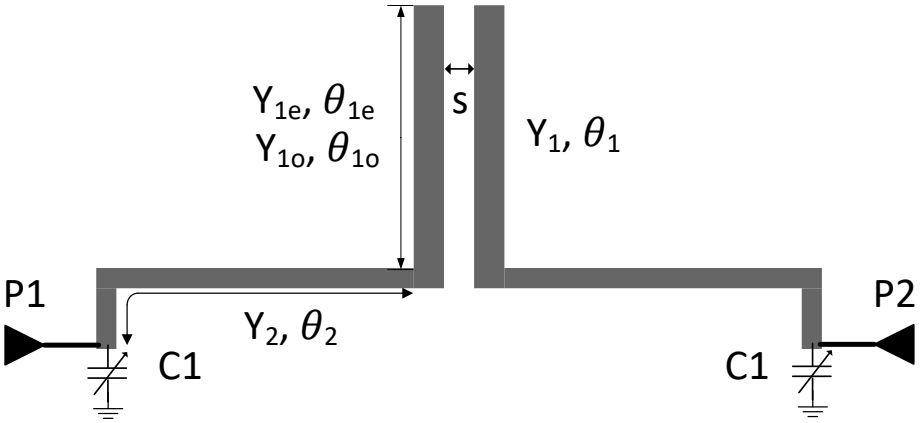

Figure 5.1 Layout of the coupled resonators of the tunable filter.

Figure 5.1 shows the layout of the electric-coupled (Y_{1e}, Y_{1o}) resonator pair. The $\lambda/2$

microstrip-line resonator is loaded with varactor diodes C_1 at one end while the other end is open. With this arrangement, the Q of the tuned resonator is higher than the conventional $\lambda/4$ resonator [12]. Thus, the resonating frequency ω_0 of the filter centre frequency can be found by the input admittance of a single resonator as

$$Y_{in}(\omega) = 0 \tag{5.1}$$

$$Y_{in} = j\omega C_1 + jY_2 \frac{Y_1 \tan(\theta_1) + Y_2 \tan(\theta_2)}{Y_2 - Y_1 \tan(\theta_1)\tan(\theta_2)} \tag{5.2}$$

The input even- and odd-mode admittances Y_{ine}, Y_{ino} of the filter seen from the observation points P1, P2 are given by

$$\begin{aligned} Y_{ine} &= j\omega C_1 + Y_{re} \\ Y_{ino} &= j\omega C_1 + Y_{ro} \end{aligned} \tag{5.3}$$

where

$$\begin{aligned} Y_{re} &= Y_2 \frac{Y_{1e}' + jY_2 \tan(\theta_2)}{Y_2 + jY_{1e}' \tan(\theta_2)} \\ Y_{ro} &= Y_2 \frac{Y_{1o}' + jY_2 \tan(\theta_2)}{Y_2 + jY_{1o}' \tan(\theta_2)} \end{aligned} \tag{5.4}$$

$$\begin{aligned} Y_{1e}' &= jY_{1e} \tan(\theta_{1e}) \\ Y_{1o}' &= jY_{1o} \tan(\theta_{1o}) \end{aligned} \tag{5.5}$$

Therefore, the admittance matrix of the coupled capacitive loaded resonator can be found as

$$Y = \begin{bmatrix} Y_{11} & Y_{12} \\ Y_{21} & Y_{22} \end{bmatrix} = \begin{bmatrix} \frac{Y_{ine} + Y_{ino}}{2} & \frac{Y_{ine} - Y_{ino}}{2} \\ \frac{Y_{ine} - Y_{ino}}{2} & \frac{Y_{ine} + Y_{ino}}{2} \end{bmatrix} \tag{5.6}$$

The slope parameter b of the coupled resonators is defined by the imaginary part of the admittance [13]

$$b = \mathrm{Im}\left[\frac{\omega_0}{2} \frac{\partial Y_{11}(\omega_0)}{\partial \omega} - \frac{Y_{11}(\omega_0)}{2} \right] \tag{5.7}$$

Thus, the coupling coefficient is given as

$$k = \frac{\mathrm{Im}[Y_{12}(\omega_0)]}{b} \tag{5.8}$$

By applying the above equations, the design parameters of the coupled resonators for a constant ABW of 120 MHz with $\pm 5\%$ variation are given as follows: $Z_{1e} = 85.783\ \Omega$, $Z_{1o} = 66.72\ \Omega$, $Z_1 = 75.94\ \Omega$, $\theta_1 = 33.45°$,$Z_2 = 91.4\ \Omega$ and $\theta_2 = 61.03°$ at 4 GHz, where the loaded capacitance C_1 is from 0.3 pF to 1.1 pF. The tuning range of the filter is calculated by (5.1) – (5.2) from 4.5 GHz to 5.55 GHz. Therefore, Figure 5.2 gives the calculated coupling coefficients, and the desired coupling coefficient line is also given in Figure 5.2 for reference. As can be seen, the coupling coefficient is inversely proportional to the centre frequency as proposed. A $\pm 5\%$ bandwidth variation over the tuning would be caused by the deviation from the ideal coupling coefficient line.

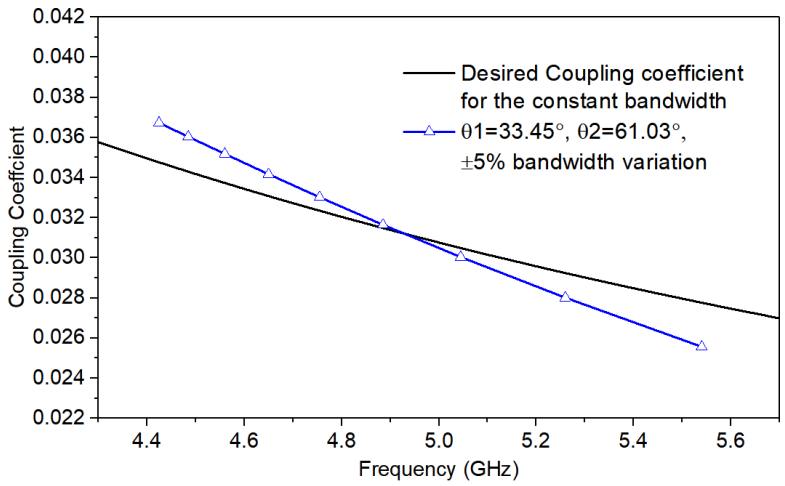

Figure 5.2 Coupling coefficient of the circuit in Figure 5.1 as a function of the centre frequency. ($Z_{1e} = 85.783\ \Omega$, $Z_{1o} = 66.72\ \Omega$, $Z_1 = 75.94\ \Omega$, $Z_2 = 91.4\ \Omega$, electrical lengths are given at 4 GHz)

5.2.3 Filter Layout and Frequency Responses

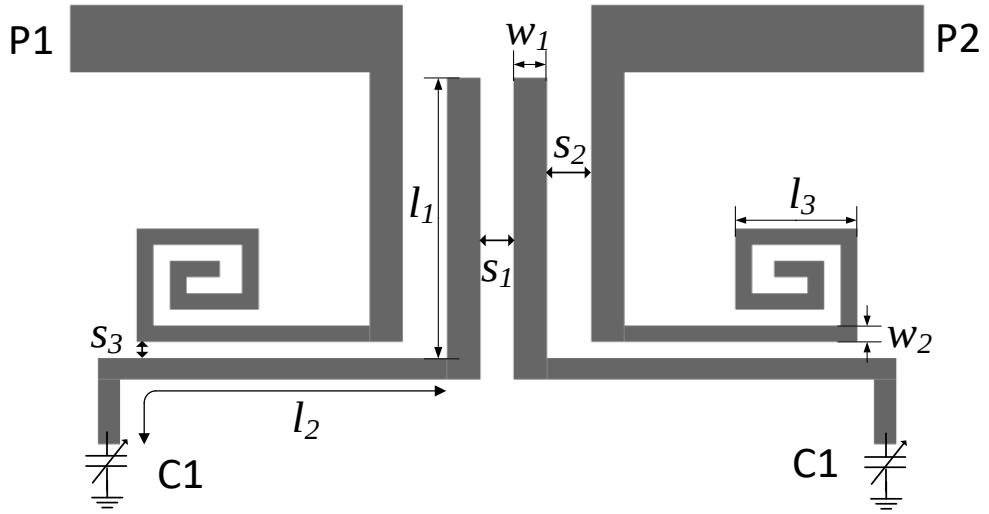

Figure 5.3 Layout of the proposed reconfigurable filter, based on substrate RO3003 with a dielectric constant of 3 and a thickness of 0.51 *mm*.

Based on the analysis above, the designed layout of the tunable filter is presented in Figure 5.3, which is based on a substrate of RO3003 with a dielectric constant of 3 and a thickness of 0.51 *mm*. The dimension parameters of the proposed filter are given in Table 5.1. Mixed electric and magnetic coupling scheme is applied for the external coupling to maintain proper external feeding during the frequency tuning. The external quality factor of the filter which is proportional to the frequency is extracted in Figure 5.4. As a result, the frequency responses of the filter given in Figure 5.5 can be obtained by the EM simulation. For a variable capacitance of 0.3 pF to 1.1 pF, as we can see, the passband is tuned from 4.45 GHz to 5.6 GHz with an ABW of 120 MHz $\pm$ 6 MHz.

Table 5-1 Parameters of the proposed reconfigurable filter in Figure 5.3

l_1	l_2	l_3	w_1	w_2
4.6 *mm*	8.5 *mm*	2.2 *mm*	0.6 *mm*	0.3 *mm*
s_1	s_2	s_3	C_1	
0.6 *mm*	0.8 *mm*	0.3 *mm*	0.3 – 1.1 pF	

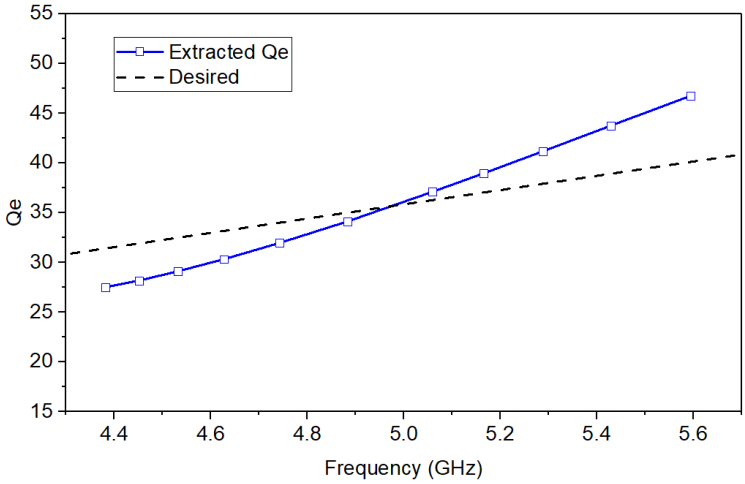

Figure 5.4 Extracted external quality factor of proposed filter.

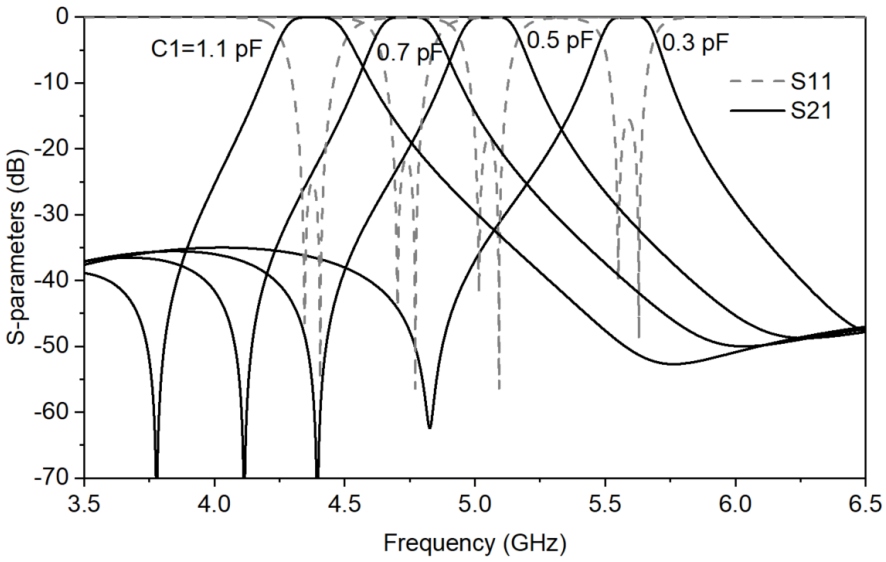

Figure 5.5 EM simulation of the proposed filter

5.3 Loss Compensation for Finite-Q Resonators

5.3.1 The Basic Structure

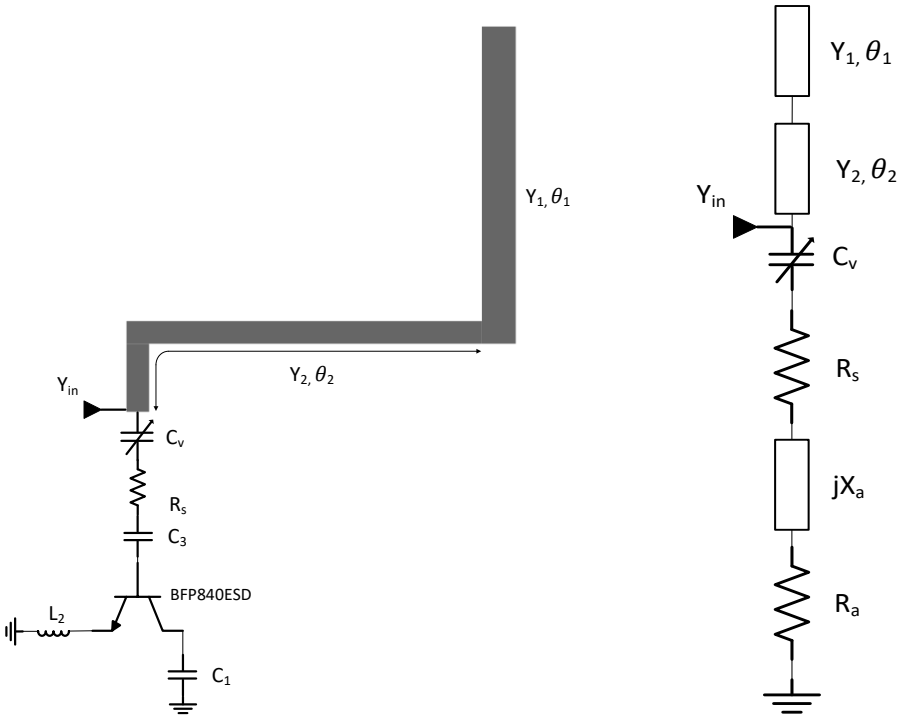

(a) (b)

Figure 5.6 (a) The proposed varactor tuned active resonator; (b) Equivalent circuit.

Figure 5.6 (a) illustrates the configuration of proposed varactor-tuned resonator loaded with an active circuit, where C_v is the variable capacitance of the varactor, R_s is the equivalent passive loss caused by the microstrip line and also varactor. The equivalent circuit of the resonator can be found in Figure 5.6 (b), where the transistor circuit is represented by an impedance of $Z_a = R_a + \mathrm{jX_a}$. Thus, the input admittance of the active resonator Y_{in}' is given as

$$Y_{in}' = \frac{1}{j\left(X_a - \left(\omega C_v\right)^{-1}\right) + R_s + R_a} + jY_2 \frac{Y_1 \tan(\theta_1) + Y_2 \tan(\theta_2)}{Y_2 - Y_1 \tan(\theta_1)\tan(\theta_2)} \tag{5.9}$$

For an idea loss compensation, the active circuit should have a negative resistance of $R_a = -R_s$. Moreover, because of the effect of the active circuit, the resonating frequency of the resonator now is can be calculated by

$$Y_{in}'(\omega)\big|_{R_a=-R_s} = 0 \tag{5.10}$$

5.3.2 Negative Resistance Circuit

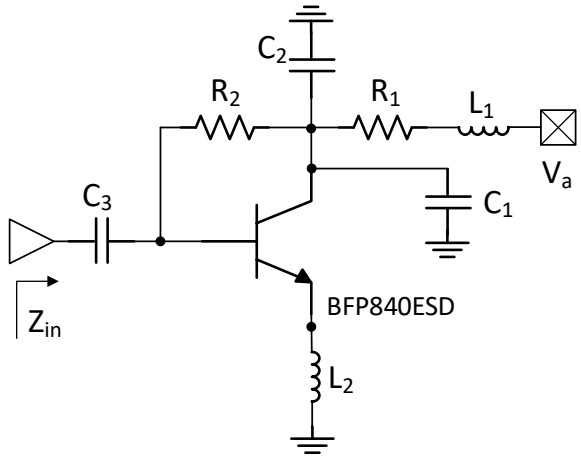

C_1	C_2	C_3	R_1	R_2	L_1	L_2
3 pF	47 pF	4.7 pF	10 kΩ	80.6 kΩ	20 nH	10 nH

Figure 5.7 Schematic of the active circuit based on the transistor BFP840ESD.

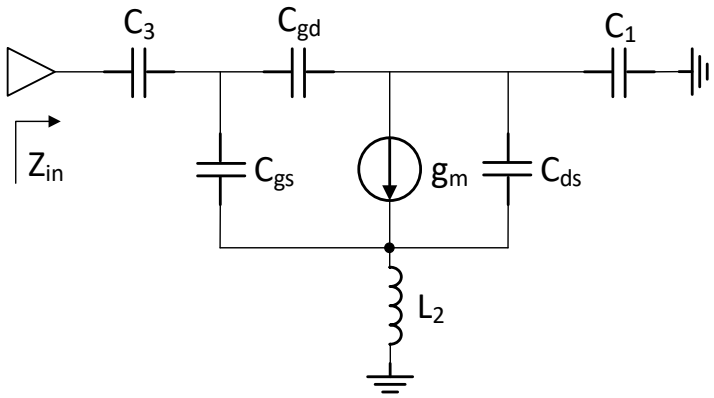

C_{gs}	C_{gd}	C_{gs}	g_m
0.41 pF	37 fF	0.41 pF	I_d/V_t

Figure 5.8 Equivalent circuit of the proposed active circuit [14].

The proposed NR circuit based on the HBT low-noise transistor BFP840ESD [14] is given in Figure 5.7, where R_1, R_2 are for the DC bias, and L_1, C_2 decouple the RF from DCs. The negative resistance of the active circuit is affected by components L_2, C_1,

C_3, and the transistor transconductance g_m. In order to estimate the negative resistance, Figure 5.8 shows the equivalent schematic of the proposed negative resistance circuit. Thus, the input impedance Z_{in} can be expressed by

$$Z_{in} = Z_b + \frac{1}{j\omega C_3} + \frac{\left(j\omega C_{gs} Z_a + 1\right)\left(j\omega C_{gs} Z_c + 1\right)}{j\omega C_{gs}\left(j\omega C_{gd} Z_c + 1\right) + j\omega C_{gd}\left(j\omega C_{gs} Z_a + 1\right)} \quad (5.11)$$

and the impedance Z_a, Z_b and Z_c can be obtained through the $\Delta - Y$ network conversion as

$$\begin{aligned} Z_a &= \frac{Z_1 Z_2}{Z_1 + Z_2 + Z_3} \\ Z_b &= \frac{Z_1 Z_3}{Z_1 + Z_2 + Z_3} \\ Z_c &= \frac{Z_2 Z_3}{Z_1 + Z_2 + Z_3} \end{aligned} \quad (5.12)$$

$$\begin{aligned} Z_1 &= j\omega L_2 \\ Z_2 &= \frac{1}{\left(g_m + j\omega C_{ds}\right)} \\ Z_3 &= \frac{1}{j\omega C_1} \end{aligned} \quad (5.13)$$

where $g_m = I_d / V_T$ is the transistor transconductance, V_T is the thermal voltage of 26 mV at the room temperature, and I_d is the drain DC bias current which can be manipulated by the bias voltage. The $I - V$ characteristics of the transistor can be obtained by the SPICE model provided by the manufacturer. The value of the negative resistance is given by the real part of (5.11) as

$$R_a = \mathrm{Re}\left(Z_{in}\right) \quad (5.14)$$

Thus, by changing the bias voltage, negative resistance R_a of the active circuit can be controlled. Figure 5.9 shows the negative resistances produced by the active circuit for a bias voltage from 1 V to 2V, and the equivalent capacitance of $\mathrm{Im}(Z_{in})$ is also given in the same graph. As can be seen, the working range of the proposed negative resistance circuit covers a frequency range from 3.5 GHz to 6.5 GHz. The generated

negative resistance is tuned from -20 Ω to 1 Ω, and it has low slopes in a narrow frequency band which guarantees an equal NR in the filter passband. Meanwhile, the equivalent capacitance C_a of the active circuit increases with the frequency, but it is less affected by the change of the bias voltage. Note that, the equivalent capacitance can be different when the circuit is built in the EM layout because of the effect of transmission lines.

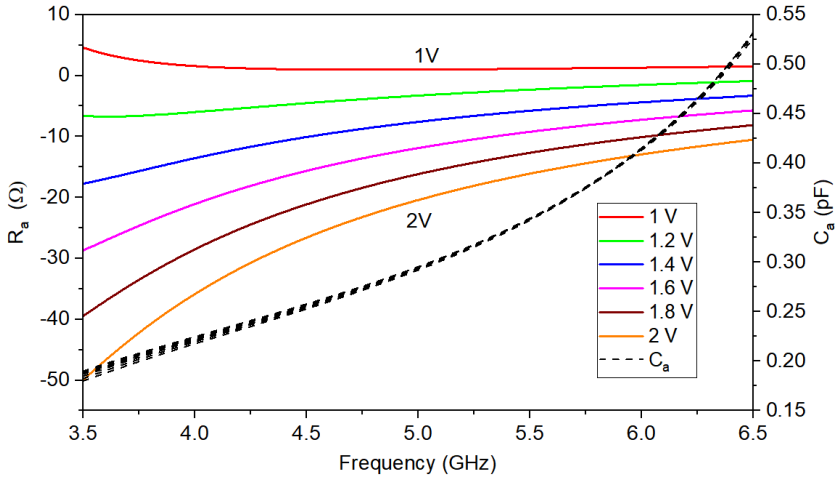

Figure 5.9 Negative resistance and the equivalent capacitance of the active circuit.

5.3.3 Resonator with NR Circuit

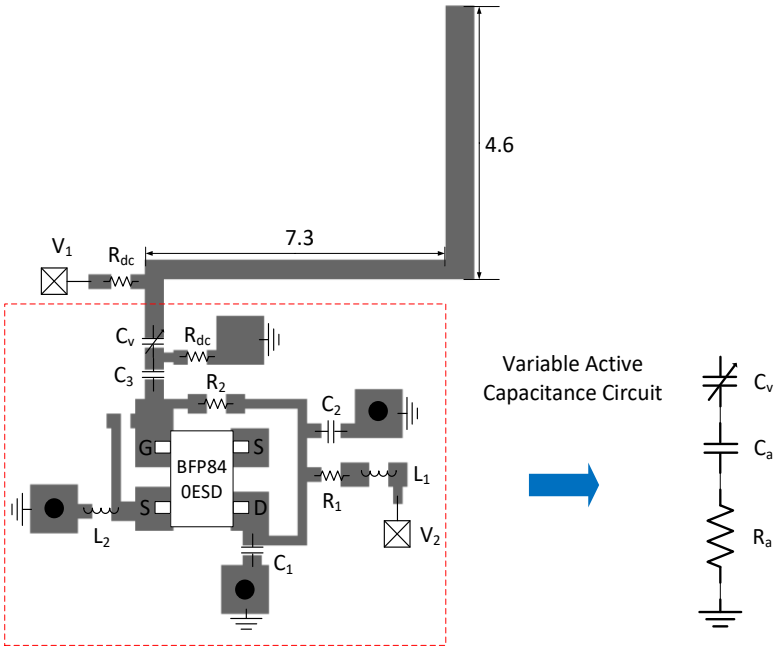

Figure 5.10 Tunable resonator with active tuning circuit.

Based on the proposed resonator in the previous tunable filter design, Figure 5.10 presents the layout of a tunable active resonator which consists of varactor diode C_v and the negative resistance circuit. The components' values can be found in Figure 5.7 while resistors R_{dc} is the high resistance RF block for DC bias. The DC bias voltage V_1 controls the capacitance of the varactor diode C_v, and the variable capacitance for the resonator is the result of the combination of the varactor capacitance C_v and the capacitance of the active circuit C_a. The value of the negative resistance can be adjusted by the DC bias voltage V_2.

Thus, Figure 5.11 gives the simulated insertion loss of the tuned active resonator and a comparison with the resonator having passive loss only. The EM simulation is performed in the ADS simulator [15]. As can been seen, for a variable capacitance of $C_v = 0.3\,pF - 1.1\,pF$, the frequency of the resonator is tuned from 4.9 GHz to 5.95 GHz. The presence of negative resistance improves the resonator Q within the tuning range as the insertion loss at resonating frequency remains less than 0.1 dB. In addition, during experimental investigation, unstable issue was observed with serious noises when a lower negative resistance is applied and pushes the S21 above 0 dB. Thus, the negative resistance compensation is limited down to 0 dB insertion loss.

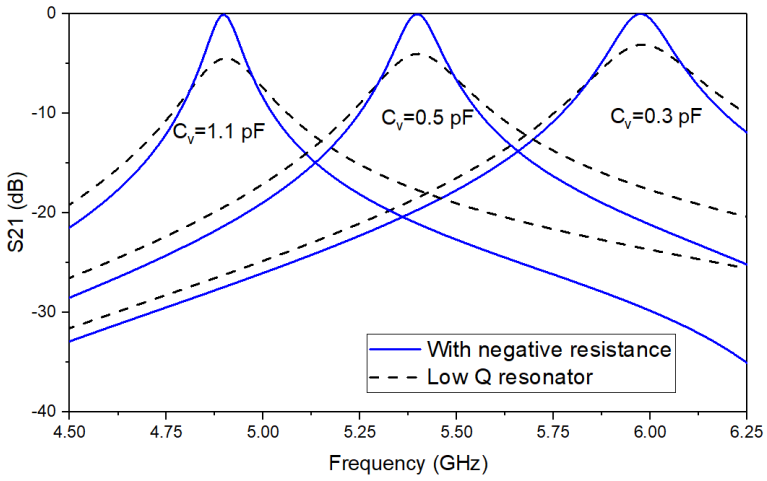

Figure 5.11 Simulated insertion loss of the tuned resonator with negative resistance compares to the resonator without the negative resistance.

5.4 Tunable 2-pole Active Filter

5.4.1 Filter Design and Simulation

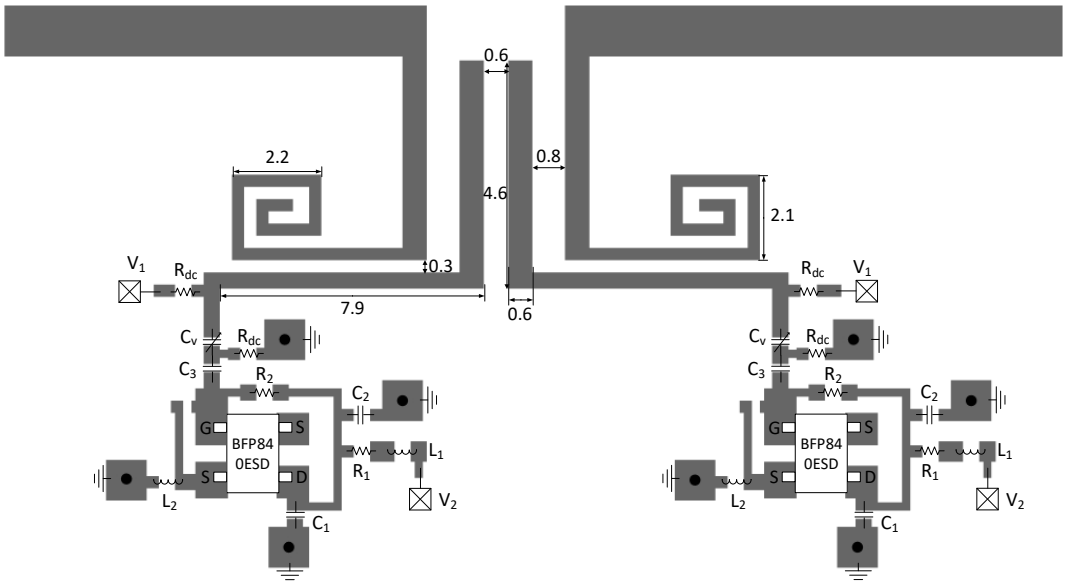

Figure 5.12 Layout of the proposed tunable 2-pole active filter.

The detailed layout of the proposed tunable 2-pole active filter is shown in Figure 5.12, where each resonator is connected to a negative resistance circuit. The circuit is designed on the RO3003 substrate with a dielectric constant of 3 and a thickness of 0.51 *mm*. The dielectric loss ($tan\,\delta = 0.0013$) and the printed metallisation ($\sigma = 5.8 \times 10^7\ s/m$) are considered. The overall size of the 2-pole filter is $26\,mm \times 14\,mm$ including active circuits. Varactor diodes used in the frequency tuning is the MA46H120 from MACOM [16] with a capacitance tuning range of 0.2 pF – 1.1 pF. Varactors DC bias circuit is using 100 kΩ Panasonic chip resistors to block the RF signal. AVX Accu-P series RF capacitors [17] are used for all the capacitors in the design, and the Coilcraft high-Q inductors are used for L_1, L_2 [18]. The performance of the varactor can be 126nfineon by the SPICE model in ADS as the discussion in Chapter 2. Furthermore, the passband frequency of the filter is controlled by the DC voltage V_1, then the negative resistance is adjusted by the voltage V_2 to compensate the passband insertion loss. In this manner, the full-wave EM simulation results are presented in Figure 5.13 (a). As can be seen, the passband is tuned from 4.9 GHz to 6 GHz with a 1-dB absolute bandwidth of 120 MHz $\pm$ 10 MHz while the minimum

passband insertion loss is maintained less than 0.2 dB during the frequency tuning. Based on the SPICE model provide by the manufacture, ADS simulations have been performed in Figure 5.13 (b) to estimate the noise figure (NF) of the active filter at four frequency states, respectively. The passband NF of 6.19 – 6.53 dB can be observed during the frequency tuning.

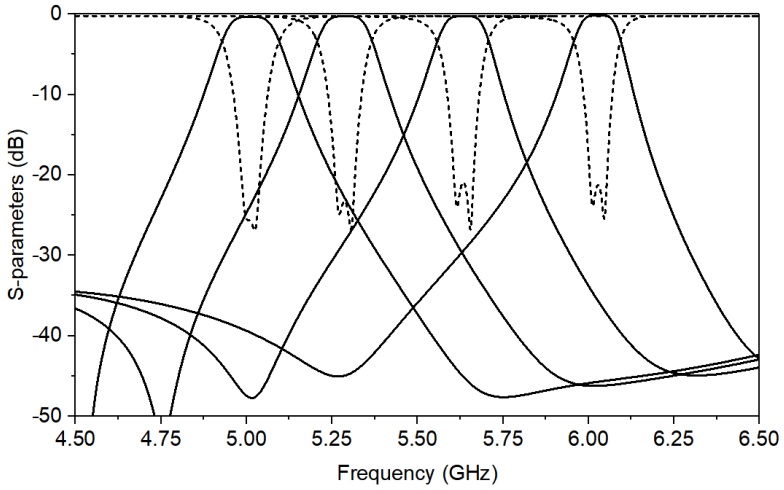

(a)

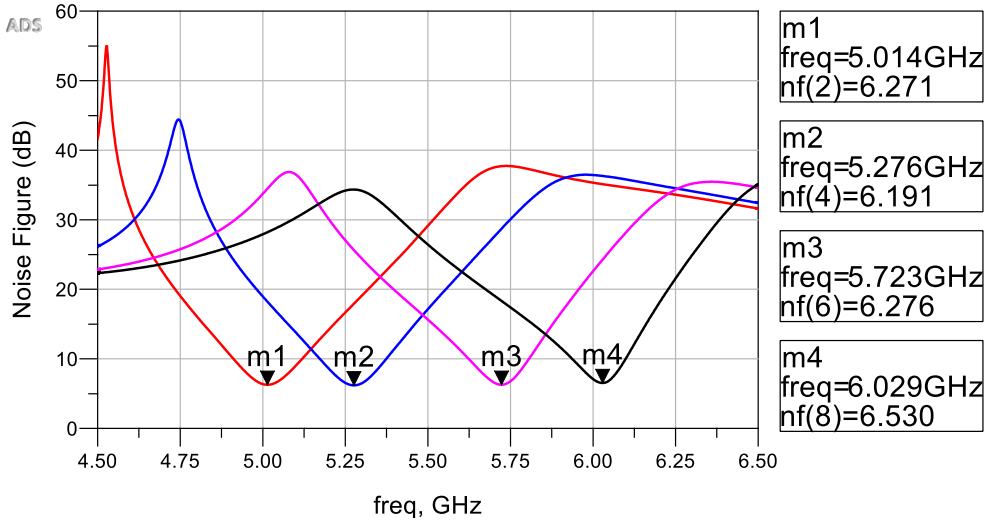

(b)

Figure 5.13 Simulated filter responses of the tuned 2-pole active filter; (a) S-parameters, (b) Noise figure.

5.4.2 Fabrication and Measurement

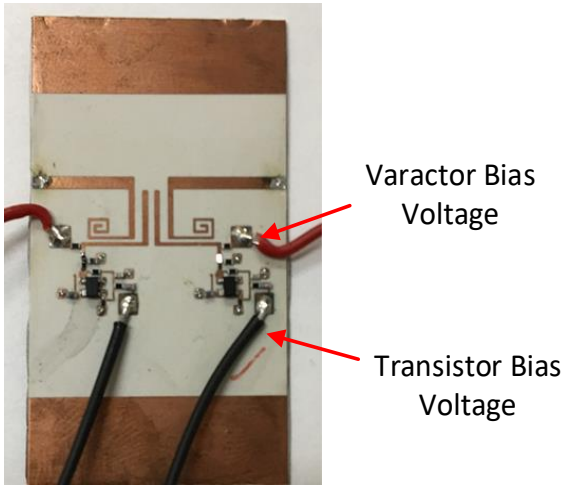

Figure 5.14 Photograph of the fabricated 2-pole tunable active filter.

The picture of the fabricated 2-pole active filter is shown in Figure 5.14. As described, two control voltages are employed for varactors and transistors. The filter is measured with a signal power of -30 dBm. For the passband frequency at 4.9 GHz, Figure 5.15 shows the filter passband variation when transistor bias voltage V_2 are increasing. The given current I_2 is the total current of two transistor circuits. A step-by-step reduction of the insertion loss can be observed with the increasing voltage. The power consumption of the active filter for a minimum passband insertion loss of 0.2 dB is measured as 0.435 mW.

Figure 5.16 shows the frequency tuning of the 2-pole active filter. As expected, the passband frequency can be reconfigured from 4.88 GHz to 6.04 GHz with a 1-dB absolute bandwidth of 120 ± 10 MHz. The minimum passband insertion loss is maintained below 0.4 dB while the filter return loss is kept above 9 dB. The measured power consumption of the fabricated filter is 0.56 mW – 0.785 mW for all frequency states.

It is well known that small-signal transistors have limited power handling capacity. Thus, Figure 5.17 plots the filter responses with different input signal powers giving the power handling capacity of the active filter. As can be seen, the filter can work with a -30 dBm signal power without considerable passband distortion. However, when the input power is increased to -20 dB with no bias voltage changes, the passband insertion

loss at 5.64 GHz state is compressed to -3.69 dB. Meanwhile, the reduction of the insertion loss at 6.04 GHz state is mild as 1.48 dB because of the higher bias voltages V_1 and V_2.

Last but not least, the measured results of the filter on a wideband frequency band are given in Figure 5.18 for the centre frequency states of 5.31 GHz and 6.04 GHz. The spurious frequency of the tunable filter is observed after 14 GHz for both tuning states while the stopband rejection is more than 25 dB up to 13 GHz frequency.

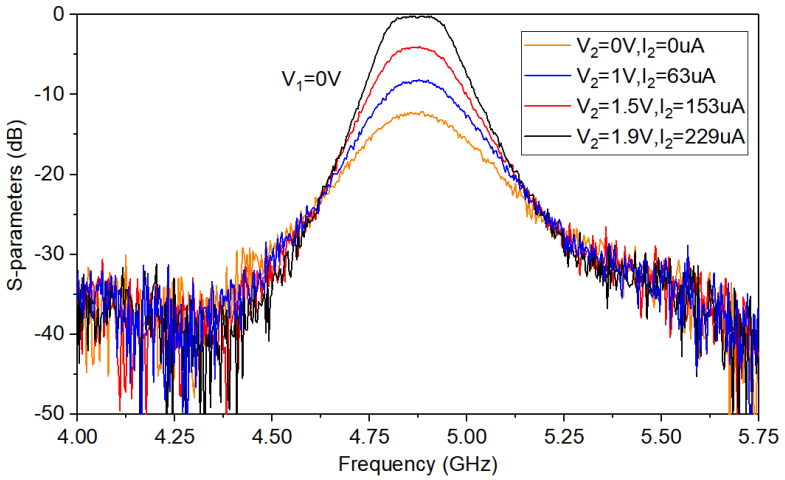

Figure 5.15 Insertion loss compensation vs the transistor bias voltage and current, input power of -30 dBm.

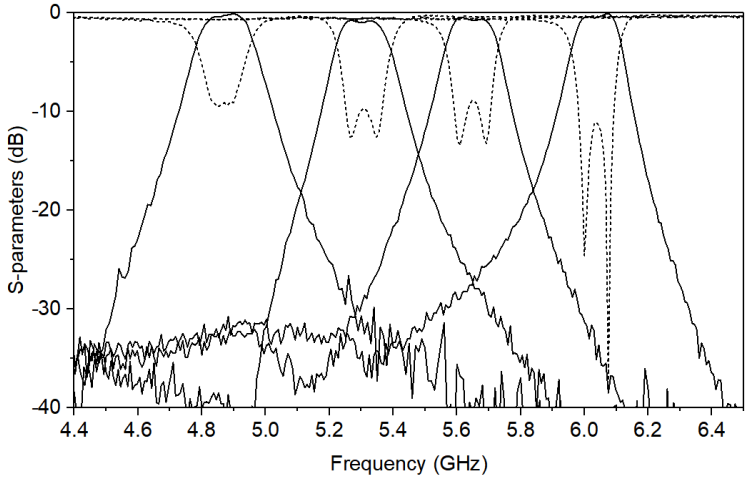

Figure 5.16 Measured frequency responses of the tunable 2-pole active filter.

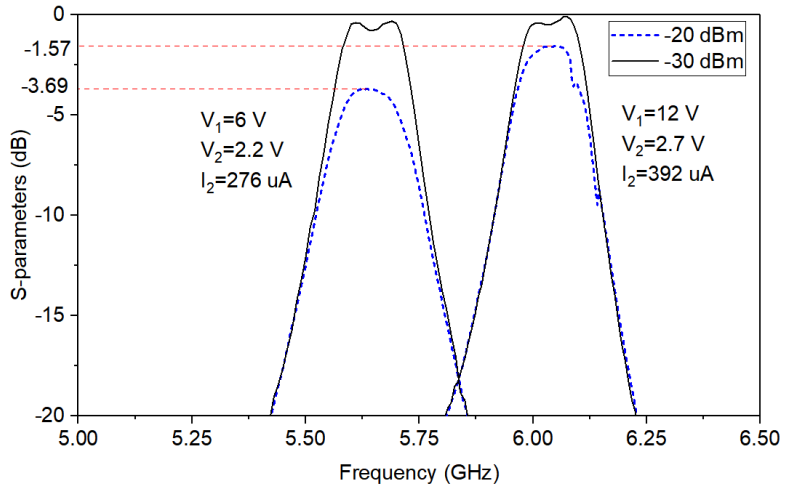

Figure 5.17 Measured filter responses with different power level of input signal.

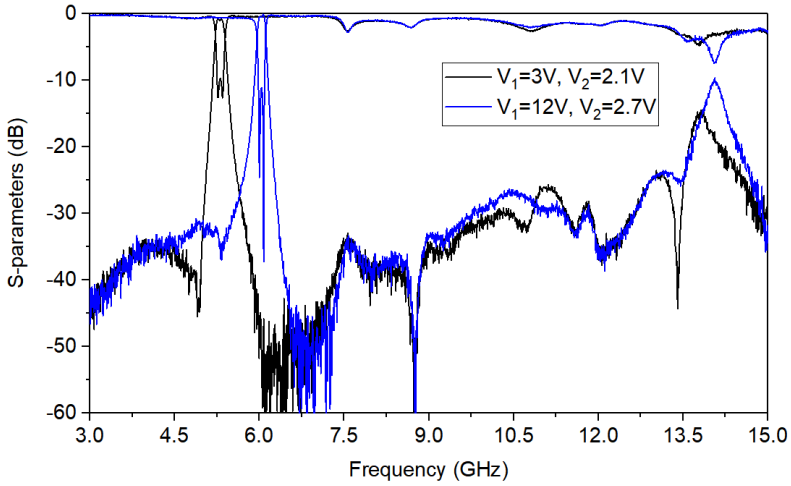

Figure 5.18 Wideband responses of the measured tunable active filter.

5.5 Conclusion

In this chapter, a varactor-tuned 2-pole microstrip filter is demonstrated with negative resistance circuits. Constant absolute bandwidth tuning property has been investigated. Filter passive loss and varactor loss are compensated by the negative resistance generated by the active circuit. The network synthesis for the proposed negative resistance circuit is presented. The filter shows a frequency tuning range of 26% from 4.88 GHz to 6.04 GHz. The measured 1-dB absolute bandwidth of the filter is $120 \pm 10\ MHz$ (2.46% - 1.98% FBW) over the tuning range. The passband insertion loss is maintained below 0.4 dB while the passband frequency is tuned. The power handling capacity is also demonstrated with different input power levels. Comparing to the lossy

filter with a cascaded amplifier, such an active filter can maintain a high selectivity when the bandwidth is small. However, a limitation of the compensation has been identified that the negative resistance cannot achieve negative insertion loss.

Because of the short of measurement equipment, the noise figure only is given by the SPICE models of transistor and varactor diode in ADS simulation. The simulated noise figure of the tunable filter is 6.19 – 6.53 dB. The NF measurement is expected in the future. Stability issue has been observed during the measurement, and it causes noises to the filter responses. Operational amplifier (OPAMP) can be considered to replace the HBT transistor for a better stability.

5.6 Reference

[1] J. Ni, W. Tang, J. Hong, and R. H. Geschke, 'Design of Microstrip Lossy Filter Using an Extended Doublet Topology', *IEEE Microwave and Wireless Components Letters*, vol. 24, no. 5, pp. 318–320, May 2014.

[2] A. C. Guyette, I. C. Hunter, and R. D. Pollard, 'The Design of Microwave Bandpass Filters Using Resonators with Nonuniform Q', *IEEE Transactions on Microwave Theory and Techniques*, vol. 54, no. 11, pp. 3914–3922, Nov. 2006.

[3] C.- Chang and T. Itoh, 'Microwave Active Filters Based on Coupled Negative Resistance Method', *IEEE Transactions on Microwave Theory and Techniques*, vol. 38, no. 12, pp. 1879–1884, Dec. 1990.

[4] X. G. Wang, Y. H. Cho, and S. W. Yun, 'A Tunable Combline Bandpass Filter Loaded with Series Resonator', *IEEE Transactions on Microwave Theory and Techniques*, vol. 60, no. 6, pp. 1569–1576, Jun. 2012.

[5] Young-Hoon Chun, Jae-Ryong Lee, Sang-Won Yun, and Jin-Koo Rhee, 'Design of an RF Low-noise Bandpass Filter using Active Capacitance Circuit', *IEEE Transactions on Microwave Theory and Techniques*, vol. 53, no. 2, pp. 687–695, Feb. 2005.

[6] D. K. Adams and R. Y. C. Ho, 'Active Filters for UHF and Microwave Frequencies', *IEEE Transactions on Microwave Theory and Techniques*, vol. 17, no. 9, pp. 662–670, Sep. 1969.

[7] Young-Hoon Chun, Sang-Won Yun, and Jin-Koo Rhee, 'Active Impedance Inverter: Analysis and Its Application to the Bandpass Filter Design', in *2002 IEEE MTT-S International Microwave Symposium Digest (Cat. No.02CH37278)*, Jun. 2002.

[8] Y. Gao, J. Powell, X. Shang, and M. J. Lancaster, 'Coupling Matrix-Based Design of Waveguide Filter Amplifiers', *IEEE Transactions on Microwave Theory and Techniques*, vol. 66, no. 12, pp. 5300–5309, Dec. 2018.

[9] S. R. Chandler, I. C. Hunter, and J. G. Gardiner, 'Active Varactor Tunable Microwave Filters', in *1993 23rd European Microwave Conference*, Sep. 1993, pp. 244–245.

[10] B.-W. Kim and S.-W. Yun, 'Varactor-tuned Combline Bandpass Filter using Step-impedance Microstrip Lines', *IEEE Transactions on Microwave Theory and Techniques*, vol. 52, no. 4, pp. 1279–1283, Apr. 2004.

[11] M. A. El-Tanani and G. M. Rebeiz, 'A Two-Pole Two-Zero Tunable Filter With Improved Linearity', *IEEE Transactions on Microwave Theory and Techniques*, vol. 57, no. 4, pp. 830–839, Apr. 2009.

[12] X. Y. Zhang, Q. Xue, C. H. Chan, and B.-J. Hu, 'Low-Loss Frequency-Agile Bandpass Filters with Controllable Bandwidth and Suppressed Second Harmonic', *IEEE Transactions on Microwave Theory and Techniques*, vol. 58, no. 6, pp. 1557–1564, Jun. 2010.

[13] G. Matthaei, E. M. T. Jones, and L. Young, *Microwave Filters, Impedance-Matching Networks, and Coupling Structures*. Norwood, Mass: Artech House, 1980.

[14] ‘BFP840ESD – Infineon’, Infineon Technologies AG. Available: https://www.infineon.com/cms/en/.

[15] *Advanced Design System*. USA: Agilent Technologies.

[16] ‘MA46H120 Series’, M/A-COM Lowell. Available: www.macom.com.

[17] ‘Accu-P Series RF capacitors’, AVX Corporation. Available: http://www.avx.com/.

[18] ‘Chip Inductors – 0402HP Series’, Coilcraft. Available: https://www.coilcraft.com/.

CHAPTER 6
CONCLUSION AND FUTURE WORK

6.1 Conclusion

The thesis has presented the developments of varactor based tunable planar filters with high performances in terms of selectivity, tunability, and passband flatness, which can utilise the valuable RF spectrum more efficiently and increase communication capability and functionality. To understand the bottleneck of current tunable filter techniques, a review of state-of-the-art varactor-tuned filters and performance-enhancement techniques is presented in Chapter 2. The first part of the thesis considers applying the lossy filter concept to improve the passband flatness of the bandwidth tuned filter. Due to the narrow band limitation of the lossy filter, the second part of this thesis discusses those narrow FBW tunable filters at C-band frequency. Active filter techniques are applied for high-Q filter responses.

In detail, the major accomplishment of the research presented in this dissertation are summarised as below:

In Chapter 3, a new type of electronically reconfigurable microstrip bandpass filter is introduced with both bandwidth and centre-frequency tuning. By using the parallel network topology of the dual-mode resonator, the passband flatness can be enhanced in a simple way by loading resistor on the symmetrical plane of the resonator to reduce odd-mode Q. Thanks to the property of the dual-mode open-loop resonator, two intrinsic band-side transmission zeros are introduced without any cross-coupling. Four-pole high selective tunable responses were measured, and they exhibited a good passband flattening for 10% to 25% FBW.

Chapter 4 presents a type of 5-pole high selective bandpass filter consisting of hairpin resonators and dual behaviour resonators. The filter presents a wide bandwidth tunability and controllable transmission zeros. To efficiently improve the filter passband flatness at the narrow bandwidth state, a novel centre-loaded resistive cross-coupling structure is introduced. The reduction of in-band insertion-loss variation can be achieved by connecting middles of resonators through a proper resistance. Effective

improvement on the in-band flatness is observed with a bandwidth tuning range of 2% to 16% at 1 GHz. An in-band insertion-loss variation of 1 dB is maintained for 2% FBW.

A tunable 2-pole filter working at C-band frequency is discussed in Chapter 5. Using an electric coupling scheme, a constant absolute bandwidth of 120MHz (2.46% - 1.98% FBW) is preserved when the frequency is changing. To overcome the loss within the filter, a small signal transistor circuit is developed that can provide negative resistance over a wide frequency range. Design equations are derived to predict the value of resistance generated by the circuit. Thus, the filter loss can be cancelled by this negative resistance, and the fabricated filter presents a high-Q resonator performance. The power handling capacity is also demonstrated with different input power levels.

6.2 Future Work

Suggestions for future development based on the works presented in this thesis are given:

- A lossy dual-mode filter topology has been demonstrated with a 4-pole tunable filter example in Chapter 3. Higher-order filters based on this topology is expected.
- The proposed CLRCCs lossy configuration in Chapter 4 enlarges the overall filter size because of the $\lambda/2$ transmission lines for connecting resistors. Alternative configurations could be investigated to replace those lines.
- The tunable lossy filters demonstrated in Chapter 4 have poor stopband performances. Further exploitations can be done to obtain better out-of-band rejections in stopbands.
- A tunable filter with active circuits has been demonstrated in Chapter 5. However, the stability issue creates significant noise within the passband. For

the future work, OPAMP is suggested to replace the HBT transistor to improve the filter performance. Furthermore, because the current lossy filter application has an amplifier-filter-amplifier architecture, as an extension in the future, it would be interesting to investigate the co-design of lossy-filter and amplifiers for size reduction. Tunability feature could also be considered in the co-design.

APPENDIX

Q Factor Extraction for Varactors

A. Extraction for The Varactor Diode – MA46H120

The details of the Q factor extraction for varactors are demonstrated in this section. The method of varactor-loaded-resonator is used to measure the varactor Q around 6GHz. The device under test (DUT) is the varactor MA46H120 [1] which has a stated capacitance range of 0.17 pF to 1.1 pF and the package size of 0201.

Because of the depletion region changes with the biasing voltage, measurement is going to cover varactor's two terminal conditions of $C_J = 0.17$ pF and $C_J = 1.1$ pF. Therefore, as shown in Fig.1 (a), varactor loaded resonator A is resonating around 6 GHz for $C_J = 0.17$ pF. In the meantime, resonator B with similar configuration is resonating around 6 GHz when the C_J is 1.1 pF. Fig. (c) shows the simulation responses of those two resonators without varactor loss. The resonator is fabricated on the substrate RO3003 with a thickness of 0.51 *mm*, a dielectric constant of 3, and a tangent loss of 0.0013. High resistances (100 kΩ) are placed between DC and RF as the RF blocks.

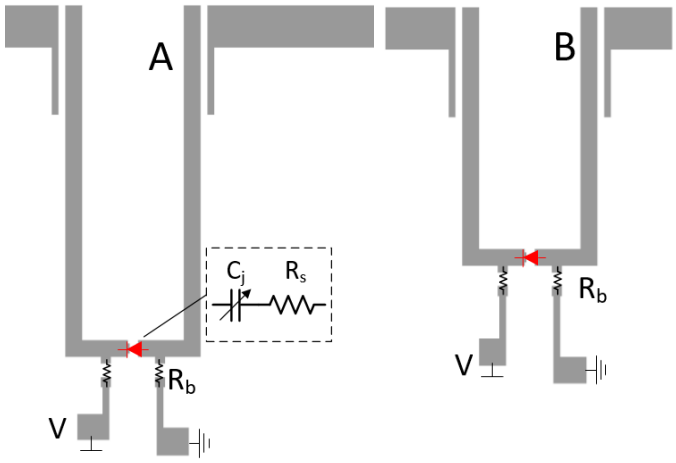

(a) (b)

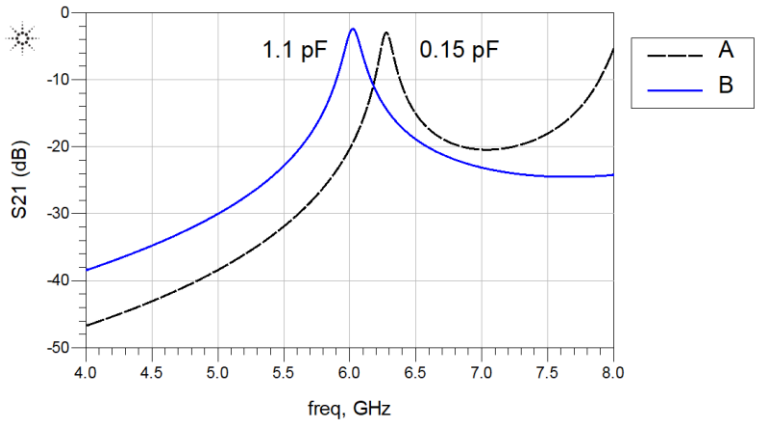

(c)

Fig. 1 Q extraction with resonator, (a) Resonator for $C_J = 0.15\ pF$; (b) Resonator for $C_J = 1.1\ pF$; (c) Frequency responses for two resonators.

As the unloaded-Q factor extraction method introduced in Section 2.13, the external feeding or excitation for the measured resonator needs to be very weak. However, in the actual measurement, the vector-network-analyser has a system noise floor. A feeble excitation leads to a low-level S21 which would be submerged under the noise floor. This can cause to the inaccuracy of the extraction results. Alternatively, as shown in Fig. 1 ©, the arranged excitation for the tested resonator is much larger for a high-level S21.

After the measurement, the obtained s-parameters are imported into the ADS simulator as Fig. 2. High impedance terminations are connecting to the imported s2p file. In such a manner, the feeble excitation is achieved in the simulation while the noise influence from the VNA is minimized. The measurement results after modified are given in Fig. 3. Using the equation (2.24), the calculated unloaded Q factors of two resonators are $Q_{0A} = 90$ and $Q_{0B} = 54$. The resonating frequencies of the resonators have shifted from simulations because of the parasitic effect and the fabrication error. By changing the parameters R_s in EM simulations, simulated Q-factors of resonators A and B are approached to the measurements. The estimated R_s for C_J = 0.15 pF is 3 Ω while the R_s is 2.2 for C_J = 1.1 pF.

Fig. 2 Measured data file terminated by high impedances in the ADS.

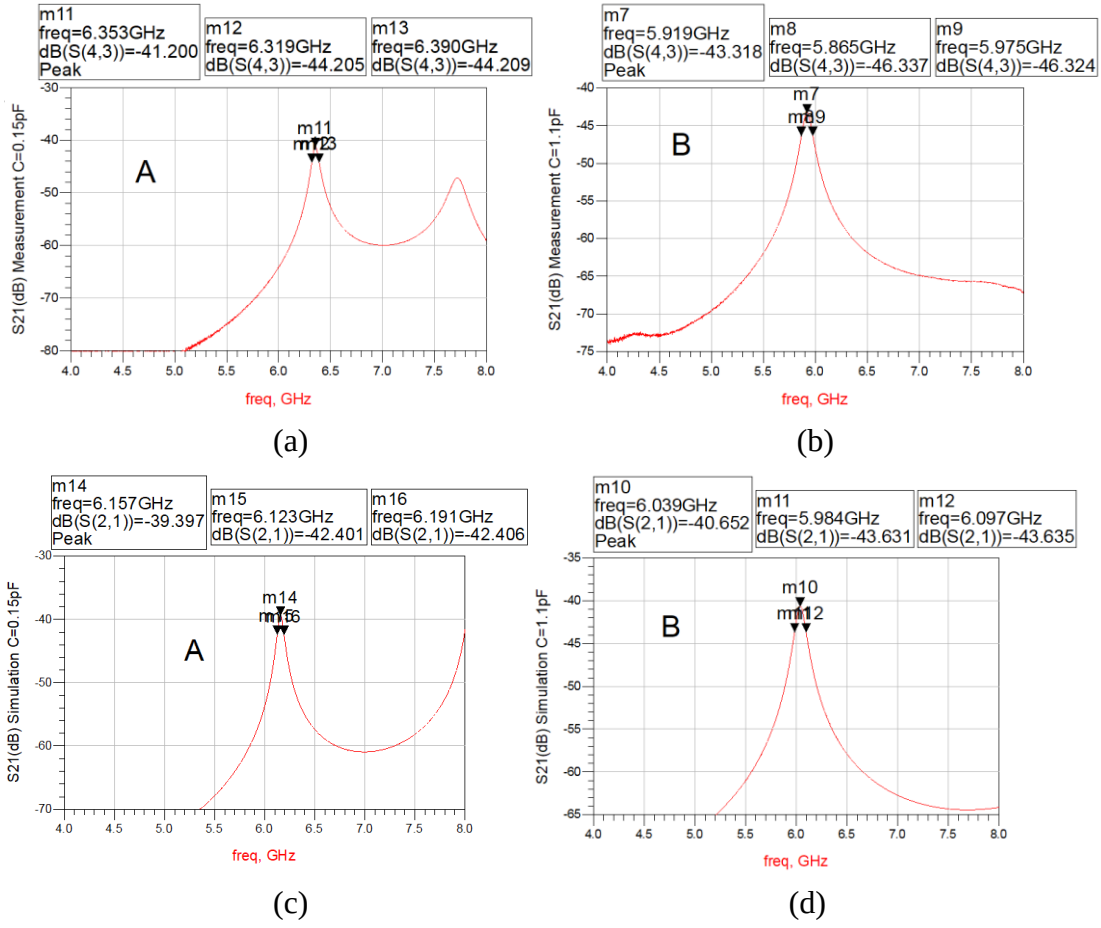

Fig. 3 (a), (b) Measurement results for C=0.15 pF and C=1.1 pF; (c), (d) Simulation approaching

Table.A. 1

Resonator	Measured Qu	Simulated Qu	Rs
A	89.5	90.5	3 Ω
B	54	53.5	2.2 Ω

B. Extraction for BST Varactor – TCP-5033UB

Herein, the BST varactor TCP-5033UB [2] characteristics are measured by the de-embedded method. Different from the varactor diode, given in Fig. 4, such BST varactor has a 3-port (6 pins) configuration where one extra port is used for DC biasing only. As shown the Fig. 5 (a), BST varactor is tested in a series 50-ohm environment with DC bias circuit. DC blocks are employing the 47 pF high-Q muRata ceramic capacitor [3] while the high resistance of 10 kΩ act as RF blocks dividing the DC circuit from the RF circuit.

Because the SLOT (Open, short, load, thru) calibration kits of the VNA is only capable to calibrate the measurement plane to the SMA interfaces, the effects of the substrate transitions connected to the DUT can't be removed by the VNA calibration kits. One optional technique is called Through-reflect-line (TRL) calibration that is often used to remove the effects of the test fixture in the de-embedded measurement. However, such a method needs to design additional cal-kits for the calibration.

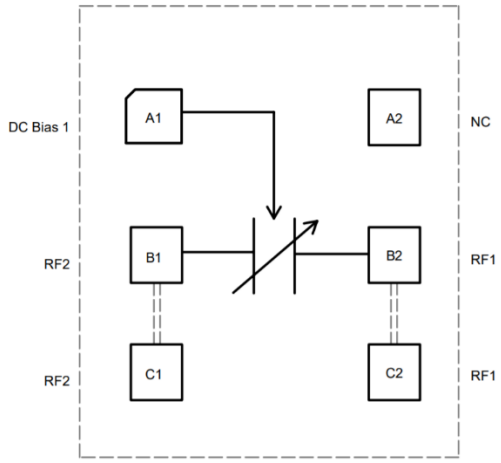

Ball / Pad Number	Pin Name	Description
A1	DC Bias 1	DC Bias Voltage
B1	RF2	RF Output
C1	RF2	RF Output
A2	NC	Not Connected
B2	RF1	RF Input
C2	RF1	RF Input

Fig. 4 Pin layout of the BST varactor [2]. (Top view)

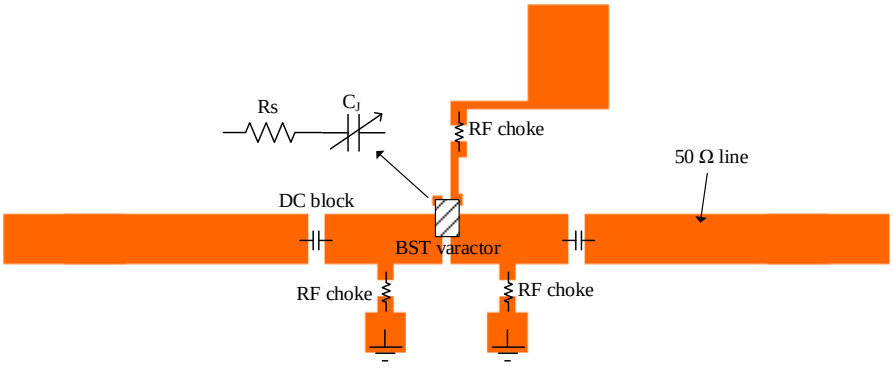

(a)

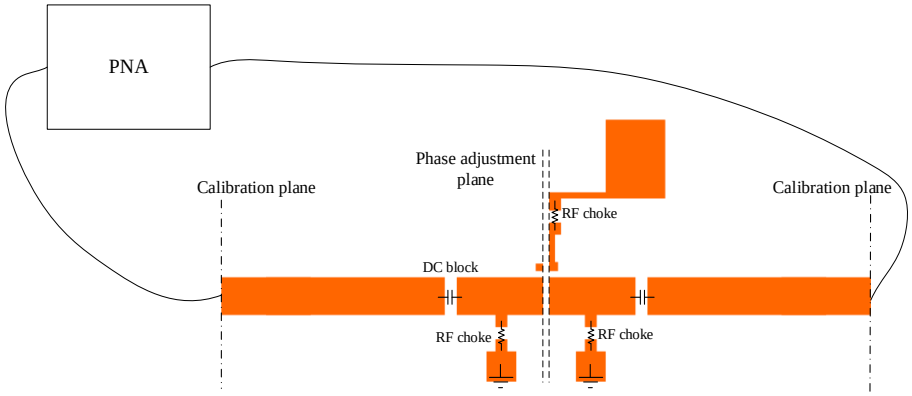

(b)

Fig. 5 (a) Testing configuration for TCP – 5033UB; (b) Reference circuit for port extension.

In order to achieve the de-embedded measurement for the BST varactor, an alternative way is used in our measurement which is much convenient, as Fig. 5 (b). After the PNA SOLT calibration, a further de-embedded is done by the port extension function on PNA test platform. This function can calibrate the phase and loss effect of the connection line and the DC circuit by measuring an identical testing circuit without DUT. It is notable that the port extension function only offers the phase cancellation and the loss compensation for the measurement. Therefore, such a method can only provide accurate results under the 50 Ω configuration. Any impedance variation in the circuit would lead to incorrect results.

The impedance of the BST varactor can be calculated from measured s-parameters using (A. 1). Consequently, the capacitance, resistance, and Q factor of the varactor are given by equations (A. 2) and (A. 3).

$$Z = Z_0 * \frac{(1+S_{11})\cdot(1+S_{22})-S_{12}\cdot S_{12}}{2*S_{21}} \quad \text{(A. 1)}$$

$$R = \mathrm{Re}(Z),\ X = \mathrm{Im}(Z) \quad \text{(A. 2)}$$

$$C = -\frac{1}{\omega \cdot X}\ (\mathrm{pF}),\ Q = \frac{|X|}{R} \quad \text{(A. 3)}$$

Table.A. 2

BST varactor characteristics, f = 1 GHz			
Voltage (V)	Capacitance (pF)	Q factor	Rs (Ω)
0	3.05	14.78	3.52
2	2.85	15.18	3.67
10	1.50	32.17	3.30
18	0.98	44.13	3.68
24	0.80	47.7	4.18

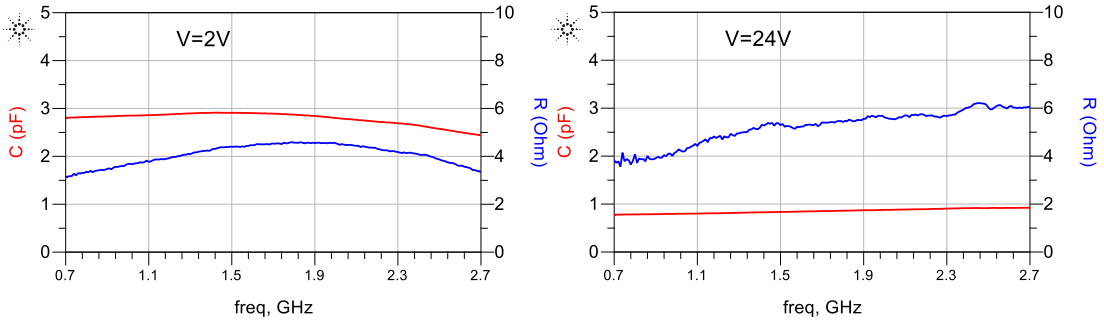

(a) (b)

Fig. 6 Calculated capacitance and resistance of the BST varactor, (a) $V_{bias} = 2V$; (b) $V_{bias} = 24V$.

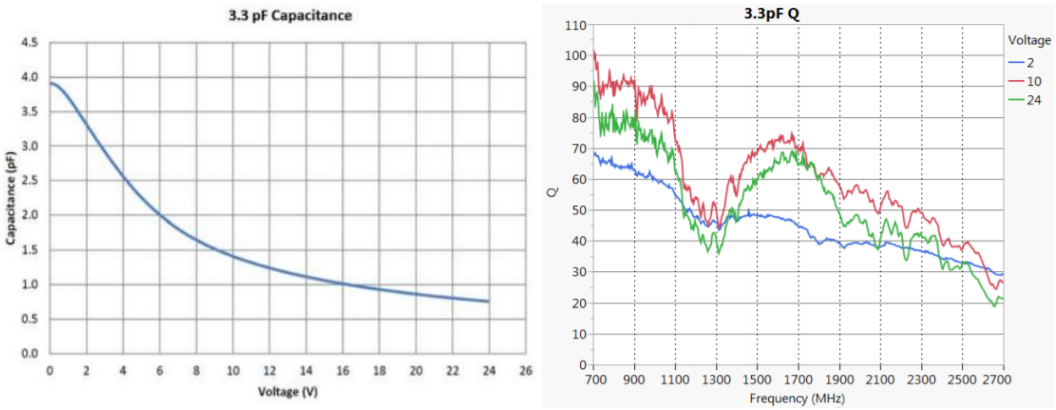

(a) (b)

Fig. 7 Figures from the TCP-5033UP datasheet [2], (a) capacitance vs voltage; (b) Q-factor vs frequency.

Table.A 2 list the calculated parameters at 1 GHz for the BST varactor under different biasing voltages. The extracted capacitance decreases from 3.05 pF to 0.8 pF when the biasing voltage raises from 0 V to 24 V. Meantime, the series-resistance alter between 3.5 Ω and 4.2 Ω. Additionally, the capacitance and the resistance variation along the frequency are plotted in Fig. 6 for biasing voltages of 2 V and 24 V.

For a comparison, Fig. 7 gives the reference plots provided by the datasheet which shows the capacitance range and Q-factor against the frequency. Unlike the measurement, however, the capacitance tuning range provided by the manufacturer is larger than the measured results. This difference could be caused by the phase error of the port extension function in Fig. 5 (b) as the phase deviation would have serious influences on the calculated capacitance. Meanwhile, the measured Q-factor of the BST varactor is much lower than the statement in the datasheet.

IIP3 Measurement for Varactors

Nonlinearity in an RF/microwave component is used to describe the characteristic of a component that introduces the signal distortion or intermodulation. Several standard parameters are commonly applied to evaluate the nonlinearity of a component: 1-dB compression point (P_{1dB}), Third-order intercept point (TOI or IP3), 2nd, and 3rd harmonic, where the third-order intercept point is a critical parameter in the small-signal system. If two interferers at ω_1 and ω_2 are applied to a nonlinear system, the output contains mixing products in which the third-order intermodulation (IM) products at $(2\omega_1 - \omega_2)$ and $(2\omega_2 - \omega_1)$ are of particular interest, as shown in Fig. 8. Equation (A. 4) gives the calculation for the input third-order intercept point (IIP3) based on input power and power difference between the main tones and IM products [4].

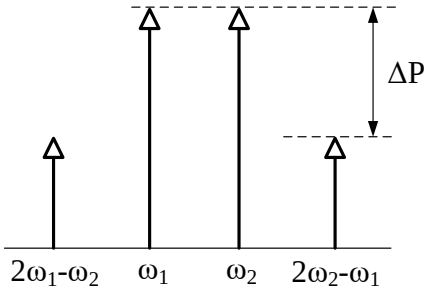

Fig. 8 Illustration of third-order intermodulation.

$$IIP_3\big|_{dBm} = \frac{\Delta P\big|_{dB}}{2} + P_{in}\big|_{dBm} \tag{A. 4}$$

As the varactor implementation can degenerate the linearity of a system, of most concern, the IP3 measurement for the varactor is demonstrated in this section. The measurement includes one varactor diode and one BST varactor for comparison purposes.

TYPICAL SPECIFICATIONS

Representative Performance Data at 25°C

Table 2. PERFORMANCE DATA

Parameter	Min	Typ	Max	Unit
Operating Bias Voltage	1.0		24	V
Capacitance (V_{bias} = 2 V)	3.003	3.3	3.597	pF
Capacitance (V_{bias} = 24 V)	0.646	0.710	0.774	pF
Tuning Range (1 V − 24 V)	4.80	5.25	6.00	
Tuning Range (2 V − 24 V)	4.20	4.65	5.30	
Leakage Current (V_{bias} = 24 V)			0.1	μA
Operating Frequency	700		2700	MHz
Quality Factor @ 700 MHz, 2 V (Note 5)		65		
Quality Factor @ 700 MHz, 24 V (Note 5)		85		
Quality Factor @ 2.4 GHz, 2 V (Note 5)		40		
Quality Factor @ 2.4 GHz, 24 V		35		
IP3 (V_{bias} = 2 V) (Notes 1, 3 and 5)		70		dBm
IP3 (V_{bias} = 24 V) (Notes 1, 3 and 5)		80		dBm
2nd Harmonic (V_{bias} = 2 V) (Notes 2, 3 and 5)		−65		dBm
2nd Harmonic (V_{bias} = 24 V) (Notes 2, 3 and 5)		−75		dBm
3rd Harmonic (V_{bias} = 2 V) (Notes 2, 3 and 5)		−45		dBm
3rd Harmonic (V_{bias} = 24 V) (Notes 2, 3 and 5)		−75		dBm
Average Transition Time (Cmin → Cmax) (Notes 4 and 5)		66		μs
Average Transition Time (Cmax → Cmin) (Notes 4 and 5)		48		μs

1. f_1 = 850 MHz, f_2 = 860 MHz, Pin 25 dBm/Tone
2. 850 MHz, Pin +34 dBm
3. IP3 and Harmonics are measured in the shunt configuration in a 50 Ω environment
4. RF_{IN} and RF_{OUT} are both connected to DC ground
5. Sample testing only. Average Transition Time for all start and stop voltage combinations between 2 V and 24 V is 50 μs.

Fig. 9 BST varactor TCP-5033UB datasheet [2].

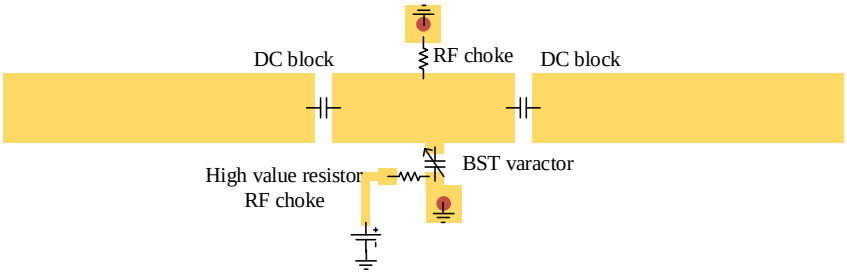

Fig. 10 Measurement circuit for BST varactor.

A. BST Varactor Measurement.

Base on the datasheet in Fig. 9, the BST varactor linearity in the term of third-order intercept point (IP3) is stated as 70-80 dBm at 855 MHz. The measurement is done in the shunt configuration in the 50-ohm environment. Thus, we are using the same measuring configuration here for comparison. Fig. 10 shows the circuit structure according to the reference. A BST varactor TCP-5033UB is shunt to the ground from a 50-ohm transmission line. Two high-value resistors present as RF chokes for the DC bias. Murata GJM 47pF capacitors are allocated at two sides of the circuit as DC blocks.

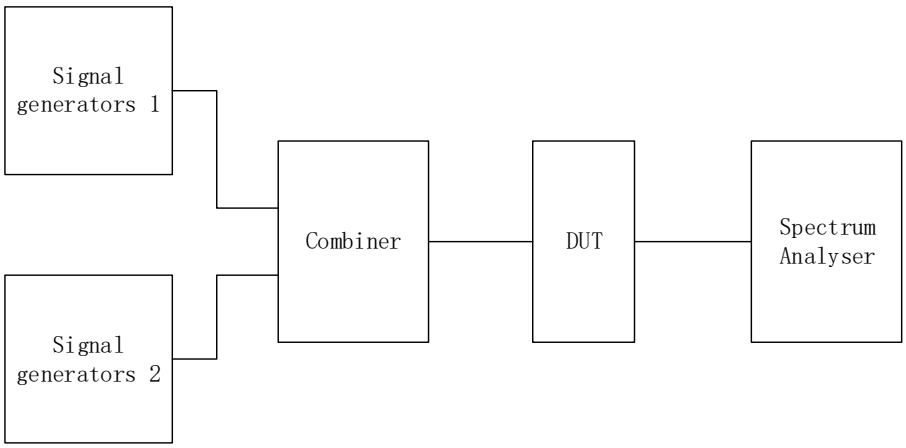

Fig. 11 Linearity measurement set-up configuration.

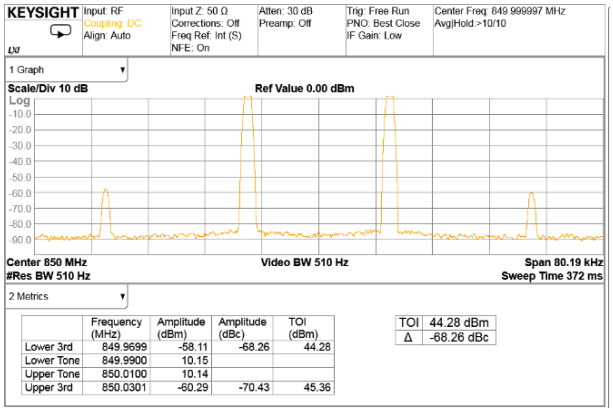

Fig. 12 TOI of the set-up.

Fig. 11 shows the set-up for the varactor IP3 measurement. Two signal generators generate two adjacent-frequency tones which are merged by the following signal combiner. The combined two-tones signal is fed through the DUT and then measured by a signal analyzer. The frequencies of two tones are 849.99 MHz and 850.01 MHz while the power of tones is 10 dBm. Because the mixer in the spectrum analyzer also generates intermodulation products, in order to achieve precise results, it is important that TOI product by spectrum analyser is removed. Therefore, the inherent TOI of the set-up without the DUT is measured at the first as Fig 12. As can be seen, the TOI from the set-up is 44 dBm at lower 3rd and 45 dBm at upper 3rd when input tones power is 10 dBm. Thus, the IIP3 of the set up can be calculated by the (A. 4) of 44.28 dBm at the lower side and 45.36 dBm at the higher side. We should remark that the IM products caused by the set-up vary for different input power. This variation needs to be included in the calculation because of the presence of DUT.

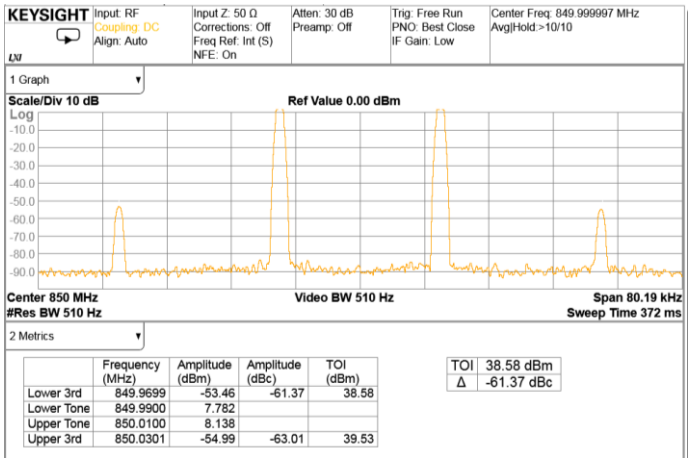

(a)

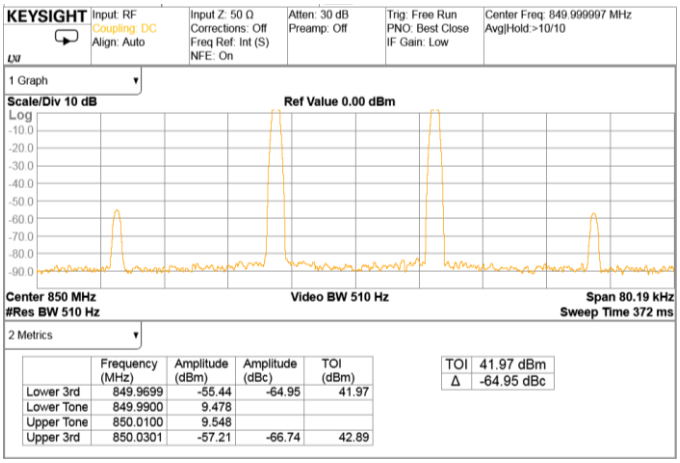

(b)

Fig. 13 Measured intermodulation for the BST varactor circuit, (a) $V_{bias} = 2V$; (b) $V_{bias} = 24V$.

Table.A. 3 Tested IIP3 for BST varactor TCP-5033UB

BST varactor TCP-5033UB IIP3		
Voltage	Lower 3rd	Upper 3rd
2V	41.64 dBm	42.94 dBm
24V	44.16 dBm	46.99 dBm

Fig.13 and Table.A. 3 give the measured IIP3 for the BST varactor. Generally, the BST varactor in a shunt configuration has a stable IIP3 of around 44 dBm. Comparing with the datasheet in Fig. 9, however, the measured IIP3 is much lower than the statement. This difference may be due to the overstatement of the product.

B. Varactor Diode Measurement

Using an identical set-up configuration, the measurement circuit for the varactor diode IIP3 is given in Fig. 14. The varactor SMV2019 with a capacitance tuning range of 0.3–2.22 pF is taken into the measurement. The two-tone signals fed into the DUT are 10 dBm tones at 849.99 MHz and 850.01 MHz. As a result, Fig 15 shows the measured

IM products produced by the varactor diode circuit. As calculated IIP3 listed in Table.A. 4, the IIP3 of the varactor diode varies significantly when different biasing voltages are applied. A varactor diode under higher biasing voltage performs much linear than it under lower biasing voltage.

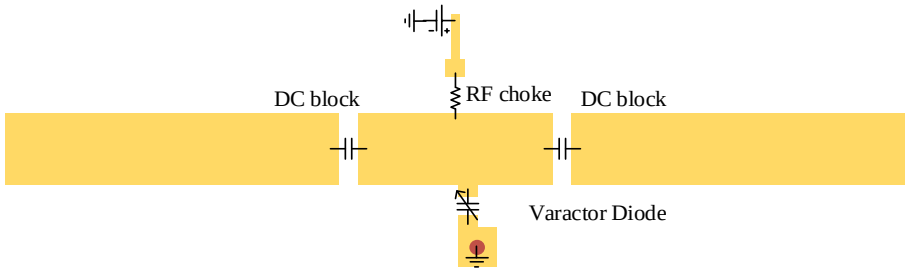

Fig. 14 Measurement circuit for the varactor diode.

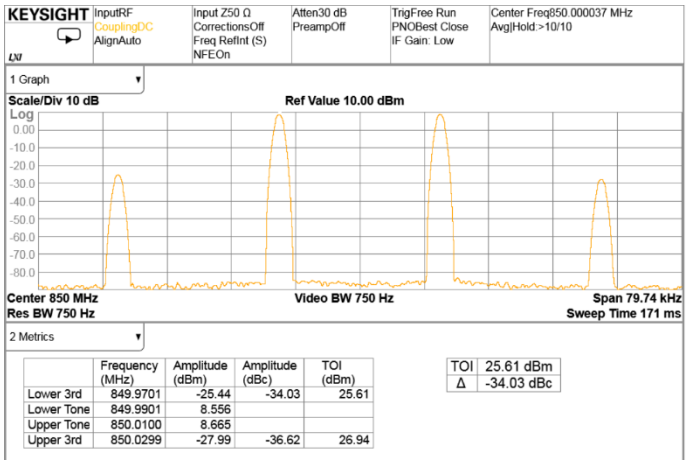

(a)

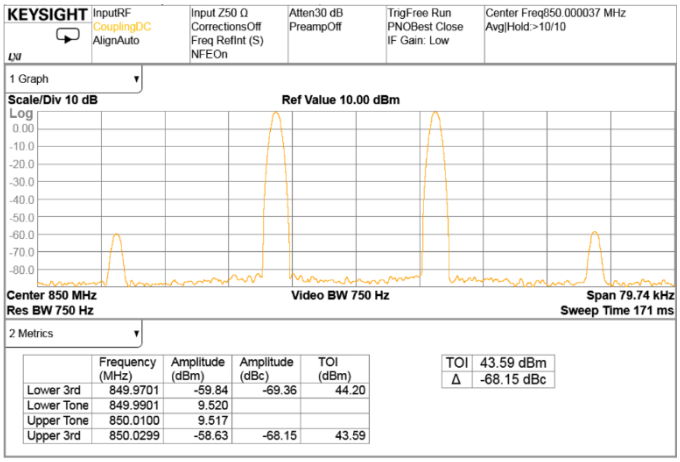

(b)

Fig. 15 Measured intermodulation for the varactor diode circuit, (a) $V_{bias} = 0V$; (b)

$V_{bias} = 20V$.

Table.A. 4 Tested IIP3 for the Varactor Diode SMV2019

SKYWORKS SMV2019 varactor IIP3		
Voltage	Lower 3rd	Upper 3rd
0V (2.22pF)	27 dBm	28.29 dBm
2V (1.2pF)	36.44 dBm	35 dBm
20V(0.3pF)	47.28 dBm	46.83 dBm

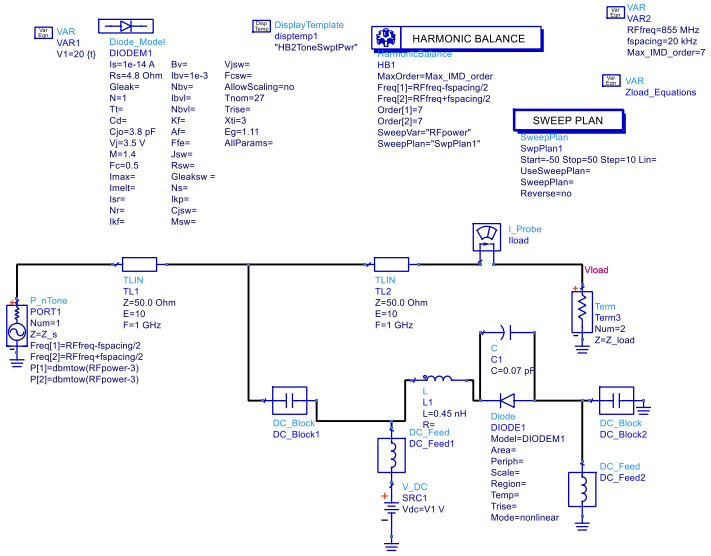

Fig. 16 Two-tones simulation schematic for the varactor SMV2019 in ADS.

Table.A. 5 Simulated IIP3 for the varactor SMV2019

SMV2019 varactor IIP3 - Simulated		
Voltage	Lower 3rd	Upper 3rd
0V (2.22pF)	30.38 dBm	30.38 dBm
2V (1.2pF)	34.92 dBm	34.92 dBm
20V(0.3pF)	55.6 dBm	55.56 dBm

Finally, the SPICE model simulation for the varactor IIP3 is presented in ADS. As mentioned in Chapter 2, SPICE models are usually available for commercial varactor diodes, and the SPICE model describes both RF and DC characteristics of a varactor. Therefore, it is possible to estimate the nonlinearity of a varactor diode in the simulation.

Fig. 16 shows the simulation configuration for the IIP3 evaluation. The varactor diode is shunted in a 50-ohm configuration as the previous measurement. By exciting a two-tone signal at 849.99 MHz and 850.01 MHz, the simulated results are obtained Table.A. 5. As expected, the varactor under a higher biasing voltage returns better linearity performance. Compared with the measured IIP3, the simulated results are close to the measurement but with several dB difference.

High-Frequency Performance Model of SMD Resistors

TYPICAL HIGH FREQUENCY PERFORMANCE ELECTRICAL MODEL

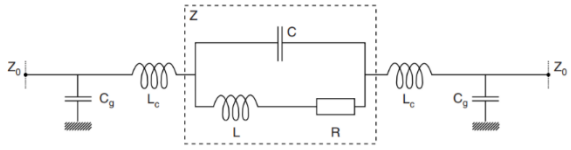

C	Internal shunt capacitance
L	Internal inductance
R	Resistance
Z	Internal impedance (R, L, C)
L_c	External connection inductance
C_g	External capacitance to ground

Fig. 17 High-frequency performance model of a SMD resistor [5].

Fig. 17 shows the RF electrical model for a surface-mount (SMD) resistor [5], where R, L, and C are relevant to the chip resistor itself, L_c and C_g depend on the mounting method in the application. To evaluate the high-frequency performance of an SMD resistor, $|Z|/R$ versus frequency curves can be given by [5]

$$Z = \frac{R + j\omega(L - R^2C - L^2C\omega^2)}{1 + C[(R^2C - 2L)\omega^2 + L^2C\omega^4]} \tag{A. 5}$$

$$\frac{[Z]}{R} = \frac{1}{1 + C[(R^2C - 2L)\omega^2 + L^2C\omega^4]} \times \sqrt{1 + \left[\frac{\omega(L - R^2C - L^2C\omega^2)}{R}\right]^2} \tag{A. 6}$$

For example, $|Z|/R$ curves for the VIHSAY CH-series high-frequency SMD resistor are given in Fig. 18. As can be seen, the $|Z|/R$ curve can considerably deviate from the idea resistor after 3 GHz, especially for the high resistance resistors. In high-frequency applications, the influence of the parasitic should be considered.

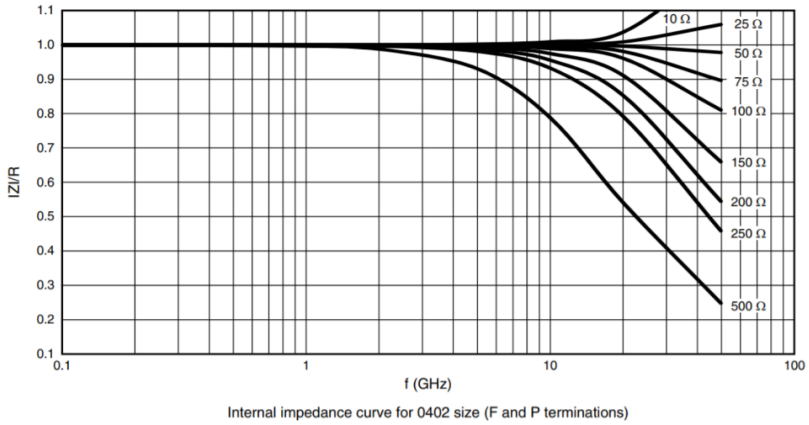

Fig. 18 $|Z|/R$ curves against the frequency for the VISHAY CH series SMD resistors (0402 package size) [5].

Reference

[1] ‘MA46H120 Series’, M/A-COM Lowell. [Online]. Available: www.macom.com.

[2] ‘TCP-5033UB - 3.3 pF Passive Tunable Integrated Circuits (PTIC)’, ON Semiconductor. Available: https://www.onsemi.com/pub/Collateral/TCP-5033UB-D.PDF.

[3] ‘Chip Multilayer Ceramic Capacitors for General - muRata’, muRata. [Online]. Available: www.murata.com.

[4] B. Razavi, *RF Microelectronics, Second Edition*, 2 edition. Upper Saddle River, NJ: Pearson, 2012.

[5] ‘High Frequency 50 GHz Thin Film Chip Resistor - VISHAY’, VISHAY Intertechnology. Available: https://www.vishay.com/.